Development of Cold-sprayed Boron Carbide Metal Matrix Composite Coatings for Wear Resistance Applications

by

Yik Tung Roy Lee

A thesis submitted in partial fulfillment of the requirements for the degree of

Master of Science

Department of Mechanical Engineering

University of Alberta

Abstract

Low-pressure cold spraying was used to fabricate boron carbide-based metal matrix composite coatings for wear resistance applications. Titanium carbide and tungsten carbide-based metal matrix composite coatings were also evaluated to allow for comparison. Powder blends containing 50, 75, and 92 wt.% carbide particles with the remaining mass composed of nickel powder were deposited, then characterized and tested. The velocity and momentum of the different impacting ceramic particles were estimated using a mathematical model. Scanning electron microscopy, image analysis, and X-ray diffraction (XRD) were used to characterize the microstructure of the coatings. The image analysis was used to determine the reinforcing carbide particle loading and the mean free path between reinforcing particles. It was found that the velocity and momentum of the carbide particles was not the dominant factor in their deposition efficiency; in fact, it was the carbide particles with highest momentum and highest fracture toughness that had the highest deposition efficiencies. Vickers micro-hardness, dry abrasion tests, adhesion tests, and preliminary corrosion tests were conducted to evaluate the performance of the coatings. Overall, the micro-hardness and wear resistance increases with increasing reinforcing particle content. Additionally, it was found that the carbide particles with high momentum produced a work hardening effect on the matrix, which led to improvements in the coating properties. In cold spray deposition of metal matrix composite coatings, high fracture toughness in the ceramic powder and high impact momentum of the ceramic particles can improve the micro-hardness and wear resistance of the deposited material.

Preface

A portion of the research presented in this thesis is under review for publishing as: Y.T.R. Lee, H. Ashrafizadeh, G. Fisher, A. McDonald, Evaluation of the effect of the type of reinforcing particles on the deposition efficiency and wear resistance of low-pressure cold-sprayed MMC coatings, Surf. Coat. Technol., under review (Manuscript number: SURFCOAT-D-16-03283). The mathematical modeling of the velocity of the carbide particles was conducted in collaboration with Dr. Hossein Ashrafizadeh. I was responsible for writing the code that was used to calculate the carbide particle velocities. Dr. Hossein Ashrafizadeh completed the data collection for TiC-Ni metal matrix composite coating and contributed to proof reading the manuscript. I was responsible for the data collection with regards to B_4C-Ni and WC-Ni. I completed the data analysis and composed the manuscript. Dr. Gary Fisher contributed his industry experience and contributed manuscript edits. Dr. André McDonald was the supervisory author and also contributed to editing the manuscript. A portion of my thesis is taken from this paper; the sections in question have been indicated with footnotes in the relevant sections.

The research related to the four point bending tests with acoustic emission was conducted as a part of an international collaboration with the University of Nottingham. The collaboration was led by Dr. André McDonald at the University of Alberta. Dr. Gary Fisher contributed his experience as a part of InnoTech Alberta. Dr. Hussain Tanvir was the lead collaborator from the University of Nottingham with Mr. Mohamed Shibly as the Master student working on the project. I deposited the coating samples investigated in this collaboration; they were low-

pressure cold-sprayed Ni, WC-Co-Ni, and B$_4$C-Ni coatings. This thesis included the results produced from this collaboration to serve as a comprehensive evaluation of the B$_4$C-Ni coatings. Mr. Mohamed Shibly collected the data related to four point bending tests with acoustic emission. The collaboration also yielded a detailed X-ray diffraction analysis of the coatings which is included in this thesis. I contributed the data analysis that is detailed in the results and discussion of this thesis.

Acknowledgements

I would like to thank my supervisors, Dr. André McDonald and Dr. Gary Fisher. Their guidance and mentorship were critical to the success of my thesis. They provided me with a solid foundation of mechanical and materials engineering with which I built my thesis and graduate studies upon.

I express my gratitude to all the supporting staff here at the University of Alberta. Thank you to the folks in the machine shop who smiled knowingly whenever I went to do my polishing work. Thank you to the Nanofab for providing characterization analysis and supporting my curiosity with the new and innovative techniques to characterize materials. Also thank you to the staff at InnoTech Alberta who conducted the numerous wear and adhesion tests that were part of my thesis.

To my lab mates and fellow graduate students, I appreciate the countless discussions about various engineering problems and unrelated subjects. The impromptu meetings were a brain exercise allowing for the sharing of knowledge. Thank you also to those who collaborated on research with me and to those who helped proof read my papers. I wish you all the best of luck with the rest of your studies and in the future.

Table of Contents

List of Tables

List of Figures

xii

Glossary of Abbreviations and Symbols

i.   Abbreviations

Al – Aluminum

Al_2O_3 – Aluminum oxide

APS – Air plasma spray

ASTM – American Society for Testing and Materials

B_4C – Boron carbide

BSE – Backscattered electron

Co – Cobalt

CVD – Chemical vapor deposition

EBSD – Electron backscatter diffraction

EDX – Energy-dispersive X-ray spectroscopy

HVOF – High-velocity oxy-fuel

NACE – National Association of Corrosion Engineers

NaCl – Sodium chloride

Ni – Nickel

MMC – Metal matrix composite

ROM – Rule of mixtures

SEM – Scanning electron microscopy

TiC – Titanium carbide

VPS – Vacuum plasma spray

WC – Tungsten carbide

XRD – X-ray diffraction

ii.   Symbols

A – Cross section area (m^2)

C_D – Drag coefficient

C – Sutherland temperature

d – Diameter (m)

F_D – Drag force (N)

F_{impact} – Impact force (N)

H – Hardness

L – Applied load (N)

M – Mach number

m – Particle mass (kg)

N_L – Number of particle intercepts per unit length of line (µm^{-1})

P – Pressure (kPa)

P_s – Shock Pressure (kPa)

R – Gas constant (J/mol.K)

s – Sliding distance (m)

T – Temperature (K)

t – Time (s)

V – Velocity (m/s)

ΔV – Change in velocity (m/s)

v – Volume fraction

Δv – Volume loss (mm^3)

W – Molecular weight (kg/mol)

w – Wear rate (mm^3/N.m)

x – Axial distance (m)

iii.   Greek Symbols

γ – Specific heat ratio

λ – Mean free path (μm)

μ - Gas viscosity (Pa/s)

ρ – Density (kg/m^3)

iv.   Subscripts

0 – Stagnation condition

e – Nozzle exit condition

g – Gas condition

m – Matrix

p – Particle condition

r – Reinforcing particle

ref – Reference condition

v.   Superscripts

* - Nozzle throat condition

1 Introduction[1]

Wear and corrosion are common causes of failure and leakage in the oil and gas industry due to the entrainment of hard-faced particles in a corrosive transport fluid [1]. These solid-liquid mixtures lead to wear and corrosion of process equipment, which negatively affects the longevity of many components in the oil and gas industry including pipelines, valves, drill bits, pump casings, and impellers [2]. As a result of wear- and corrosion-based failures, equipment maintenance can constitute a significant portion of the operating costs at commercial production sites [3].

1.1 Wear

Tribology is the study of friction, wear, and, lubrication. It is the investigation of a solid surface and how it interacts with an environment, whether it be another solid surface, a liquid, or slurry. Wear is a system property and tribologists have defined four components common to most wear scenarios. They are the counter body, the environment, the interfacial element, and the solid body (see Fig. 1) [4]. Typically the wear of the counter body or solid body is studied as they are the components of interest, such as the pipeline, impeller, or pump casing. For example

---

in a pump, the impeller would be the counter body, while the pump casing is the solid body, and the fluid being pumped would be the environment and the interfacial element.
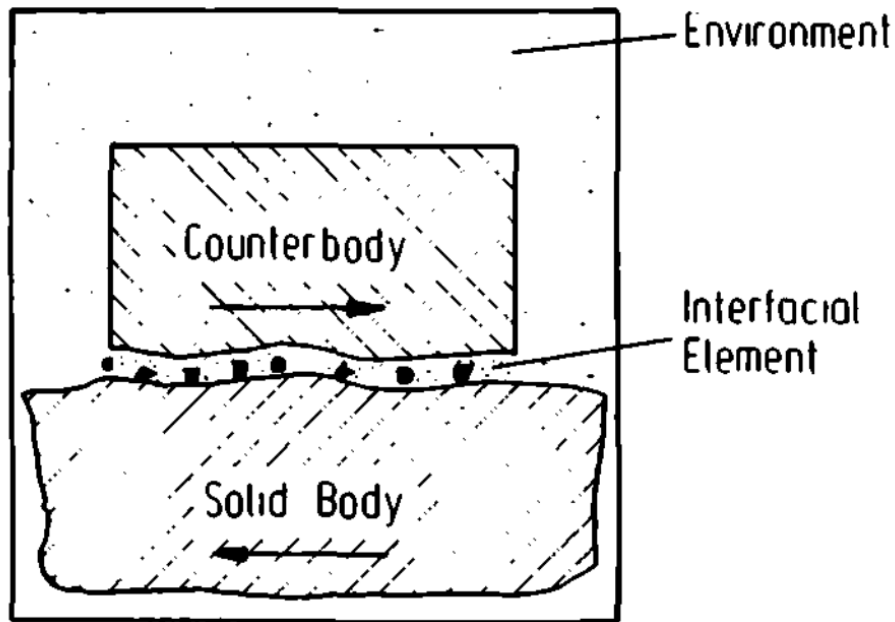
Figure 1: Schematic of the components within a wear scenario [4]

Wear can be divided into different processes based on the motion of the counter body relative to the solid body. There is sliding wear, rolling wear, oscillation wear, impact wear, and erosive wear. The types of relative motion are shown in Fig. 2. The counter body does not have to be a solid, and in the case of erosive wear, the counter body is a fluid. The fluid may contain entrained particles that further increase the amount of wear experienced by the solid body.
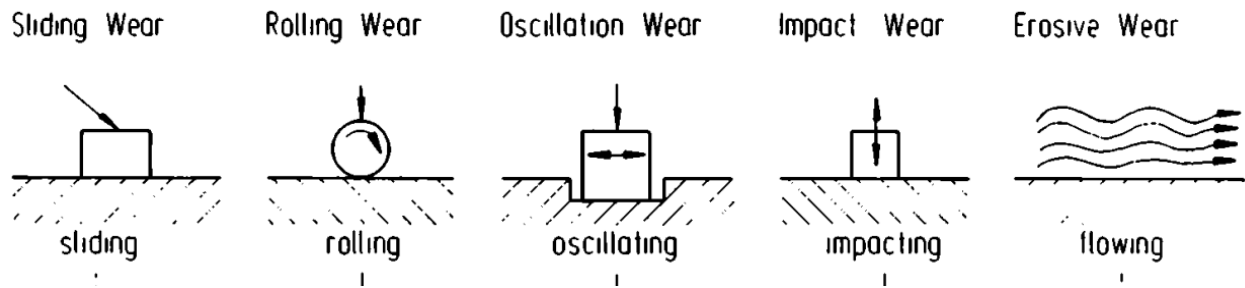
Figure 2: Schematic of the wear processes based on counter body motion [4]

The defining wear process is not the only way to classify a wear scenario since wear mechanisms are also used to classify wear. Wear mechanisms can be divided into the following categories: adhesive, abrasive, delamination, erosion, fatigue, fretting, and corrosion/oxidative wear [5]. Of these wear processes and mechanisms, three major types of wear have been identified in the Alberta oil sands processing industry. They are erosive, impact, and abrasive wear [3]. Erosive wear is the material loss in a solid body due to the flow of a fluid, which may contain entrained solid particles, over the solid surface. Erosive wear occurs during the transport of slurries and the interaction of the suspended solid particles typically with pipes and in other hydrotransport processes [2,3]. Impact wear is due to the repeated impact of large objects such as rocks and boulders, which is a common occurrence in accessories and equipment such as screens or crushers used in the mining stage of oil sands production [3]. Abrasive wear is the result of sand sliding over and between equipment surfaces, which may occur in pumps [3]. The combined effects of wear and corrosion, such as erosion-corrosion, have also been identified as a challenge in the Alberta oil sands industry [6]. The combined effects of wear and corrosion can increase the rate at which materials are removed from a surface. The material loss due to a chemical reaction on the surface can be accelerated by frictional heating, microfracture, and repeated removal of the reaction products [7]. A corrosive environment may also cause a change

3

in the plasticity of a surface and induce stress corrosion cracking [5]. An increase in the cracks within a material surface can increase the wear rates due to certain material removal mechanisms.

1.1.1   *Material Removal Mechanisms*

Abrasive wear is estimated to contribute to approximately 63% of the cost of wear in industry, while erosive, adhesive, fretting, and fatigue make up the other 37% [8]. Therefore, abrasive wear will be the main focus of this study and the material removal mechanisms discussed will be based on an abrasive wear scenario. The material removal mechanisms due to abrasive wear depend on the material properties. For metals and ductile materials, the typical material removal mechanisms are microploughing and microcutting [2,5]. Figure 3 shows a schematic representation of these material removal mechanisms. On a worn surface, microploughing and microcutting can be identified due to characteristic grooves and scratches parallel to the direction of motion during abrasive wear. For ceramics, the material removal mechanism is microcracking [5], which can be identified by brittle fracture surfaces that occur on the wear surface (see Fig. 3). The orientation of the brittle fracture surfaces will depend on the orientation of the cracks from which they are formed, and therefore may not be parallel to the direction of motion during abrasive wear.
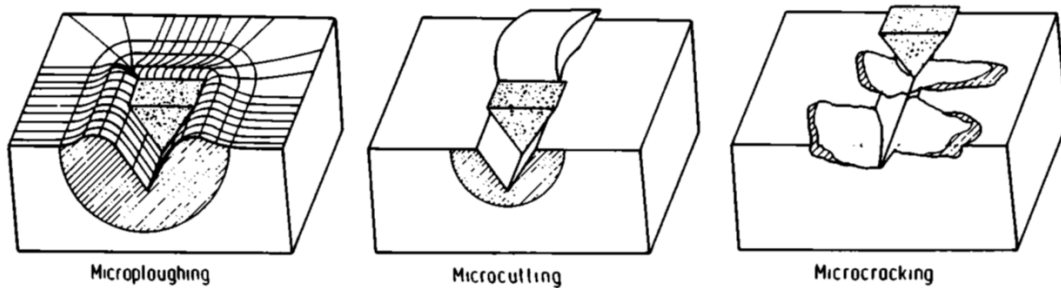
Figure 3: Schematic of the material removal mechanisms in abrasive wear [4]

Wear is a common occurrence in the oil production process and cannot be eliminated; therefore, protective coatings can be deposited on the surface of the components exposed to these harsh environments to increase their lifespan and protect the system from premature failure and leakage. An ideal wear resistant coating would combine high hardness and high fracture toughness. High material hardness reduces the penetration of sand in abrasive and erosive environments and would reduce the material removed due to mircocutting and microploughing [5]. A material with high fracture toughness would reduce the material mircocracking and fracturing removal mechanisms [5].

1.2 Metal Matrix Composite Coatings

Metal matrix composites (MMCs) are engineered materials that that are comprised of at least two constituent phases with properties that are not obtainable with a single phase [9]. One phase is the metallic matrix and the other phase is a reinforcing particle, fiber, or sheet [9]. The reinforcing phase could be a ceramic, other inorganic materials or organic materials. MMCs are

desirable due to their enhanced properties such as lighter weight, higher strength, and improved wear resistance [9]. For wear resistance applications MMC coatings are protective coatings of great interest due to their unique combination of hardness and toughness [10,11]. In MMC coatings, the hard reinforcing phase are usually made from ceramics particles which are distributed within a ductile metal matrix [11]. The combination of the hardness of the reinforcing particles with the toughness of a ductile metal matrix has resulted in high resistance to wear by MMC coatings [4,9,10,12–14].

MMCs have been extensively studied and the rule of mixtures (ROM) has been used to investigate and predict the properties of composite materials [10,11,15,16]. ROM uses two generalized models: the iso-stress and iso-strain models. The iso-strain model defines the theoretical maximum hardness of a composite to be a volume weighted average of the hardness of its constituents, which is

$$H_{\text{upper}} = v_{\text{r}} H_{\text{r}} + v_{\text{m}} H_{\text{m}}. \tag{1a}$$

The iso-stress model defines a minimum hardness for a composite, which is

$$H_{\text{lower}} = \left(\frac{v_{\text{r}}}{H_{\text{r}}} + \frac{v_{\text{m}}}{H_{\text{m}}} \right)^{-1}. \tag{1b}$$

As such, increasing the volume fraction of the hard phase is expected to increase the hardness of the composite.

For wear resistance, the equal wear and equal pressure models have been derived from the iso-stress and iso-strain models [17]. The equal wear model is similar to the iso-strain model in Eq. (1a), thus a maximum wear resistance for the composite can calculated by replacing hardness in with wear resistance in Eq. (1a) [17]. Similarly, the equal pressure model defines a minimum wear resistance and is equivalent to the iso-stress model for hardness in Eq. (1b) [17]. Therefore, based on the ROM, increasing the volume fraction of the wear resistant phase is expected to increase the wear resistance of the composite. However, the wear resistance of the individual components will depend on their individual material removal mechanisms, which could change when they are combined into a composite. Thus, the volume fraction of reinforcing particles required to create a high wear resistance MMC coating will depend on the material removal mechanism within the composite.

The material removal mechanisms in MMC coatings will depend on the intrinsic microstructural properties. These properties include volume fraction of reinforcing reinforcement-and-matrix interface, uniformity in distribution, and average distance between the reinforcing particles [4,9,18]. Higher volume fraction of reinforcing particles and shorter mean free path between these reinforcing particles have been shown to improve load sharing which increases hardness and abrasive wear resistance [10,16,19]. This increase in wear resistance could be attributed to the addition of hard particles which increased in hardness of the composite, decreased the penetration of abrasive sand, and reduced material removal by microploughing and microcutting. Meanwhile the matrix could plastically deform to resist forces that would otherwise fracture or crack the hard reinforcing particles. Overall, wear resistance is increased by combining the hardness of ceramics and the toughness of metals.

1.3   Thermal Spray of Metal Matrix Composites

Thermal spraying processes are one of the methods for deposition of protective wear resistant MMC coatings [3]. In thermal spraying, a heat source is used to heat and accelerate powder particles prior to impacting and spreading on the substrate to form the coating [2,20,21]. MMC coatings have been successfully deposited by thermal spraying processes such as plasma spraying and high-velocity oxy-fuel (HVOF) spraying as reported in previous studies [1,22–25]. However, the high operating temperatures of these processes can induce chemical changes to form undesirable phases in the fabricated coatings [26]. Decarburization or oxidation of tungsten carbide (WC)-based coatings is an example of such a chemical change that occurs during thermal spray deposition [26–28]. The decarburization or oxidation of the feedstock material can reduce the hardness, toughness, and wear resistance of the fabricated coatings [22,23,26,28].

1.3.1   Plasma Spraying

The impact of oxidation on wear rates has been explored by multiple studies. Chen and Hutching [23] compared the low stress abrasion resistance of air plasma spraying (APS) and vacuum plasma spraying (VPS) coatings fabricated from WC-17 wt.% cobalt (Co) powder. It was found that the APS coatings resulted in decarburization and had wear rates of 63 x 10^{-6} mm^3/N.m; whereas, the VPS coatings had little to no decarburization and lower wear rates of 41 x 10^{-6} mm^3/N.m [23]. These wear rates were converted from units of mm^3/km with a 29.4N load to units of mm^3/N.m to match the units used in the present study. Qi $et\ al.$ [29] investigated VPS

and HVOF sprayed TiC-Ni coatings. It was found that the VPS coating had wear rates which were 3 – 4 times lower than the HVOF coatings [29]. Upon investigation of the polished cross sections, it was found that oxides had formed in the inter-splat region of the HVOF coatings and that this contributed to delamination of the coating which resulted in mechanical failure and higher wear rates [29].

1.3.2 High-velocity Oxy-fuel Spraying

For HVOF coatings, decarburization can also led to higher wear rates. Saha and Khan [30] compared the coatings fabricated from microcrystalline WC-Co powder with encapsulated near-nanocrystalline WC-Co powder. The near-nanocrystalline WC-Co particles were encapsulated with Co to minimize the exposure of the WC particles to the HVOF flame; this reduced the decarburization of the WC in the encapsulated near-nanocrystalline WC-Co coating [30]. The micro-crystalline WC-Co powder produced a coating with wear rates of 53.3×10^{-6} $mm^3/N.m$ and the encapsulated near-nanocrystalline WC-Co powder produced a coating with wear rates of 8.65×10^{-6} $mm^3/N.m$ [30]. The improvement in wear rates found by Saha and Khan [30], could be partially attributed to the use of near-nanocrystalline WC powder; however, a study by Guilemany, et al. [31] showed that there was significant decarburization in non-encapsulated nanocrystalline WC-Co HVOF sprayed coatings which resulted in similar wear rates between microcrystalline WC-Co and nanocrystalline WC-Co. Guilemany, et al. [31] used HVOF to spray three powders: conventional microcrystalline WC-Co, nanocrystalline WC-Co, and a blend of conventional microcrystalline WC-Co and nanocrystalline WC-Co. The

nanocrystalline WC-Co coatings were found to experience the most decarburization with wear rates of 8.83 x 10^{-6} mm^3/N.m [31]. A similar wear rate of 8.77 x 10^{-6} mm^3/N.m was found for the microcrystalline WC-Co coatings which experienced the least decarburization [31]. Suggesting that the decarburization of the WC nanoparticles resulted in similar wear rates between the nanocrystalline and microcrystalline WC coatings despite using the nanoparticles to decrease wear rates. Finally, the combined powder produced the most wear resistant coatings with wear rates of 3.90 x 10^{-6} mm^3/N.m [31]. Overall these studies highlight that decarburization negatively effects the wear rates of WC-based composites. Therefore, alternative low temperature deposition processes such as cold spraying are of interest.

1.4 Cold Spraying

Cold spraying is a deposition method where powder particles are accelerated in a supersonic gas flow to high velocities (300 - 1200 m/s) prior to impact on the substrate [2,32]. The temperature of the feedstock material is well below their melting point and the coating is formed by the extensive plastic deformation of the particles upon impact owing to their high velocity [33,34]. Therefore, the powder material is not heated to high temperatures and chemical change in the feedstock material is minimized [16]. The velocity of the particles and the properties of the deposited coatings primarily depend on the pressure of the system. Based on the working pressure, cold spraying has been categorized as either a high-pressure or low-pressure process [35,36]. High pressure cold spraying uses gas pressures in the range of 1 - 4 MPa [36]. In

contrast for low-pressure cold spraying, the pressure of the working gas is usually below 1 MPa and the particle velocities range between 300 and 600 m/s [2,32,35].

1.4.1 *Parameters Affecting Cold Spray Deposition*

The velocity of the particles is related to the deposition efficiency of metallic particles. Schmidt, *et al.* [33] defined a window of deposition for ductile materials based on the velocity of the particles. Upon impact at an optimal velocity, the change in particle momentum transforms into a force that plastically deforms the particle. The high rate of plastic deformation also causes adiabatic shear heating along the interface between the particle and the surface allowing for thermal softening which further facilitates plastic deformation [33]. Overall, the plastic deformation leads to mechanical interlocking of the particles and the formation of a coating [33]. Outside of the window of deposition there is little to no deposition [33]. Below a critical velocity the particles have insufficient change in momentum to cause enough plastic deformation for coating formation [33]. Above an erosion velocity, there is sufficient adiabatic shear heating to melt the particle and cause hydrodynamic penetration that erodes the surface resulting in materials removal [33].

In low-pressure cold spraying the critical velocity, the minimum particle velocity that will allow for adhesion of the cold-sprayed particles to the substrate, of ductile materials may not be attained [2]. However, this spraying technique has been found to be an effective and cost efficient tool for deposition of ceramic-ductile MMC coatings [16,19]. In low-pressure cold

spraying of MMC coatings, the impact of reinforcing particles produces compressive stresses on the previously deposited layers and roughens the deposited surface [2,37]. The compressive stresses increase the density of the fabricated coatings and compensate for the lower impact velocity of the particles. In addition, Sova, *et al.* [37] showed that depending on the size of the ceramic particle, the impact of hard ceramic particles can roughen the surface of the previously deposited layers to promote the adhesion of incoming particles. The fine ceramic particles (average diameter of 19 to 25 μm) roughen the sprayed surface and promote the mechanical interlocking of impacting particles, which increases the deposition efficiency of the mixture in comparison to that of pure metal. In contrast, the coarse ceramic particles (average diameter of 135 to 141 μm) roughen and erode the surface resulting in no significant increase the deposition efficiency due to the enhanced erosion effect [37]. Sova, *et al.* [38] also evaluated the effect of ceramic particle velocity on the deposition efficiency of aluminum oxide (Al_2O_3) and silicon carbide (SiC) reinforcing particles in cold-sprayed MMC coatings [38]. It was found that below a certain velocity the ceramic particles did not penetrate into the coating. This behavior led to lower deposition efficiency [38]. The coarser ceramic particles (average diameter of 127 to 135 μm), which were not accelerated to the required minimum velocity for penetration, eroded the surface and reduced the deposition efficiency. Although Sova, *et al.* [37,38] studied the effect of particle size and velocity on the deposition efficiency of the cold-sprayed MMC coatings, limited attention was given to the effect of the fracture toughness and momentum of the ceramic particles on the deposition efficiency.

1.5 Cold-sprayed Materials and Coatings

High-pressure cold spraying has been successfully used to fabricate MMC coatings. Kim, *et al.* [39] used high pressure cold spraying to deposit micro and nano-structured WC-Co powders containing between 12 - 17 wt. % Co. The deposited coating experienced no decarburization and had high hardness values [39]. The micro-structured WC-Co powder produced cold-sprayed coatings with hardness values of 918 - 984 $HV_{0.5}$, similar to that of HVOF sprayed coatings at hardness values of 1100 - 1200 $HV_{0.5}$ [39]. The cold-sprayed nano-structured powders had even higher hardness values of 1480 - 2053 $HV_{0.5}$ [39]. Kim, *et al.* [39] did not report any wear rates; however, such high hardness values within a MMC coating is promising and shows the potential of cold spraying as an low temperature alternative to HVOF. In a different study, Dosta, *et al.* [40] used high pressure cold spraying to deposit WC-25Co cermet coatings. Again, these coatings exhibited no signs of decarburization and similar hardness values of 884 - 981 $HV_{0.3}$ were found. Dosta, *et al.* [40] also evaluated the wear rates and found values between 27.8 x 10^{-6} and 28.7 x 10^{-6} mm^3/N.m. Given the similar materials were used and similar hardness values were found between the two studies, it is possible that the micro-structured WC-Co coating of Kim, *et al.* [39] would have similar wear rates as that of Dosta, *et al.* [40]. Furthermore the nano-structured WC-Co coating of Kim, *et al.* [39] could possible produce even lower wear rates due to its higher hardness.

Boron carbide (B_4C)-based MMC coatings have also been deposited by high-pressure cold spraying. Feng, *et al.* [41] deposited B_4C-nickel (Ni) MMC coatings using B_4C particles

13

with a size distribution of 20 - 54 μm, $D_{0.5} \approx 35$ μm. Two different techniques were used to combine the B_4C powder with Ni. In one case, the feedstock powder was prepared by way of chemical vapor deposition (CVD) of a Ni layer on the surface of the B_4C particles, while the other feedstock powder was a mechanical blend of B_4C and Ni powders. The mechanically blended feedstock powders contained 78, 84, and 87 vol.% B_4C and produced coatings with 7.6 ± 0.8, 6.9 ± 0.8, and 10.5 ± 0.6 vol.% B_4C, respectively. For the powder that was fabricated by way of CVD of a Ni layer, the feedstock powder contained the same 78, 84, and 87 vol.% B_4C and produced coatings with higher B_4C content of 44.0, 42.1, and 32.7 vol.% B_4C, respectively. The B_4C content in the deposited coatings show that the coating of the B_4C particles in Ni greatly improves the deposition efficiencies of the B_4C particles; however, the relationship between the B_4C content in the feedstock powder and the B_4C content in the coating is not clear. Additionally, the micro-hardness of the cold-sprayed B_4C-Ni coatings are also of interest. Amongst the coatings fabricated from the powder blend, the highest hardness of 336 ± 25 $HV_{0.5}$ was achieved in the coating fabricated from the 78 vol.% B_4C powder blend, with only 7.6 ± 0.8 vol.% B_4C reinforcement in the coating. For the coatings produced from the CVD Ni-coated B_4C powder, the highest hardness achieved was 429 ± 41 $HV_{0.5}$ in the coating fabricated from 87 vol.% B_4C feedstock, with 32.7 ± 1.3 vol.% B_4C reinforcement in the coating [41]. These results do not agree with the conventional ROM for composite materials where hardness is expected to increase with increasing volume fraction of the hard phase [16]. Overall, these results indicate that further studies on the micro-hardness of cold-sprayed MMC coatings and the deposition behavior of cold-sprayed B_4C-based MMC coatings are needed.

Low-pressure cold spraying has also been used to successfully deposit MMC coatings. Melendez, *et al.* [10,16], evaluated the possibility of fabricating WC-12Co-Ni MMC coatings by a low-pressure cold spray system. The cold-sprayed WC-based MMC coatings had a maximum WC content of 68 ± 3 wt.% (52 ± 2 vol.%), a hardness of 553 ± 63 $HV_{0.3}$, and wear rates of 20 x 10^{-6} mm^3/N.m. These wear rates are low and show that low-pressure cold-sprayed WC-based MMC coatings can compete with both the high-pressure cold-sprayed and HVOF sprayed MMC coatings presented earlier. In another study, Hodder, *et al.* [19] also reported the successful fabrication of Al_2O_3-Al MMC coating with low-pressure cold spraying that contained 48 wt.% (38 vol.%) Al_2O_3 reinforcing particles. The hardness of this cold-sprayed coating was 85 ± 24 $HV_{0.2}$. Friction-stir processing was conducted after spraying to improve the homogeneity of the Al_2O_3 distribution within the coating; this increased the hardness of the Al_2O_3-Al composite to 137 ± 3 $HV_{0.3}$. This increase in hardness is evidence that well distributed reinforcing particles with low mean free path can improve the hardness in particle reinforced MMC coatings [19].

1.6 Motivations

The excellent wear resistance of the WC-based MMC coatings has prompted the investigation of other coating reinforcing particles that are harder than WC for use as reinforcement in MMC coatings. Titanium carbide (TiC) and B_4C have hardness values (2900 kg/mm^2 for TiC [42] and 3900 kg/mm^2 for B_4C [42]) that are higher than that of WC (2300 kg/mm^2 [43]), are chemically stable, and possess high resistance to corrosion [29,41]. Additionally, the density of TiC (4.9 g/cm^3 [44]) and B_4C (2.5 g/cm^3 [45]) are much lower than

that of WC (15.8 g/cm^3 [16]) suggesting that these carbides can be accelerated to higher velocities in the gas stream during cold spraying, which will influence particle momentum. Thus, the B$_4$C- and TiC-based MMC coatings deposited by the cold spraying process can potentially be superior to those of WC-based coatings due to the higher hardness of these carbides and also their lower density.

1.7 Objectives

The objective of this study was to explore fabrication and use of low-pressure cold-sprayed B$_4$C-based MMCs for wear applications. In order to conduct a comprehensive exploration of the MMC coatings the following items were addressed:

1. Optimization of the cold spray parameters such that a minimum coating thickness of 300 μm was produced while minimizing the number of nozzle passes.

2. Analysis of the microstructure of the composite using a Scanning Electron Microscope (SEM) and image analysis.

3. Determination of the velocity and momentum of the carbide particles using a mathematical model.

4. Quantification of the deposition efficiency of the carbide particles within the MMC.

5. Evaluation of the performance of the coating by measuring the abrasion wear rates, strain to fracture, and adhesion strength.

6. Relating the hardness, fracture strength and/or fracture toughness of the coatings to the abrasion performance of the coatings using accepted tribological theory.

1.8 Thesis Organization

This thesis is organized into several chapters. The first chapter describes the background information related to the thesis. Chapter 1 also details the motivations and objectives of the thesis. The second chapter describes the experimental method used to deposit and characterize the coatings. The mathematical model developed for predicting the particle velocity is detailed in Chapter 3. Chapter 4 presents and discusses the results obtained from the analysis for the coatings. The fifth chapter summarizes the conclusions of the study. Finally, Chapter 6 will elaborate on the future work that would be valuable in the exploration of the cold-sprayed MMC coatings.

2 Experimental Method[2]

2.1 Powder and Substrate

In this study, fused and crushed carbide particles of B_4C (Panadyne, Montgomeryville, PA, USA), TiC (Pacific Particulate Materials Ltd., Port Moody, BC, Canada), and WC (Pacific Particulate Materials Ltd., Port Moody, BC, Canada) were mechanically blended with Ni powder that was specifically designed for cold spraying (N5001, CenterLine Ltd., Windsor, ON, Canada). Each feedstock powder was created by blending 50, 75, and 92 wt.% of each carbide powder with the remainder Ni powder to produce a total of nine powder compositions. A coating was also obtained with a 96 wt.% B_4C + 4 wt.% Ni; however, it did not meet the minimum thickness requirements for testing and characterization, thus it was removed from the study. Figures 4 –7 show the morphology of the powder particles. As shown, all the selected carbide particles had angular shapes with sharp edges. The Ni powder had a highly dendritic structure (see Fig. 7) to facilitate their deposition and a size distribution of –45 to + 5 μm [46]. The size distribution of the carbide particles was estimated by image analysis (ImagePro, Media Cybernetics, Bethesda, MD, USA) [47]. The average size of the carbide particles was estimated to be 39 ± 10 μm ($n = 42$), 23 ± 7 μm ($n = 28$), and 36 ± 11 μm ($n = 56$) for B_4C, TiC, and WC, respectively. The substrates sizes varied depending on the tests, generally, they were made from low carbon steel and were grit blasted by #24 alumina grit (Manus Abrasive Systems Inc., Edmonton, AB, Canada) prior to deposition.

---

[2] Portions of this chapter were published in: Y.T.R. Lee, H. Ashrafizadeh, G. Fisher, A. McDonald, Evaluation of the effect of the type of reinforcing particles on the deposition efficiency and wear resistance of low-pressure cold-sprayed MMC coatings, Surf. Coat. Technol., under review, (Manuscript number: SURFCOAT-D-16-03283)
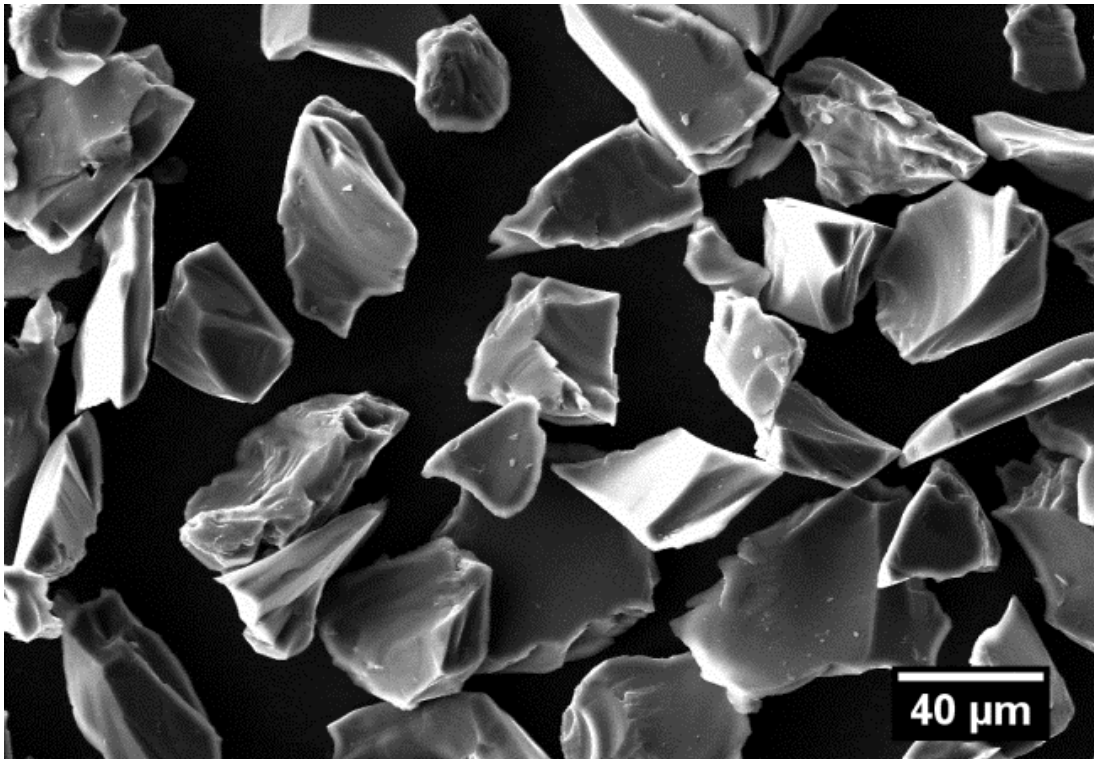
Figure 4: SEM image of B$_4$C powder morphology
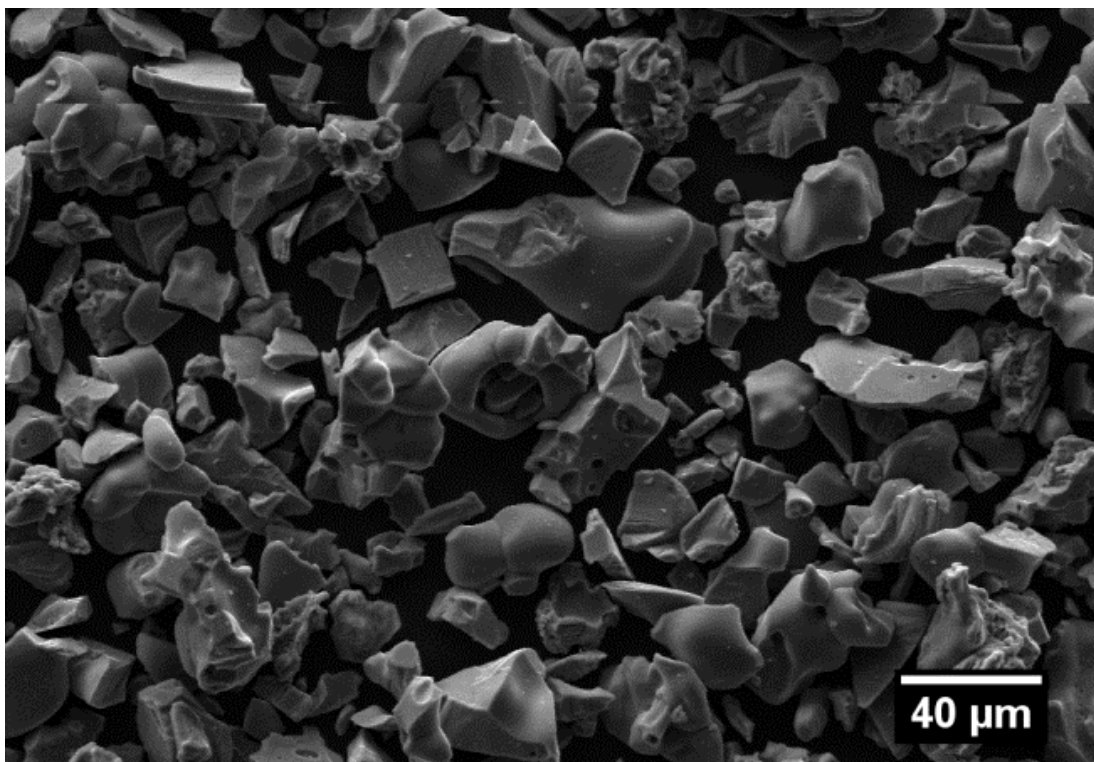
Figure 5: SEM image of TiC powder morphology
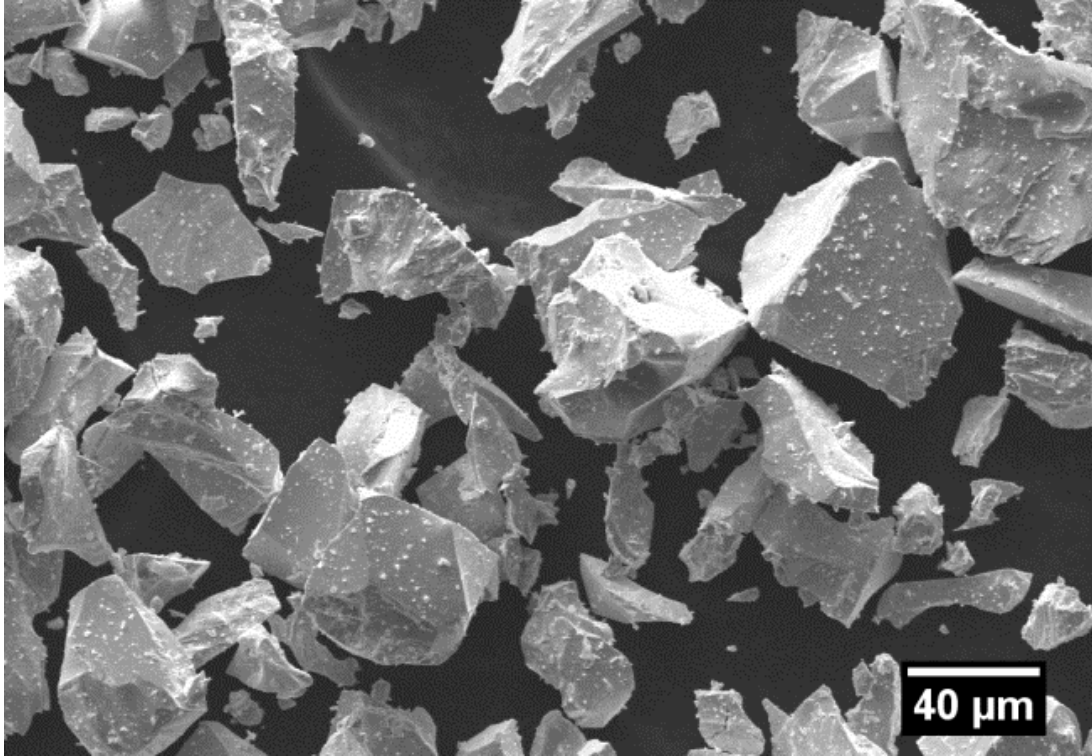
Figure 6: SEM image of WC powder morphology
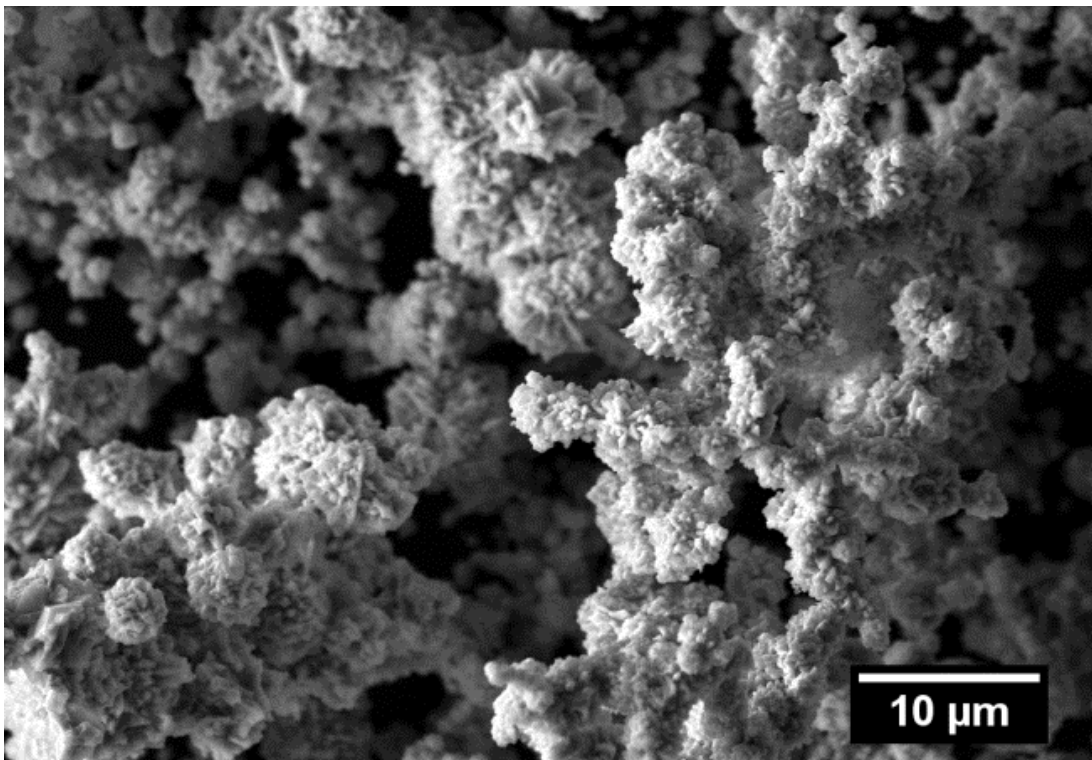
Figure 7: SEM image of Ni powder morphology

2.2 Cold Spray Parameters

A low-pressure cold spray system (SST series P, CenterLine, Ltd., Windsor, ON, Canada), with compressed air as the working fluid, was employed to deposit the coatings. The cold spray system utilized a converging-diverging de Laval nozzle. The selected process parameters are summarized in Table 1. An automatic robot (HP-20, Motoman, Yaskawa Electric Corp., Waukegan, IL, USA) was used to maintain constant stand-off distance (distance between the cold spray nozzle and the substrate) and traverse velocity during the cold spray deposition process. The gun traverse speed was set to 5 mm/s for deposition of all the powder feedstock compositions, except for the 92 wt.% B_4C + 8 wt.% Ni composition, where the gun traverse speed was set to 2.5 mm/s.

Table 1: Cold spray parameters

Process gas	Compressed air
Pressure	634 kPa
Temperature	550°C
Stand-off distance	5 mm

2.3 Coating Characterization

The substrates used for coating characterization were 25 mm x 25 mm x 6 mm and the target thickness for these coatings were 250 μm. The coated samples were cut in cross-sections and cold-mounted in an epoxy resin (Allied High Tech Products, Inc., Rancho Dominguez, CA, USA). The cross sections were then ground using 180, 240, 360, 400, 600, 800, and 1200 grit

21

silicon carbide paper (LECO, Mississauga, ON, Canada) and further polished using 3 μm and 1 μm diamond slurries (LECO, Mississauga, ON, Canada).

A scanning electron microscope (SEM) (EVO MA 15, Zeiss, Cambridge, UK) equipped with energy-dispersive X-ray spectroscopy (EDX) was employed for analyzing and imaging of the cross sections of the fabricated coatings. To avoid surface charging during microscopy, a thin film of carbon was deposited on mounted samples by a carbon evaporation system (EM SCD 005, Leica Baltec Instrument, Balzers, Liechtenstein). EDX was used to confirm the composition of the phases observed within the microstructure.

The SEM images, captured in backscattered electron (BSE) mode, were used for image analysis (ImagePro, Media Cybernetics, Bethesda, MD, USA) to determine the porosity and carbide content within the fabricated MMC coatings. The reinforcing carbide content in the coatings was determined by using the count function within the ImagePro software. This function identifies carbide particles as objects that are brighter or darker than a set intensity. An area percentage of the carbide particles is then calculated and used as an estimate of the volume percentage. For the TiC- and WC-based MMC coatings, a minimum of five micrographs were used to evaluate the volume percentage of carbide particles in each of the deposited powder blends. For the B_4C-based MMC coatings 18 micrographs were used.

The mean free path between the reinforcing particles was calculated by [48]

$$\lambda = \frac{1 - v_r}{N_L}.$$ (2)

To calculate the N_L, five lines were drawn randomly on the SEM images taken for carbide volume fraction analysis and the number of particle intercepts was manually counted and applied in Eq. (2). The mean free path is representative of the spacing between adjacent reinforcing particles in MMC coatings.

2.3.1   *X-ray Diffraction and Rietveld Refinement*[3]

X-ray diffraction (XRD) (Ultimate IV, Rigaku, Sendagaya, Japan) was used to determine the phases in the B_4C powder that was studied. A copper anode was used and the X-rays were generated using a current of 44mA at a voltage of 40 kV. The scan range was between 10 and 80° with a scan rate of 1°/min. The material phases in the B_4C-Ni coatings fabricated from the 92 wt.% B_4C + 8 wt.% Ni powder blend was also determined by using XRD (Siemens D500 diffractometer, Siemens Corporation, Cherry Hill, NJ, USA). A copper anode was used and the X-rays were generated using a current of 25mA at a voltage of 40 kV. The scan range was between 10 and 90° with a scan rate of 0.75°/min. Reitveld refinement was conducted on the coating to allow for a quantitative phase analysis. Reitveld refinement fits a number of calculated XRD phase patterns onto the experimentally-obtained XRD pattern [49]. The number of calculated patterns used depends on the number of phases identified in the sample. In this study,

---

[3] Portions of the experimental work in this section was completed in the collaboration with the University of Nottingham

only the B_4C and Ni phases were used in the Reitveld refinement. A scale parameter for each of the phases present in the sample was calculated to match the calculated XRD phase patterns to the experimental obtained XRD pattern [49]. These scale parameters were combined with the density of the identified phases to calculate the weight percentage of the phases [49].

2.4 Vickers Micro-hardness

A Vickers micro-hardness indenter (MVK-H1, Mitutoyo, Aurora, IL, USA) was used to measure the micro-hardness of the fabricated coatings. The same coatings that were used for microstructure analysis were used for hardness testing. The indentations were conducted according to ASTM Standard E384 (2011) [50] with 300 gram force load and a dwell time of 10 seconds. The indents were spaced a minimum of four indentation diagonals apart, as per the recommendations of ASTM Standard C1327 (2015) [51]. This was done to minimize errors from the work hardening due to the indentations. For the B_4C-based MMC coatings a minimum of 40 indentations were collected on each deposited powder blend. In the case of the TiC- and WC-based MMCs a minimum of five indentations were collected.

2.5 Dry Abrasion Testing

The wear resistance of the cold-sprayed MMC coatings was evaluated by conducting abrasion tests according to ASTM Standard G65 (2010) – procedure E (1000 revolutions) [52].

The substrate size for the abrasion testing was 76 mm x 25 mm x 12.5 mm. Figure 8 shows a schematic of an ASTM G65 test apparatus. During testing, abrasive sand passes between the coated sample and a rotating rubber lined wheel. The AFS 50/70 silica sand (US Silica, Ottawa, IL, USA) was selected as the abrasive medium. The tests on the B$_4$C- and TiC-based coatings were conducted with a neoprene rubber lined wheel, while the tests on the WC-based coatings were conducted with the standard chlorobutyl rubber lined wheel. The testing parameters are presented in Table 2. The abrasive wear rate was calculated by [53]

$$w = \frac{\Delta v}{Ls}. \qquad (3)$$

Each of the B$_4$C-based MMC coating compositions was tested three times. Only one sample was tested for the other MMC coating compositions.
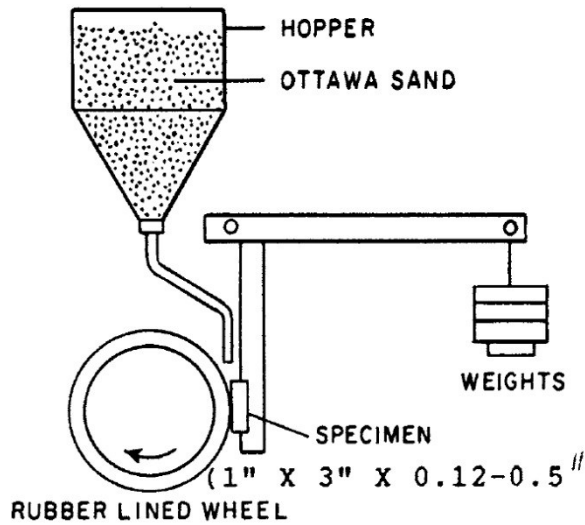
Figure 8: Schematic of ASTM G65 test apparatus [52]

Table 2: Abrasive testing parameters

Number of revolutions	1000
Rotations per minute	200
Total sliding distance	718 m
Applied load	130 N
Sand flow rate	365 g/min

2.6 Four Point Bending with Acoustic Emission[4]

Four point bending tests were conducted to investigate the fracture behavior of the cold-sprayed B_4C-Ni and WC-Co-Ni coatings. The B_4C-Ni coating was produced from the 92 wt.% B_4C + 8 wt.% Ni powder blend. The WC-Co-Ni coatings were fabricated to replicate the highest WC loading coatings fabricated by Melendez, *et al*. [10,16] from the 96 wt.% WC-Co + 4 wt.% Ni; the spray parameters used are the same as those detailed in Table 1 and a traverse speed of 5 mm/s was used. The tests were conducted on a universal testing system (Instron 5969, Norwood, MA, USA). The outer span of the four point bending fixture was 64 mm and the inner span was 32 mm. The tests were conducted at room temperature, and a constant displacement mode was used with a rate of 1 mm/min with a 50 kN load cell. The samples were loaded such that the coating would be in tension for the test. A linear variable differential transformer was used to measure the mid-point deflection, which was set to a maximum of 2 mm. Two acoustic transducers (Physical Acoustics Corporation, Princeton Junction, NJ, USA) were fixed on either end of the sample to collect the acoustic emission from the fracture of the coating. The acoustic data was processed in the AEwin[TM] software (Physical Acoustics Corporation, Princeton Junction, NJ, USA). The two acoustic transducers were calibrated for two different acoustic

---

[4] The experimental tests outlined in this section were completed by Mr. Mohamed Shibly

ranges to maximize the data collected from the fracture behavior; the first range was between 45 and 100 dB and the second range was between 70 and 140 dB. The data showed that there was more significant data in the 45 to 100 dB range, thus only the results from this transducer were included in this study. The B_4C-Ni MMC coating was deposited on titanium alloy, grade 5 (Ti6Al4V), substrates. The substrates were 120 mm x 19 mm x 7 mm. The coating was deposited on one of the 120 mm x 19 mm, then ground down to approximately 200 µm of uniform coating thickness. Based on the substrate a maximum nominal strain of 0.8% was used to prevent plastic deformation in the substrate [54].

2.7 Adhesion Testing

Adhesion testing of B_4C-Ni MMC coating was conducted pursuant to ASTM C633 (2013) [55]. The substrates were threaded diameter low carbon steel cylinders, which were 38 mm tall and 25 mm in. The three powder blends of B_4C-Ni were deposited with a target thickness of 200 µm. Three samples of each of the deposited B_4C-Ni powder blends were tested. The adhesive used was FM-1000 adhesive manufactured by Cytec Industries. The samples were then visually inspected to identify the location of failure in the coatings. Figure 9 shows the potential failure locations as described by ASTM C633 (2013) [55].
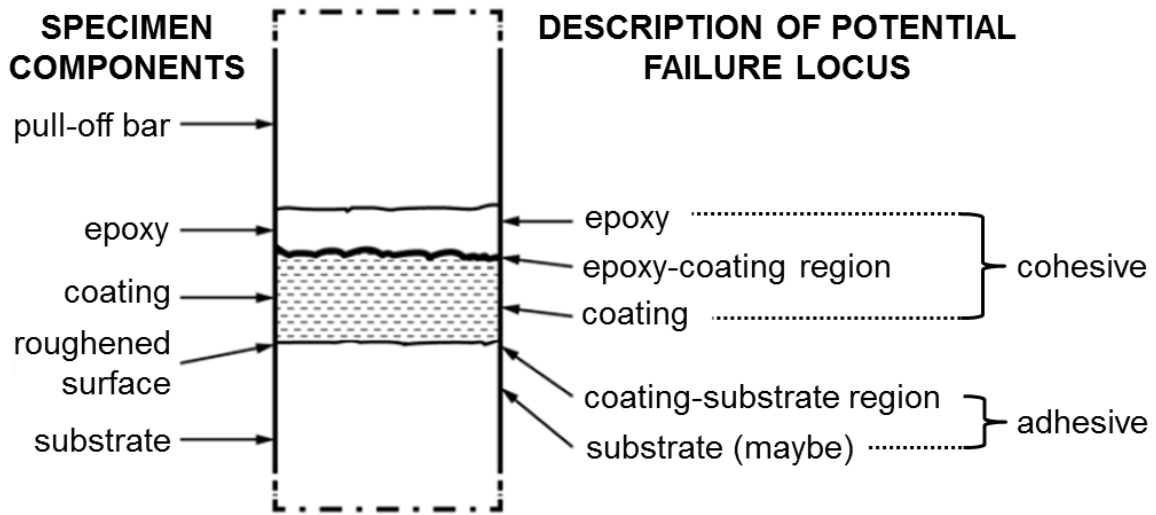
Figure 9: Adapted schematic of ASTM C633 failure locations [55]

2.8 Preliminary Corrosion Testing

NACE/ASTM G31 – 12a [56] was used as a guideline to develop laboratory immersion corrosion tests. The laboratory corrosion tests were conducted for a total of 10 days. The low carbon steel substrates on which the coatings were deposited were approximately 12 mm x 12 mm x 6 mm in size. The cold-sprayed MMC coatings were deposited on one of the 12 mm x 12 mm surfaces. The other surfaces were coated with a rust resistant paint (TREMCLAD, Rust-Oleum, Concord, ON, Canada) to protect the substrate from corrosion. The corrosion samples included: two cold-sprayed coatings fabricated from each of the 92 wt.% carbide + 8 wt.% Ni powder blends, two cold-sprayed Ni samples, two substrates fully coated with the rust resistant paint, and one uncoated substrate.

The composition of the immersion solution was 30 wt.% NaCl (FLS641-500, Fisher Scientific, Ottawa, ON, Canada) and deionized water. A hot plate was used to maintain the temperature of the testing solution at 40 °C. Six 250 mL beakers were used to contain the testing solutions with each beaker filled with 100 mL of the NaCl solution. At regular intervals, the samples were removed, lightly cleaned, and weighed. The solutions were also refilled to 100 mL with deionized water. The reported results were for the total mass loss over the course of the 10 day immersion corrosion tests.

3 Particle Velocity Model[5]

The in-flight velocity of the sprayed carbide particles was estimated by employing a mathematical model based on the principles of dynamics and thermodynamics of compressible fluid flowing through a converging-diverging nozzle [57]. The geometry and dimensions of the nozzle are shown in Fig. 10. In this model, the gas was treated as ideal with constant specific heats. It was also assumed that the gas flow was one dimensional and isentropic [57].
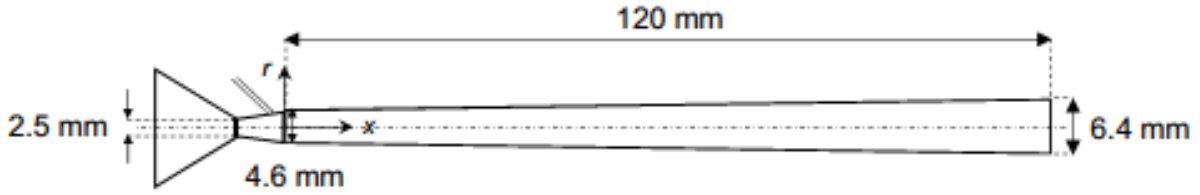
Figure 10: Geometry of the converging-diverging cold spray nozzle

Within the divergent section of the nozzle, the Mach number is a function of only the cross section area of the nozzle and is determined from [57]:

$$\frac{A}{A^*} = \left(\frac{1}{M}\right)\left[\left(\frac{2}{\gamma+1}\right)\left(1+\frac{\gamma-1}{2}M^2\right)\right]^{\frac{\gamma+1}{2(\gamma-1)}}. \tag{4}$$

Due to the mathematical difficulty associated with solving the non-linear equation of Eq. (4), the following equations derived by Grujicic, *et al.* [58] were used to determine the Mach number:

$$M = \left[k_1\frac{A}{A^*}+(1-k_1)\right]^{k_2}, \tag{5a}$$

---

where $k_1 = 218.0629 - 243.5764\gamma + 71.7925\gamma^2$ and $\qquad$ (5b)

$k_2 = -0.12245 + 0.28130\gamma$. $\qquad$ (5c)

Pressure, temperature, velocity, and density of the gas at any point within the divergent section of the nozzle were determined by using Eqs. (6) to (9), respectively and given as [57,58]:

$$P_g = P^* \left(\frac{\gamma + 1}{2 + (\gamma - 1)M^2} \right)^{\frac{\gamma}{\gamma - 1}} , \qquad (6a)$$

$$\text{where } P^* = \frac{P_0}{\left(1 + \frac{\gamma - 1}{2} \right)^{\frac{\gamma}{\gamma - 1}}} ; \qquad (6b)$$

$$T_g = \frac{T_0}{\left(1 + \left(\frac{\gamma - 1}{2} \right) M^2 \right)} ; \qquad (7)$$

$$V_g = M \sqrt{\gamma R T_g} \text{ ; and} \qquad (8)$$

$$\rho_g = \frac{\rho_0}{\left(\left(1 + \frac{\gamma - 1}{2} M^2 \right)^{\frac{1}{\gamma - 1}} \right)} . \qquad (9)$$

In derivation of these equations, it was assumed that the carrier gas was supplied from a large chamber where its velocity was zero. The stagnation temperature and pressure used were 823 K (550 °C) and 634 kPa gauge pressure (735 kPa absolute pressure).

The validity of Eqs. (6) to (9) is based on the assumption that no normal shocks occurred in the nozzle. This condition requires that the shock pressure be higher than that of the ambient pressure [59]. In other words, P_s, as determined by Eq. (10) should be larger than the ambient

pressure (101 kPa) [57,58]. The validity of this condition was verified in this study. Equation (10) for the shock pressure is

$$P_s = P_e \left(\frac{2\gamma}{\gamma+1} M_e^2 - \frac{\gamma-1}{\gamma+1} \right). \tag{10}$$

The particle velocity was determined in accordance with the second law of motion by assuming that the drag force was the only force applied on the accelerating particles:

$$m_p a_p = m_p \frac{dV_p}{dt} = m_p \frac{d^2 x_p}{dt^2} = F_D, \tag{11a}$$

where the drag force was determined by,

$$F_D = \frac{1}{2} C_D A_p \rho_g \left(V_g - V_p \right)^2, \tag{11b}$$

where the drag coefficient, C_D, was determined to be [60]:

$$C_D = \frac{24}{Re_p} \left[\frac{\left(1 + 0.15 Re_p^{0.687}\right)\left(1 + \exp\left(-\left(\frac{0.427}{M_p^{4.63}}\right) - \left(\frac{3}{Re_p^{0.88}}\right)\right)\right)}{1 + \left(\frac{M_p}{Re_p}\right)\left(3.82 + 1.28 \exp\left(-1.25 \frac{M_p}{Re_p}\right)\right)} \right], \tag{12}$$

for

$$Re_p = \left| V_g - V_p \right| \frac{\rho_g d_p}{\mu}, \tag{13a}$$

where $\mu = \mu_{ref} \frac{T_{ref} + C}{T + C} \left(\frac{T}{T_{ref}} \right)^{\frac{3}{2}}$; and $\tag{13b}$

$$M_p = \frac{\left|V_g - V_p\right|}{\sqrt{\gamma R T_g}} \quad .$$ (14)

The reference conditions were taken from Prisco [60], where the reference gas was air and the viscosity was 18.27 Pa/s, the reference temperature was 291.15 K, and the Sutherland temperature was 120 K.

The chain rule was applied to derive the time independent form of Eq. (11) and Euler's method was employed for numerical integration and derivation of particle velocity and acceleration at each point. Thus, the final equation for particle velocity was determined as [59,61]

$$V_{p,x} = \left(V_{p,x-1}^2 + \frac{1.5 \Delta x C_D \rho_g}{d_p \rho_p} \left(V_{g,x} - V_{p,x-1} \right)^2 \right)^{0.5} \quad .$$ (15)

Equation (15) was solved numerically at spatial intervals of $\Delta x = 0.1$ mm across the length of the nozzle for determination of the velocity of the reinforcing particles at the nozzle exit.

The complete and commented MATLAB code for the applied mathematical model can be found in Appendix A.

4   Results and Discussions[6]

The focus of this study is the development of low-pressure cold-sprayed B_4C-based MMC coatings. TiC- and WC-based MMC coatings were also explored in this study to provide a comparison between different carbide reinforcements in low-pressure cold spraying. Each carbide powder was mechanically blended with Ni to produce the cold-sprayed MMC coatings. The follow chapter discusses the results obtained from the testing conducted on the cold-sprayed MMC coatings that were studied.

4.1   Cold Spray Parameter Selection

The cold spray parameters were selected such that a B_4C-Ni coating could be easily deposited. Figure 11 shows a sample of the successfully deposited 92 wt.% of B_4C + 8 wt.% Ni powder blend. The coatings fabricated from 50 wt.% and 75 wt.% of B_4C content in the fed powder were similar to Fig. 11 though with less reinforcing particles, images of the coatings fabricated from 50 wt.% and 75 wt.% of B_4C can be found in Appendix B. Initially, all the cold spray parameters were selected as the same as that of Melendez, *et al.* [10,16] in the successful deposition of low-pressure cold-sprayed WC-Co-Ni coatings. These parameters are within guidelines suggested by SST Centerline Ltd. for the deposition of the Ni powder [46]. The temperature of 550°C maximizes the velocity of the expanding gas while maintaining a low

---

[6] Portions of this chapter were published in: Y.T.R. Lee, H. Ashrafizadeh, G. Fisher, A. McDonald, Evaluation of the effect of the type of reinforcing particles on the deposition efficiency and wear resistance of low-pressure cold-sprayed MMC coatings, Surf. Coat. Technol., under review, (Manuscript number: SURFCOAT-D-16-03283).

enough temperature to minimize recrystallization of the Ni powder. These parameters were found to be successful for the 50 and 75 wt.% B_4C coatings; however, in the powder blends containing 92 and 96 wt.% B_4C the brittle carbide to ductile metal ratio became too high and rate of coating deposition on the substrate dropped considerably. The high ratio between brittle carbide and ductile binder resulted in insufficient metal to deposit between impacting carbides. As such the high carbide content powder blends (92 and 96 wt.%) eroded at the previously deposited layers and the overall deposition efficiency was very low. The traverse speed was decreased to 2.5 mm/s to increase the coating deposition rate and to maintain similar parameters to Melendez, *et al.* [10,16]. Decreasing traverse speed was expected in increase deposition efficiency by increasing substrate heating and facilitating substrate side deformation [62]. Substrate side deformation is important to carbide deposition efficiencies as they do not plastically deform to cause the mechanical interlocking required to deposit a coating. The slower traverse speed improved the deposition of the 92 wt.% B_4C powder blend and a coating with a thickness above 300 μm could be deposited for subsequent testing and evaluation, see Fig. 11. Even with the slower traverse speed the sample where the 96 wt.% B_4C powder blend was deposited showed no change in thickness after three passes. The deposited coating was thin, with only approximately 60 μm in thickness, see Fig. 12. This was insufficient thickness for performance testing and the coating deposited from the powder blend containing 96 wt.% B_4C was therefore eliminated from the study.
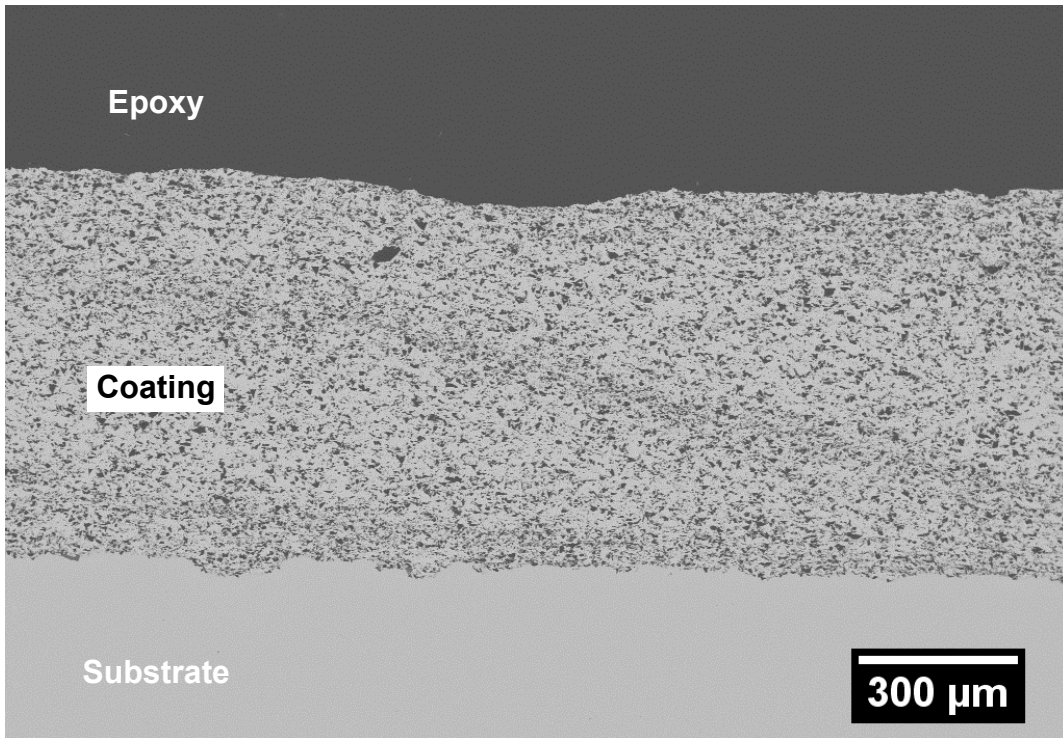
Figure 11: BSE image of the MMC coatings microstructure fabricated from 92 wt.% B_4C + 8 wt.% Ni in the powder blend
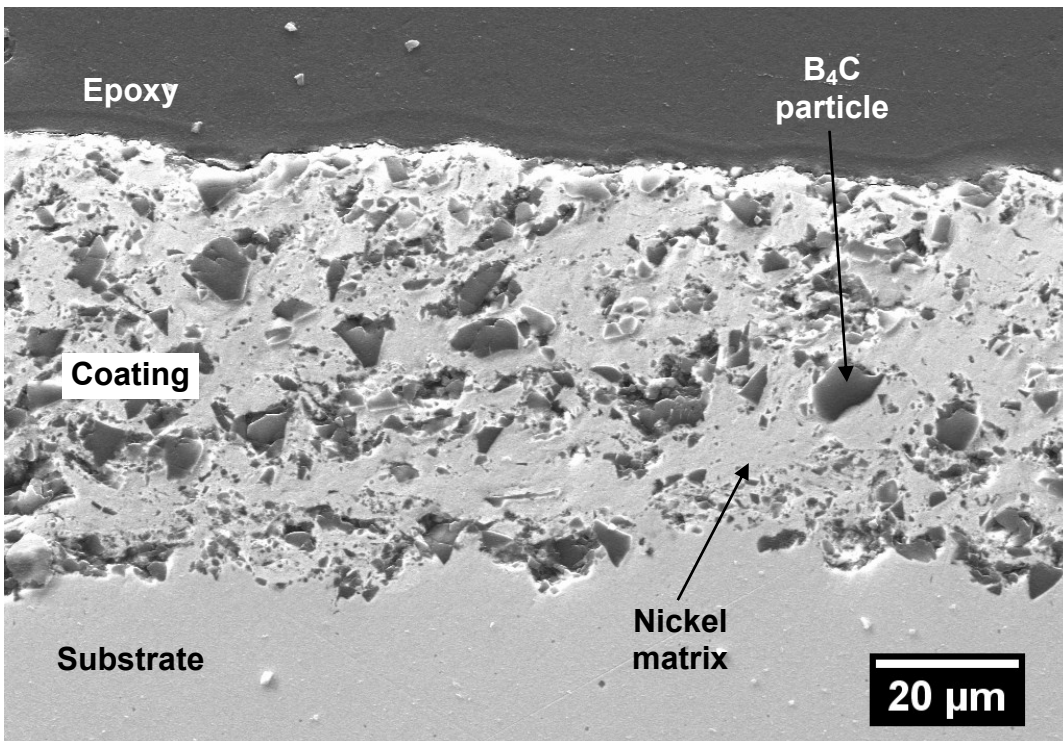
Figure 12: Secondary electron image of the MMC coatings microstructure fabricated from 96 wt.% B_4C + 4 wt.% Ni in the powder blend

4.2   Particle Velocity

In cold spraying, the temperature of fed powder particles in the working gas stream are well below their melting point and the fabrication takes place by the extensive plastic deformation and interlocking of the impacting particles. Therefore, no deposition occurs when depositing brittle materials without ductile binder. Instead, the accelerated carbide particles may fracture, rebound, and even erode the substrate surface upon impact [33]. On the other hand, the addition of ductile metallic powder to brittle ceramics would allow for cold spray deposition of the metal-ceramic mixtures. In cold spray deposition of metal-ceramic powder blends, the ceramic particles can compress and compact the deposited metal particles to further consolidate the coating [2,16]. Additionally, the impact and penetration of ceramic particles can roughen the substrate to improve the overall deposition efficiency of the coating [37,38].

The impact velocity of the ductile metals plays an important role on the overall deposition efficiency and characteristics of the fabricated coatings. It has been shown in previous studies, that the impact of metal particles with higher velocity would allow for increased deformation and interlocking of the splats and, therefore, higher deposition efficiency with reduced pores within the coating [33,63,64]. Conversely, fewer studies have focused on studying the effect of the velocity of the carbide particles on the deposition efficiency and properties of cold-sprayed metal-ceramic powder blends [37,38].

In order to study the effect of carbide particle velocity on the properties and deposition efficiency of the cold-sprayed MMC coatings, the mathematical model developed in this study was employed to estimate the velocity of the carbide particles. Figure 13 shows the velocity of the working gas, B₄C, TiC, and WC particles through the expanding section of the nozzle as calculated by Eq. (15). The origin on the x-axis of Fig. 10 was where the powders entered the nozzle. As seen from Fig. 13, the WC particles have the lowest velocity at all points along the nozzle due to the higher mass of this carbide. The velocity and mass of the carbide particles define the forces and stresses produced upon impact. The impact force is a function of the change in momentum of the impacting carbides, and is given according to impulse formula,

$$m\Delta V = \int F_{impact} dt \, , \tag{16}$$
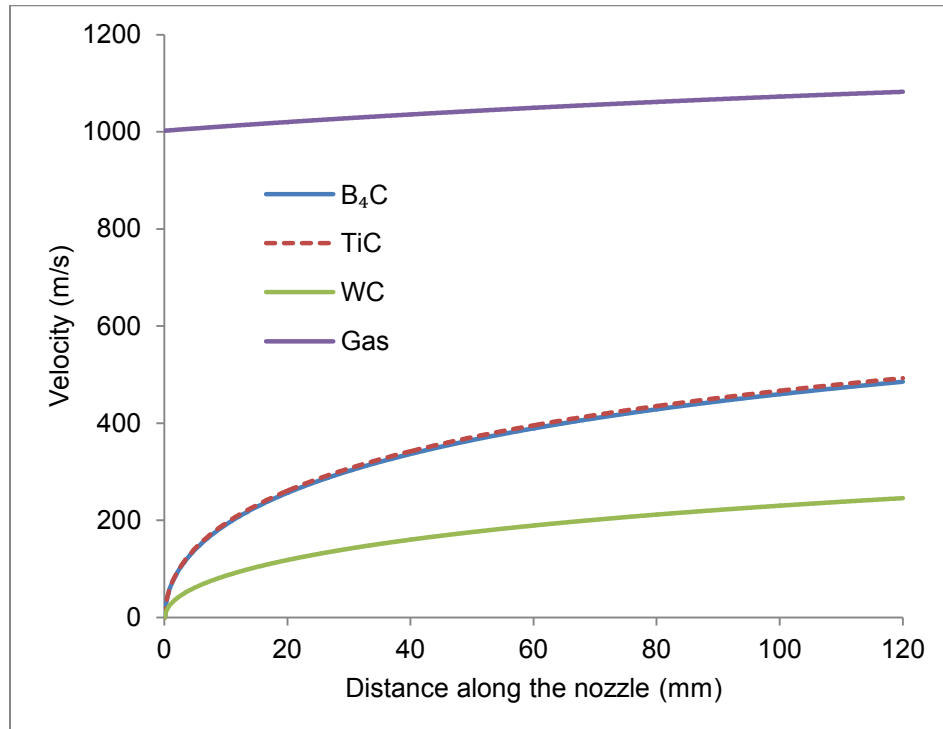
Figure 13: Air and carbide particle velocities along the diverging section of the cold spray nozzle

In this study, the momenta of the carbide particles were estimated by assuming a perfectly plastic collision, where the coefficient of restitution was zero. This assumption allowed for the comparison of the forces produced upon impact for the different carbides that were studied. The velocities and momenta that were calculated are shown in Table 3. The TiC particles had smaller size, lower mass and, therefore, had the lowest momentum. In contrast, the denser WC particles had the maximum momentum. The higher momentum led to higher forces upon impact that increased the compression of ductile metal and also increased the possibility of penetration of carbide particles into the coating.

Table 3: Particle parameters – density, diameter, velocity, and momentum

	Density (g/cm^3)	Mean Diameter (μm)	Mean Velocity (m/s)	Mean Momentum (nNs)
B$_4$C	2.52	39 ± 10 ($n = 42$)	485	38
TiC	4.93	23 ± 7 ($n = 28$)	493	15
WC	15.8	36 ± 11 ($n = 56$)	246	95
	Density (g/cm^3)	Diameter (μm)	Velocity (m/s)	Momentum (nNs)
Ni (5 μm)	8.9	5	754	0.4
Ni (45 μm)	8.9	45	276	117

4.3 Microstructure

The scanning electron microscope (SEM) micrographs taken of the coating cross sections were used to study the microstructural features of the fabricated coatings. Figures 14 – 16 show typical backscattered electron (BSE) micrographs of the fabricated coatings with 92 wt.% of carbide content in the sprayed powder blend. In these micrographs, B$_4$C and TiC appear darker than the Ni matrix due to their lower atomic weight compared to Ni (see Figs. 14 and 15). In contrast, the WC reinforcing particles were brighter than the Ni matrix in the BSE image (see

Fig. 16) due to the higher atomic weight of WC than Ni. The morphology of the coatings fabricated from 50 wt.% and 75 wt.% of carbide content in the fed powder were similar to the images shown in Figs. 14 – 16, though, with less reinforcing particles. Additional SEM micrographs showing the microstructure of the coatings fabricated from 50 wt.% and 75 wt.% of carbide content in the feedstock powder can be found in Appendix B.
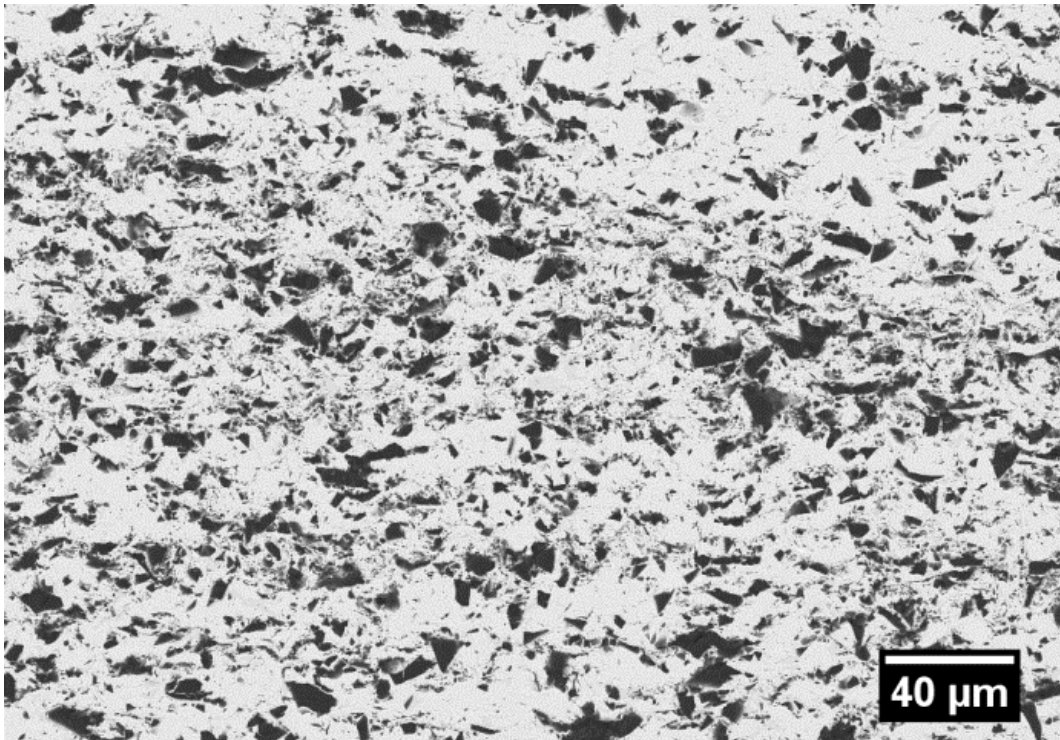
Figure 14: BSE image of the MMC coatings microstructure fabricated from
92 wt.% B_4C + 8 wt.% Ni in the powder blend
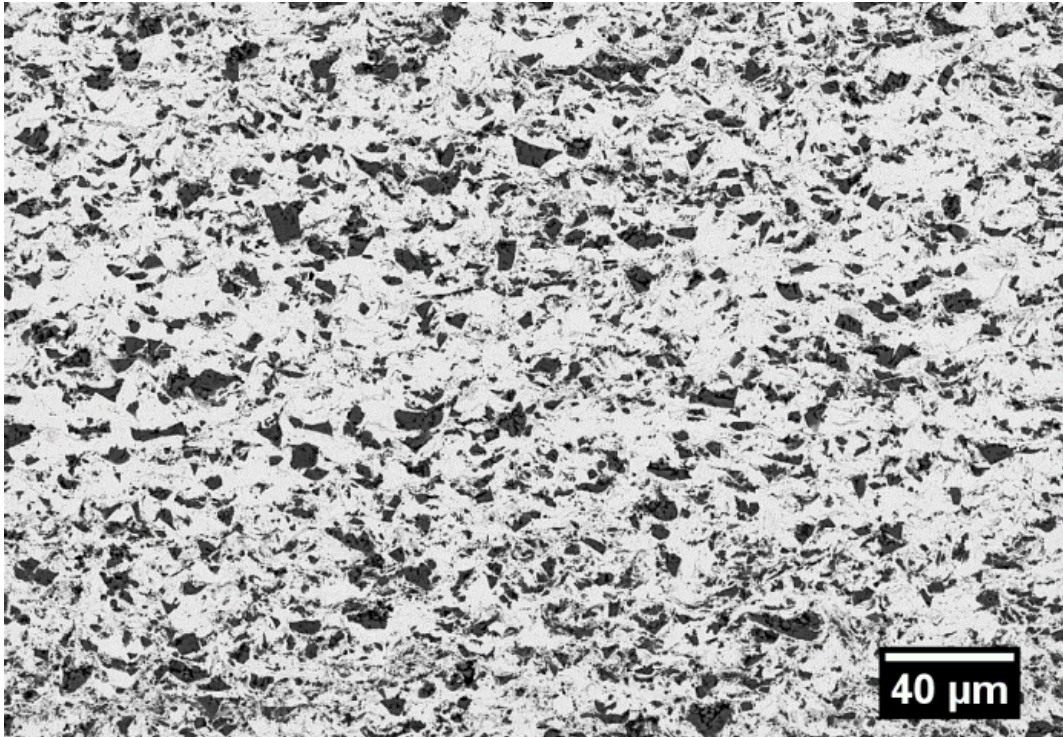
Figure 15: BSE image of the MMC coatings microstructure fabricated from
92 wt.% TiC + 8 wt.% Ni in the powder blend
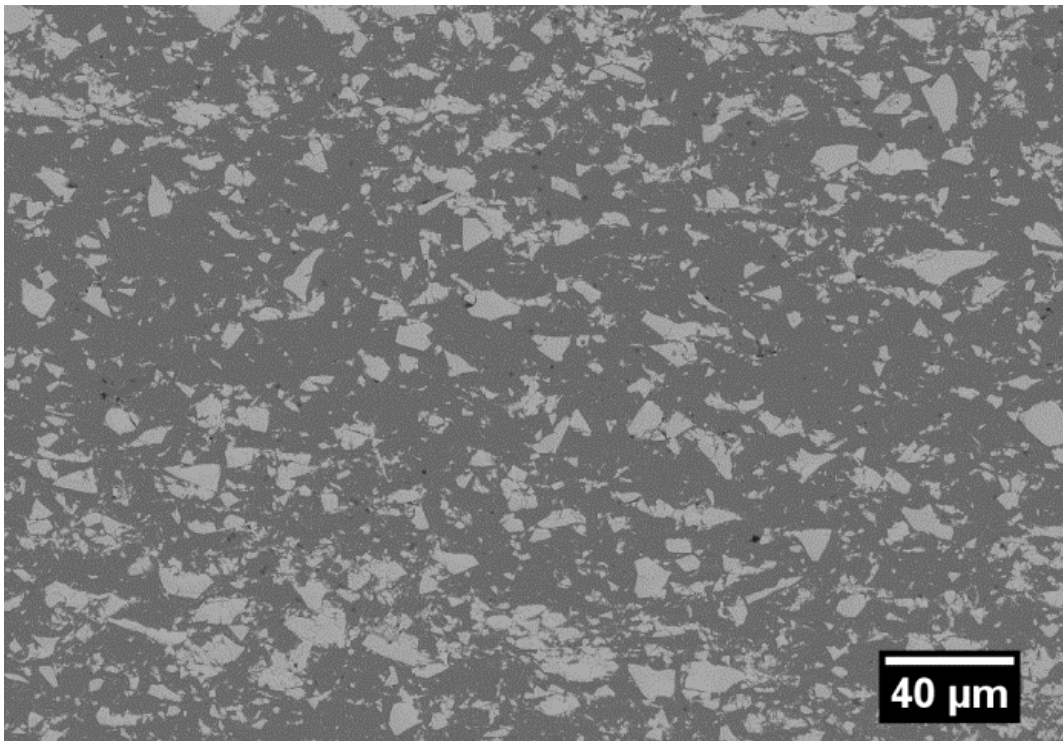
Figure 16: BSE image of the MMC coatings microstructure fabricated from
92 wt.% WC + 8 wt.% Ni in the powder blend

4.3.1 Carbide Particle Fracture

The comparison of the micrographs in Figs. 4 – 6 with Figs. 14 – 16 suggests that there was a reduction in the size of the carbide particles after deposition. For all three types of reinforcing particles that were studied, the carbide particles within the coating (see Figs. 14 – 16) were smaller than the carbide powder particles prior to spraying (see Figs. 4 – 6). In order to quantitatively evaluate the changes in the size of the reinforcing particles, image analysis was conducted to measure the average diameter of the carbide particles before and after the spraying. Figure 17 shows a typical graph of the WC carbide particle size distribution after deposition. As seen in this figure, the distribution of the carbide particles was shifted towards 1 μm. This behavior was observed for all the carbide particles that were studied, regardless of the carbide type, initial diameter, and weight percent of the reinforcing particle within the feedstock powder. Due to the non-normal distribution of the graph presented in Fig. 17, a weighted averages technique was used to calculate a single value for the size of the reinforcing particles within the coating [65]. Table 4 shows the weighted average values for the diameters of the carbide particles within the fabricated coatings. A comparison of the average size of the carbide particles before and after cold spraying show the reduction in size of the carbide particles and provides evidence for fracture of the carbide particles during spraying. It should be noted that the distribution shift of the particle size to 1 μm (see Fig. 17) could have been due to the resolution limit of the measurement technique. This resolution limit was due to the magnification of the images used and the image analysis software. The magnification of the images used for particle size analysis limited small particles in the coating to only a few pixels. Furthermore, the image analysis software identifies each pixel as a certain number of microns and can only measure

particles that are larger than a certain number of pixels. Therefore, particles below 1 μm may not have been counted or were counted as a larger 1 μm particle. Due to the resolution limit, it was difficult to conclude a trend from the data presented in Table 4; however, the fracturing of carbide particles upon impact with the surface was clear.
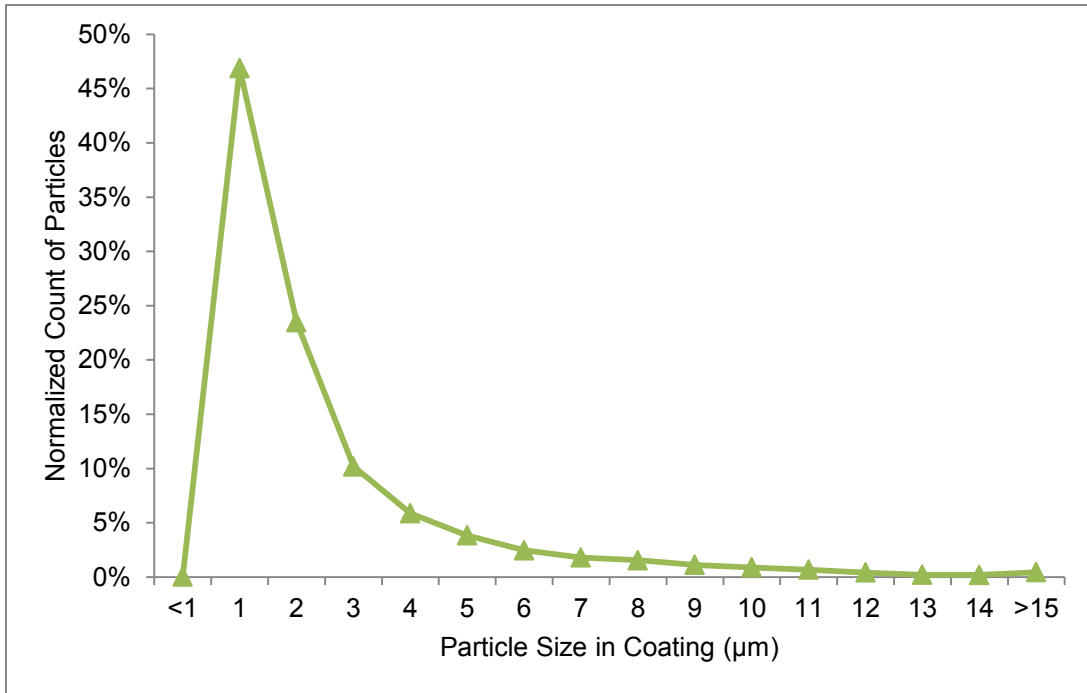
Figure 17: WC particle size distribution of the WC-Ni coating fabricated from
92wt.% WC + 8 wt.% Ni in the powder blend

Table 4: Weighted average of reinforcing carbide particle diameter in the cold-sprayed MMC coatings

	Mean diameter in powder (μm)	Weighted average particle diameter in the fabricated coatings (μm)		
		50 wt.% carbide + 50 wt.% Ni	75 wt.% carbide + 25 wt.% Ni	92 wt.% carbide + 8 wt.% Ni
B$_4$C	39 ± 10 (n = 42)	3.3 ± 2.9 (n = 4516)	3.0 ± 2.7 (n = 12560)	2.6 ± 2.4 (n = 28294)
TiC	23 ± 7 (n = 28)	2.3 ± 1.9 (n = 2393)	2.0 ± 1.7 (n = 7044)	2.4 ± 2.2 (n = 10736)
WC	36 ± 11 (n = 56)	2.7 ± 2.3 (n = 1432)	2.6 ± 2.3 (n = 2924)	2.5 ± 2.4 (n = 7690)

The deposition efficiency was investigated by comparing the reinforcing particle weight percentage within the coating versus the content of carbide in the powder blend. Figure 18 shows

the graphs of carbide content in the coating versus the carbide content in the powder. There is a significant loss of carbide content during the cold spraying process, this is due to the carbide particles rebounding from the surface, fracturing upon impact, and not causing sufficient plastic deformation to promote mechanical interlocking to adhere to the surface. As shown in Fig. 18, the weight percentage of the reinforcing particles within the coating increased by increasing the carbide content in the feedstock powder. This trend has also been reported in previous studies on cold-sprayed MMC coatings [16,18,19,59]. The volume percentages of carbide content was also evaluated (see Fig. 19) and a trend similar to that of Fig. 18 was observed, namely that increasing carbide content in the feedstock powder led to an increase in carbide content in the fabricated coating. The highest deposition efficiency at a given weight and volume percentage was obtained for the WC particles, whereas, the B_4C particles showed the lowest deposition efficiency.
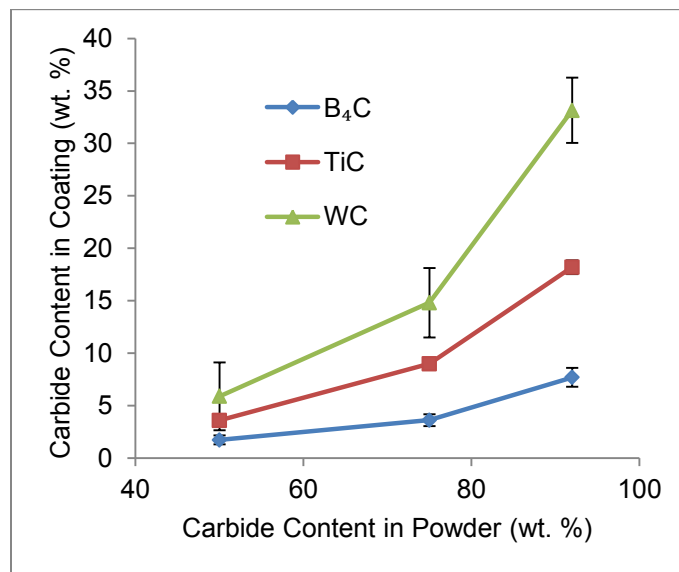
Figure 18: Curves of reinforcing carbide particle content in the coating versus
carbide particle contents in the powder (weight percentage)

44
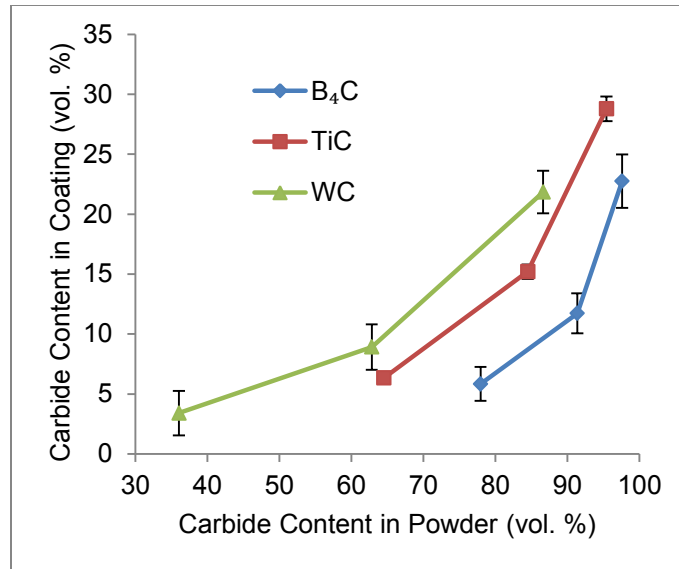
Figure 19: Curves of reinforcing carbide particle content in the coating versus carbide particle contents in the powder (volume percentage)

A comparison of the carbide velocity (see Fig. 13) and the deposition efficiency (see Fig. 18) illustrates that there is no direct correlation between velocity and deposition efficiency. This is in contrast to what has been reported in previous studies [38]. However, the WC particles had the highest momentum (see Table 3) and the highest deposition efficiency of reinforcing particles in cold-sprayed MMC coating. This behavior emphasizes on the possible relationship between momentum and deposition efficiency. On the other hand, the low momentum TiC particles (see Table 3) had higher deposition efficiency than B$_4$C carbides (see Fig. 18). This suggests that other parameters in addition to particle momentum affect deposition efficiency of the carbide particles.

The mechanical properties of the carbide particles, specifically fracture toughness, may also influence the deposition efficiency. Higher resistance to fracture can improve deposition

45

efficiency by allowing more carbide particles to be embedded into the cold-sprayed coating rather than fracturing and rebounding from the surface. To investigate the effect of the carbide fracture toughness on the deposition efficiency, the theoretical fracture toughness values of the bulk carbide materials [66] (see Table 5) were compared with the deposition efficiency presented in Fig. 18. The comparison showed that the carbide particles with higher fracture toughness had higher deposition efficiency. In the impact of carbide particles with higher fracture toughness, the carbide can resist fracturing to allow for higher plastic deformation of the surface and particle embedment. The penetrated carbides along with the plastic deformation can increase the surface roughness to allow for easier adhesion of the incoming powder particles. Higher surface roughness enhances deposition efficiency by facilitating the mechanical interlocking required to cause adherence of subsequent particles. This discussion about the effect of fracture toughness on deposition efficiency explains the lower deposition efficiency of B_4C than that of TiC, despite the higher momentum of the B_4C particles (see Table 3). Due to the lower fracture toughness of the B_4C particles, they experienced higher fracturing and rebounding from the surface, which negatively affected their deposition efficiency.

Table 5: Mechanical properties of the studied carbide particles

	Hardness (kg/mm^2)	Fracture Toughness (MPa m$^{0.5}$) [66]
B_4C	3900 [42]	2.5-3.6
TiC	2900 [42]	3.5-4.5
WC	2300 [43]	5.5-7.5

In addition to carbide particle fracture upon impact, which resulted in a reduction of carbide particle size and low deposition efficiencies, carbide particle fracture within the deposited coating was also observed. An investigation of high magnification images of the

deposited coating and powder cross sections was conducted (see Figs. 20 – 23). The TiC-based coating cross section (see Fig. 20) showed that the TiC particles contained dark jagged voids. The voids may have been due to pulled-out fragments of fractured TiC particles. Additionally, in the WC-based coating cross-sections (see Fig. 21) there were cracks in the WC particles. Therefore, the presence of the voids in the deposited TiC particles and the cracks in deposited WC particles may be evidence of carbide particle fracture. The original powder cross sections (Figs. 22 and 23) show no evidence of dark jagged voids or cracking. Therefore, these void and cracks were not due to the powder manufacturing process. The occurrence of the particle pull-out and cracks found in the deposited carbide particles and not the original carbide particles suggest that the impingement of high momentum particles during the cold spraying process may have been the cause of cracking within the deposited carbide particles.
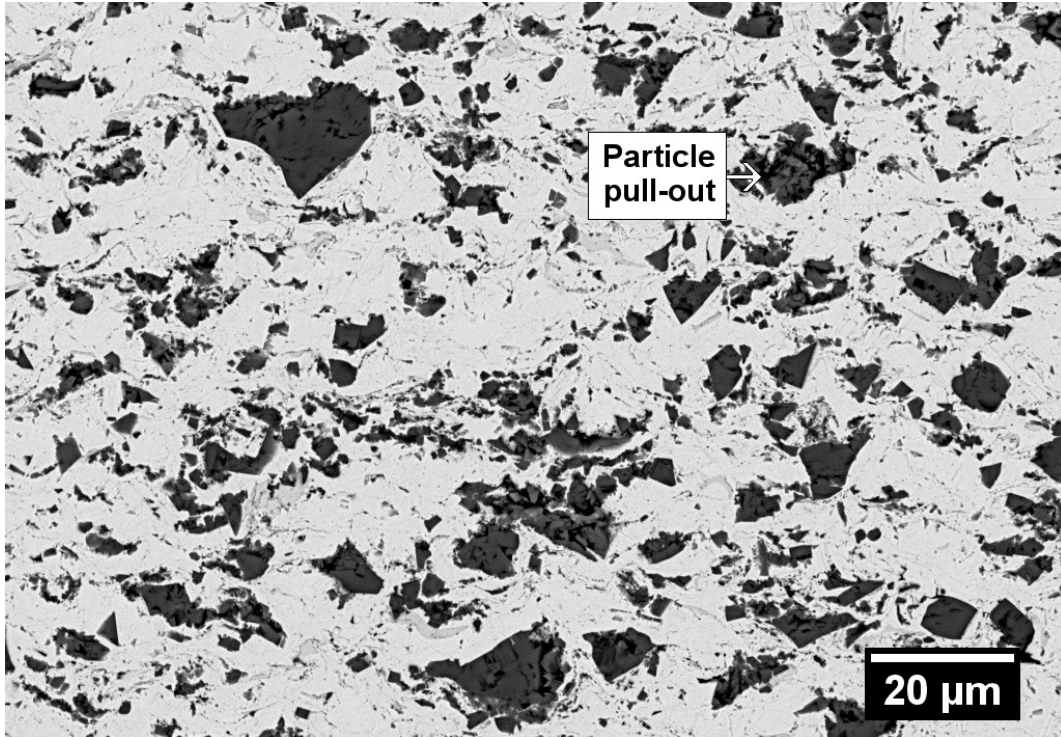
Figure 20: High magnification, 2000X, BSE image of the MMC coating microstructure fabricated from 92 wt.% TiC + 8 wt.% Ni in the powder blend
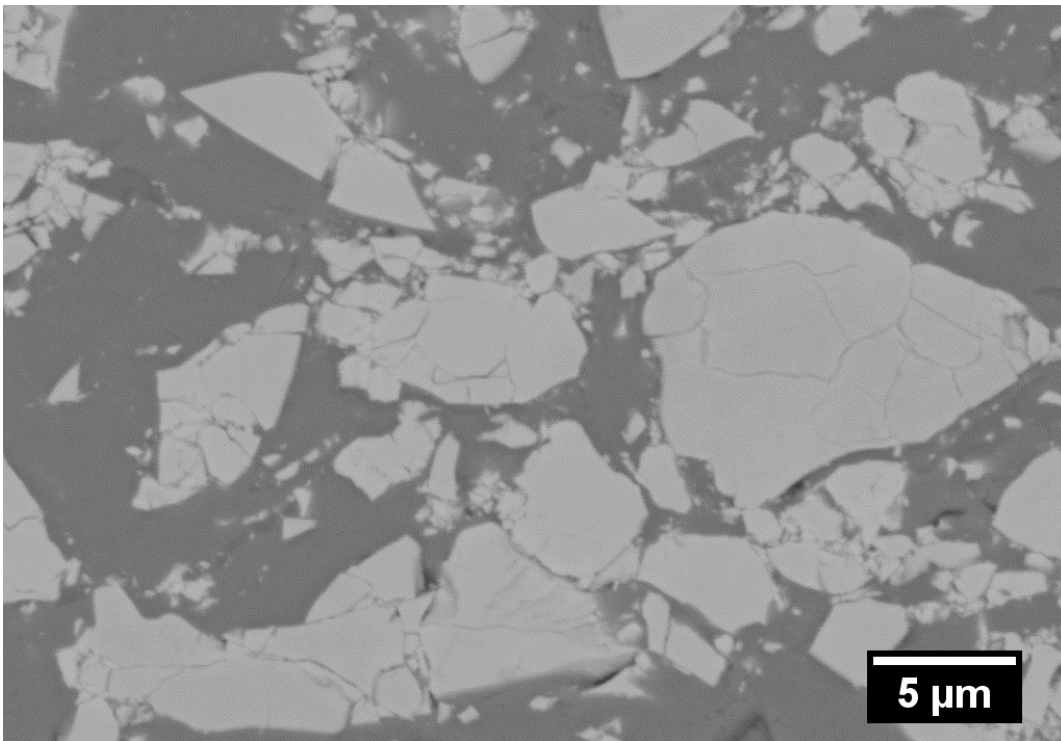
Figure 21: High magnification, 8000X, BSE image of the MMC coating microstructure fabricated from 92 wt.% WC + 8 wt.% Ni in the powder blend
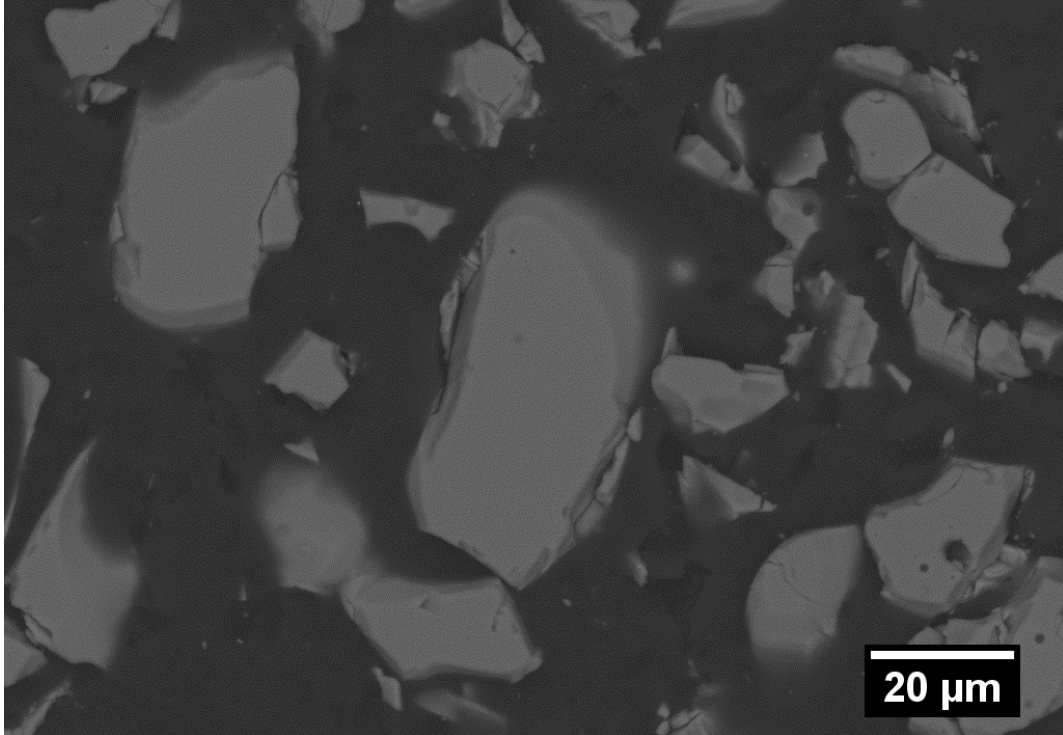
Figure 22: High magnification, 2000X, BSE image of the TiC powder
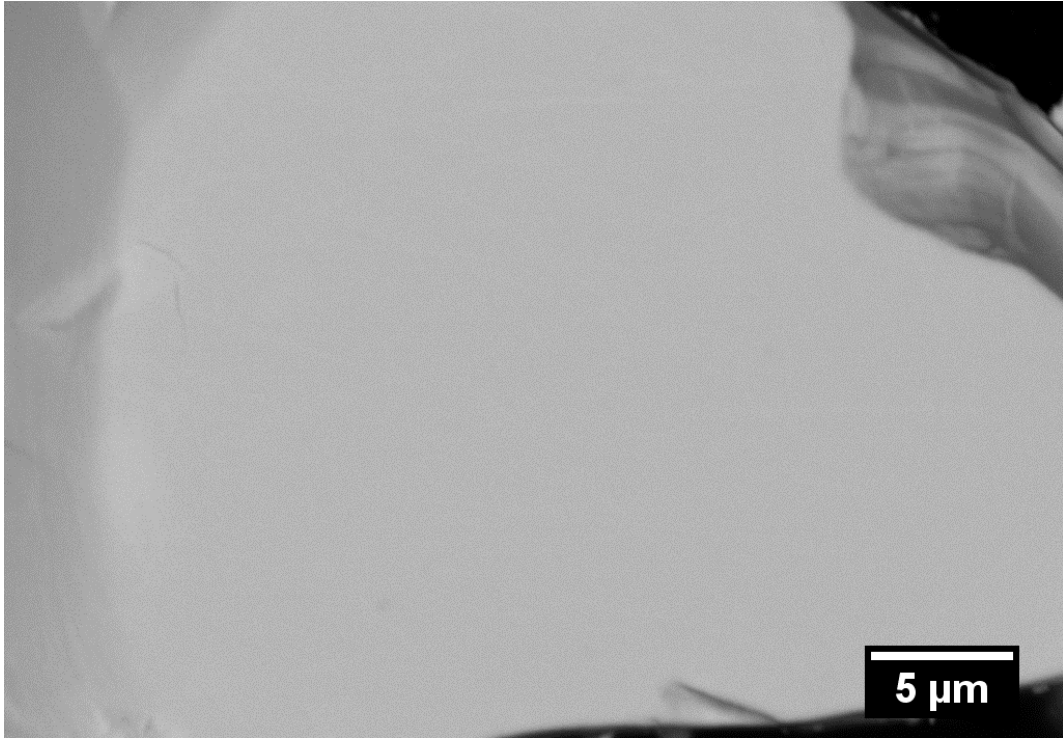
Figure 23: High magnification, 8000X, BSE image of a WC particle

4.3.2 Porosity

Image analysis was also used to evaluate the porosity of the coatings. Figure 24 shows the porosity in the TiC- and WC-based MMC coatings. The B_4C-based coatings were not evaluated for porosity due to the low contrast difference between B_4C particles and pores on the SEM micrographs (see Fig. 14). Figure 24 shows two contrasting trends, porosity increases with increasing TiC reinforcing particle but decreases with increasing WC reinforcing particles. In order to measure porosity the image analysis software counts any area darker than a set intensity as a pore. The software does not distinguish between pores and particle pull-out, which both appear as dark areas on a BSE image. In cold spray coatings pores typically follow the intersplat boundaries and are often rounded. Particle pull-out of the carbide powders are typically jagged with well-defined edges. Figure 25 shows examples of pores and particle pull-out. The particle pull-out of TiC particle fragments from the deposited TiC particles (see Fig. 20) was identified as porosity by the image analysis software; therefore, with increasing TiC particle content in the coating, an increase in porosity was also observed. As such the trend of increasing porosity with increasing TiC carbide content is most probably an artifact of particle pull-out during polishing. No voids or pull-out were observed for the WC particle (see Fig. 21) and thus the porosity in the WC-Ni coating was reduced with increasing WC content in the coating. This is evidence that the high momentum WC particles have a compaction effect upon impact with the surface; therefore, densifying the matrix and improving the matrix properties.
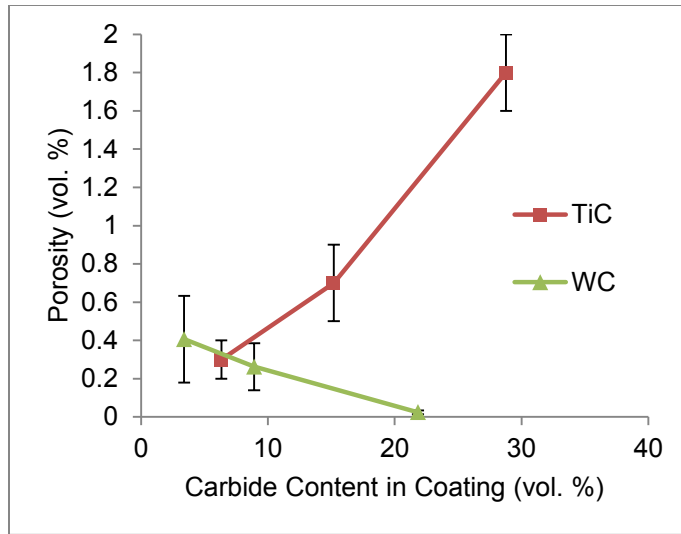
Figure 24: Relationship between porosity and reinforcing carbide particle content in the coating
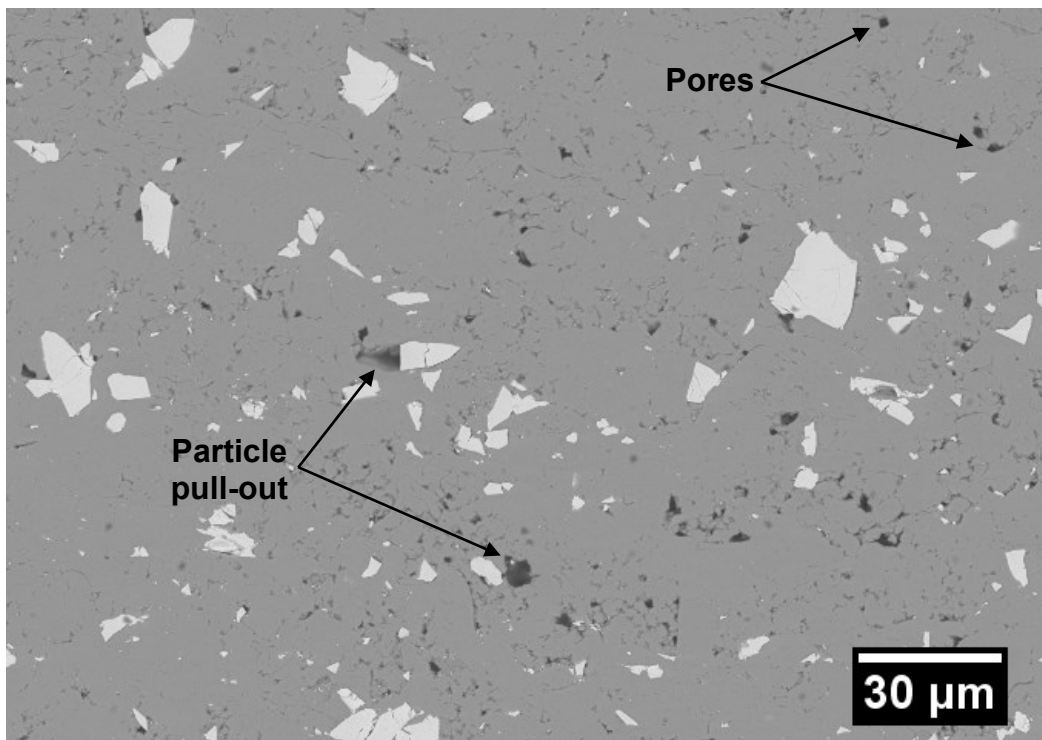
Figure 25: BSE image of the MMC coating microstructure fabricated from
50 wt.% WC + 50 wt.% Ni in the powder blend showing typical pores and particle pull-out

4.3.3 *X-ray Diffraction and Rietveld Refinement*[7]

X-ray diffraction (XRD) was conducted to confirm that no phase change had occurred in the B_4C-Ni coatings. Figure 26 shows the XRD profile for the B_4C powder. There was a broad peak at 26°, which did not match the calculated pattern. The occurrence of this peak may be due to contamination of the B_4C powder. Figure 27 shows the XRD pattern obtained for the B_4C-Ni coating fabricated from 92 wt.% B_4C and 8 wt.% Ni. The B_4C and Ni peaks are identified. A comparison of Figs. 26 and 27 shows that no significant phase change in the B_4C has occurred during the cold spray process. Additionally, Rietveld refinement with quantitative phase analysis was used to corroborate the content of reinforcing B_4C particles in the coatings. The difference between the experimental XRD pattern and the calculated XRD patterns is shown in the gray curve at the bottom of the XRD plots (see Figs. 26 and 27). The results of the Rietveld refinement with quantitative phase analysis are shown on the right of the figures in weight percentages. The quantitative phase analysis by Rietveld refinement of B_4C (9.72 wt.% in Fig. 27) show that the B_4C weight percentage content in the coatings are comparable to the values found using image analysis (8 wt.% in Fig. 18).

---

[7] Portions of the results in this section were obtained in the collaboration with the University of Nottingham; however, the analysis was conducted by Yik Tung Roy Lee
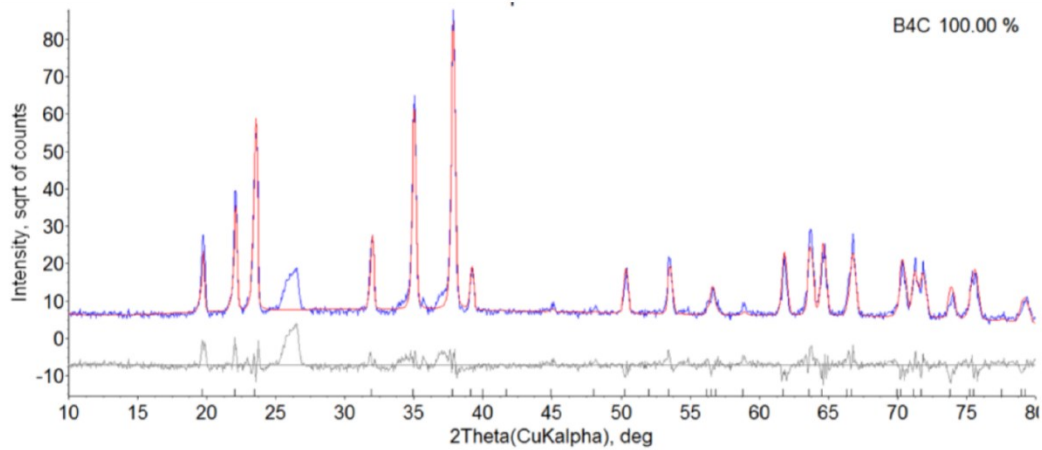
Figure 26: XRD pattern showing Rietveld refinement with quantitative phase analysis of the B_4C powder [54]
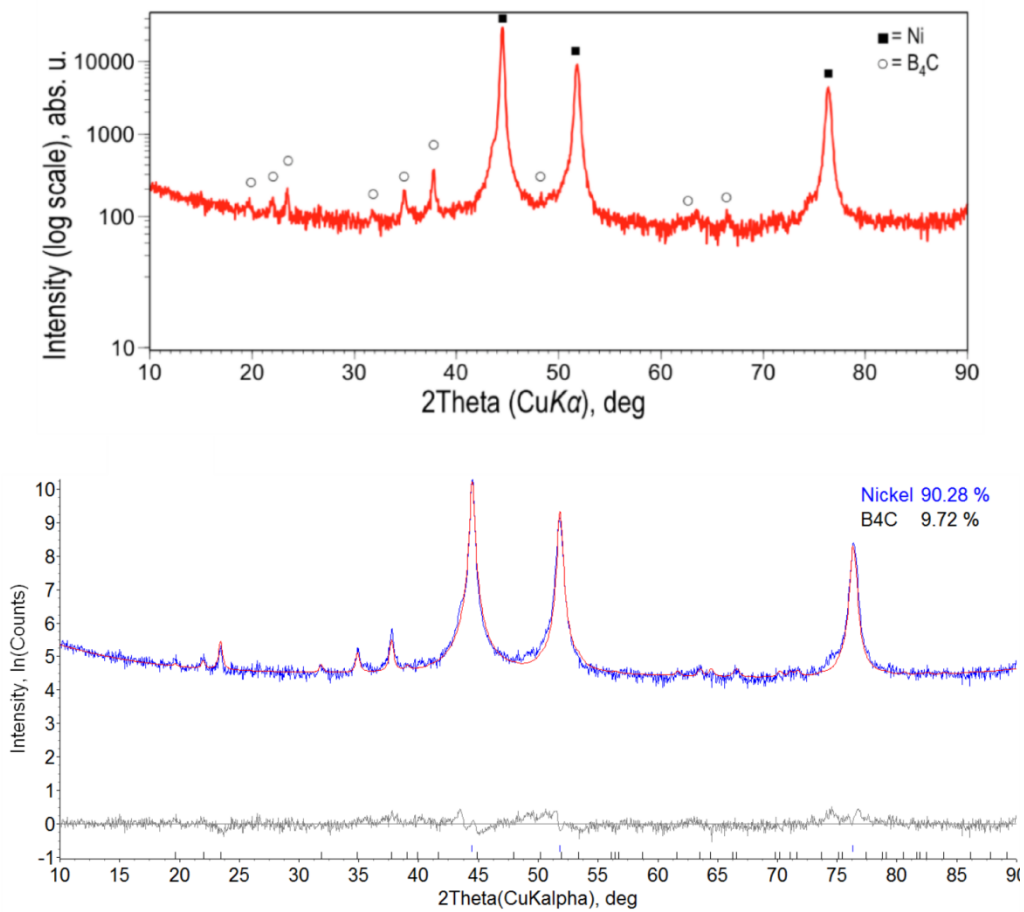
Figure 27: XRD pattern showing peak identification and Rietveld refinement with quantitative phase analysis for the coatings fabricated from 92 wt.% B_4C + 8 wt.% Ni in the powder blend [54]

4.4 Vickers Micro-hardness

The reinforcing particle content in MMC coatings affects their micro-hardness. Figure 28 is a micrograph showing a typical hardness indentation on the cross section a coating, the indentation occurs on top of both the matrix and reinforcing particles. Figure 29 shows the relationship between micro-hardness and carbide volume content for the MMC coatings that were studied. The hardness was increased by increasing the carbide content within the coating. As described in the Introduction, the ROM (iso-strain model) for composite materials states that the hardness of the composite is a weighted average of the hardness of the constituents. Figure 29 also shows the curves associated with the ROM (iso-strain model)[16][15]. The hardness of the low-pressure cold-sprayed Ni matrix was taken as 137 $HV_{0.3}$ [16]. As shown in Fig. 29, two composites with the same matrix and equal volume percentage of reinforcing particles, but different reinforcing particles should not have the same hardness. The composite with the harder reinforcing particle would have higher hardness. A comparison of the ROM (iso-strain model) curves and the experimental hardness of the fabricated coatings (see Fig. 29) shows that the composite coatings deviated from ROM (iso-strain); for a given volume fraction of reinforcing particles, the WC-based MMC coatings had the highest micro-hardness, even though the WC has the lowest theoretical hardness based on ROM (iso-strain). This deviation was more evident at low volume percent of carbides in the coating (see Fig. 29). The high hardness of the WC-based MMC coatings can be attributed to the higher momentum and fracture toughness of the WC particles compared to those of the other two carbides. The higher momentum and fracture toughness of the impacting WC particles resulted in plastic deformation, work hardening and

greater densification of the ductile metal matrix. Therefore, this increased the hardness of the matrix and subsequently, the composite.
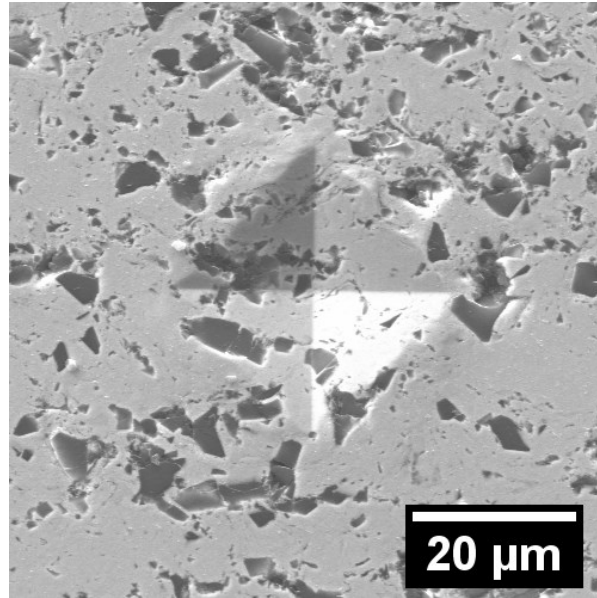
Figure 28: Vickers micro-hardness indentation on the cold-sprayed coating of 92 wt.% B_4C + 8 wt.% Ni MMC powder
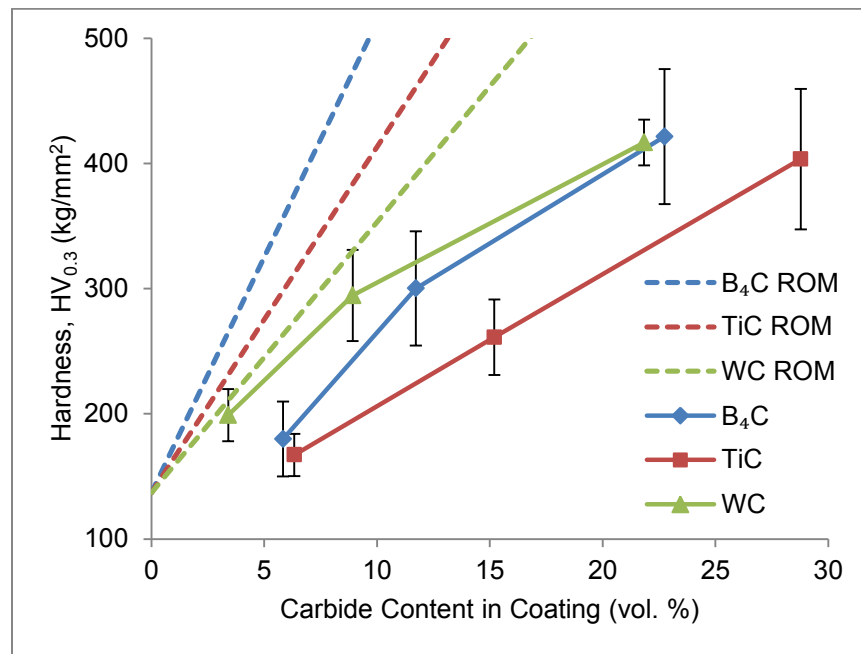
Figure 29: Relationship between micro-hardness of the MMC coating and carbide content in the coating with the upper range of micro-hardness based on ROM

The effect of work hardening and densification of the matrix on the MMC coating hardness was more pronounced in coatings with reinforcing particle volume percent within the range of 3 - 15 vol.% (see Fig. 29). In the coatings with lower volume percent of carbide particles, the mean free path was higher as shown in Fig. 30. The larger mean free path resulted in reduced load sharing between reinforcing particles. Consequently, the effect of the reinforcing particles on the hardness of the composite was reduced and the strength of the work-hardened matrix was more prevalent. This was evidenced by the fact that the MMC coatings with 3 vol.% of WC had the highest mean free path and the highest hardness in comparison to the TiC and B_4C MMC coatings with carbide content of 6 vol.% (see Figs. 30 and 31). This shows that the high momentum of the WC particles translated into high impact forces, which had work-hardened and densified the Ni metal matrix, resulting in the higher hardness of the WC-Ni MMC coating that was observed (see Fig. 31).
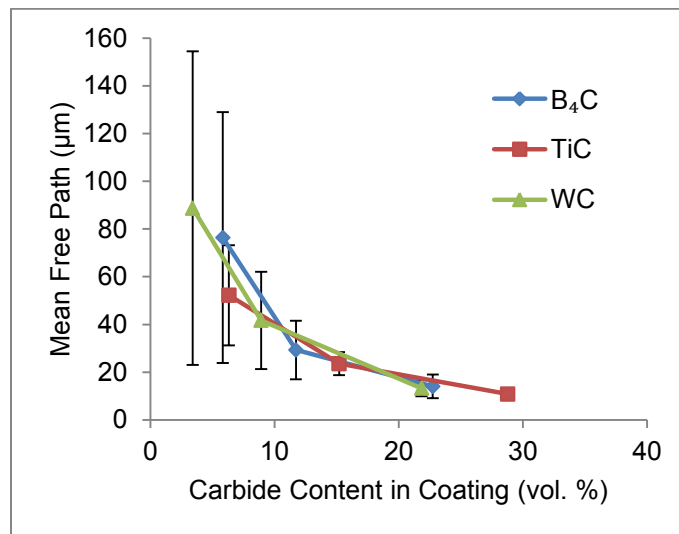
Figure 30: Curves of mean free path between reinforcing particles versus the carbide content in the coating
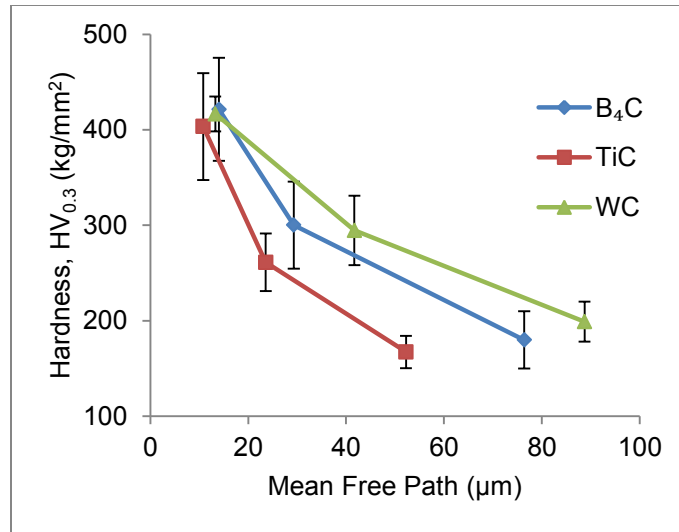
Figure 31: Relationship between micro-hardness and mean free path between reinforcing particles in the coating

Micro-hardness indentations with a load of 50 gf were conducted on the coatings fabricated from 50 wt.% carbide and 50 wt.% Ni to directly investigate the work hardening of the matrix. The low load micro-hardness indentations were targeted at un-reinforced areas of the coating to obtain hardness values of just the matrix. Figure 32 shows a typical indentation that was used to obtain the matrix hardness. Table 6 summarizes the hardness of the matrices within the different coatings. The matrix micro-hardness values (at 50 gf) reported in Table 6 are higher than the hardness values of the composite (at 300gf) (see Fig. 29). This can be attributed to work hardening during the polishing process, which has a greater influence on the shallow 50 gf indentations than the larger and deeper 300gf indentations.

Figure 32: Vicker's micro-hardness indentation (50 gf) on cold-sprayed coating of
50 wt.% B4C + 50 wt.% Ni MMC powder

Table 6: Matrix micro-hardness of the deposited coatings

Coating	Hardness ($HV_{0.05}$)
Ni	142.7 ± 8.1 ($n = 5$)
6 vol.% B_4C + Ni	170.9 ± 18.8 ($n = 5$)
3 vol.% WC + Ni	225.7 ± 25.5 ($n = 6$)
6 vol.% TiC + Ni	269.4 ± 33.1 ($n = 15$)

The obtained matrix hardness values in Table 6 show that there is work hardening occurring in the coatings. Pure Ni, annealed at 700K for 1 hour, has a micro-hardness of approximately 100 $HV_{0.05}$ [67]. The cold spraying of the Ni powder resulted in some work hardening of the metal to increase the Ni metal hardness (see Table 6). Metal work hardening and grain refinement during cold spraying also been found in other studies [68–71]. Further work hardening of Ni is possible. Neishi *et al.* [67] showed that work hardening, by equal-channel angular pressing, of Ni can refine grains from approximately 80 µm to approximately 0.3 µm increased the micro-hardness of Ni to approximately 250 $HV_{0.05}$ [67]. In fact, the Ni matrix was

further work hardened by the impact of the carbide particles. In the B_4C-Ni coating the Ni matrix is harder than in the un-reinforced Ni coating. Additionally, the higher momentum WC particles (see Table 3) resulted in a further increase in the matrix hardness for the WC-Ni coating (see Table 6). However, Table 6 also shows that the TiC-Ni coating produced a matrix hardness higher than that of the WC coating, despite the low momentum of the TiC particles (see Table 3). Indentations on the un-reinforced matrix were difficult in the TiC coatings. The lower mean free path between reinforcing particles in the 6 vol.% TiC coatings (see Figs. 30 and 31) resulted in some of the 50 gf force indentations occurring in close proximity to or on top of a TiC reinforcing particle (see Fig. 33). The lower mean free path also indicates that more load sharing may occur within indentation area beneath the visible surface. As a result, the reported hardness of the matrix in the TiC-Ni coating was likely influenced by the reinforcing TiC particles and potential load sharing from nearby particles. Therefore, the matrix hardness found within the 6 vol.% TiC coatings may not be representative of that of the un-reinforced matrix of the coating. The results from the B_4C-Ni, WC-Ni, and Ni coatings show that the carbides have a work hardening effect on the Ni matrix and that higher momentum carbides can increase this work hardening effect.
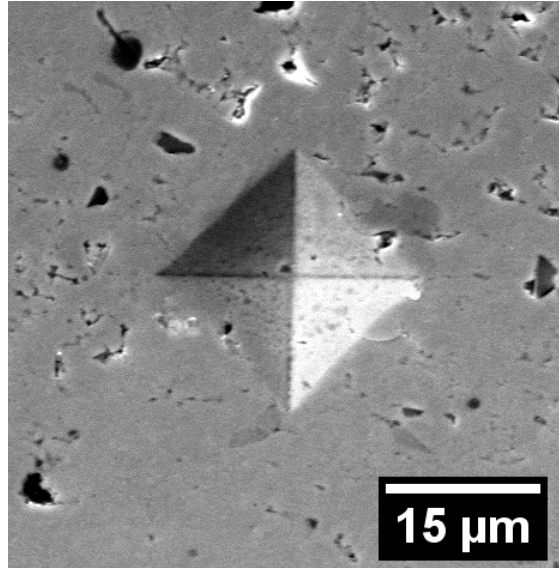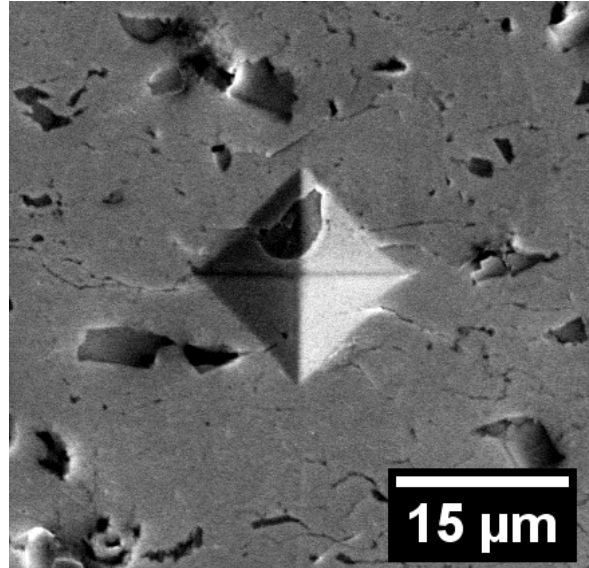
Figure 33: Vicker's micro-hardness indentation (50 gf) on cold-sprayed coating of 50 wt.% TiC + 50 wt.% Ni MMC powder

4.5 Dry abrasion testing

The abrasive wear resistance of the deposited MMC coatings was evaluated according to the provisions and procedures outlined in ASTM Standard G65 (2010) [52]. Figure 34 shows the graphs of the wear rate versus the hardness of the MMC coatings. The wear rate was higher at lower hardness values for each MMC coating type. This was expected since the coatings with higher hardness values had higher carbide content (see Fig. 29) to protect the matrix from scratching and grooving by the abrasive sand. The reinforcing particles act as an obstacle against the abrasive sand particles and force them to change their path. In addition, the coatings with higher hardness had lower mean free path (see Fig. 31) and improved load sharing between reinforcing particles. This reduced the penetration of the sliding abrasive sand into the coating. Thus, increasing reinforcing particle content and lowering mean free path will increase hardness

and improve wear resistance of the MMC coatings. This was also observed by Melendez, *et al.* [10] and Saito, *et al.* [72] while studying the wear rates of WC-based MMC.
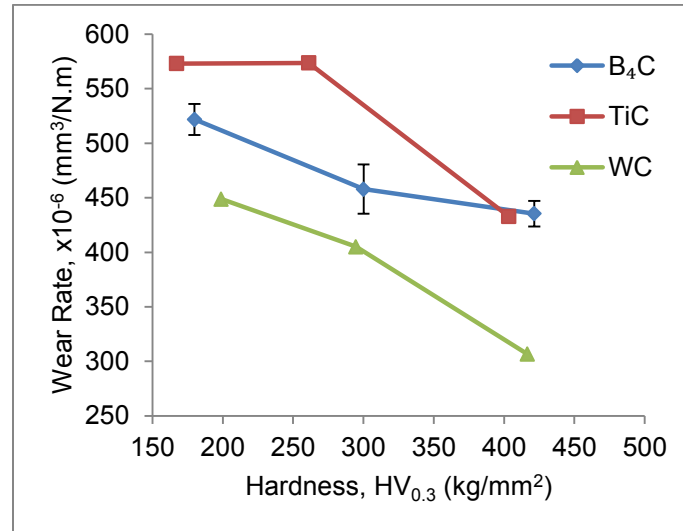
Figure 34: Curves of the MMC coating wear rates versus the micro-hardness of the coatings

4.5.1   *Wear Scar Analysis*

Figure 34 showed that MMC coatings with similar hardness had different wear rates. Although part of that difference could be attributed to the use of different materials to line the wheel for the tests, identification of the material removal mechanism of the abraded coatings can explain the variation in wear rates observed for the different types of MMC coatings. To study the material removal mechanism, SEM images of the abraded surfaces were captured and analyzed. Figures 35 – 37 show the worn surfaces of the lowest carbide content coatings fabricated from the 50 wt.% carbide and 50 wt.% Ni powder blend, specifically, the coatings have 6 vol.% B_4C, 6 vol.% TiC, or 3 vol.% WC. There were many grooves or scratches that can

be observed in the worn surfaces, which are indicative of the microploughing and microcutting mechanisms. Microploughing and microcutting result from the abrasive sand sliding along the surface while being pressed into the surface. This action generally results in plastic deformation, which is shown in the form of scratches or grooves.

Figure 35: Secondary electron image of the abraded coating surfaces fabricated from 50 wt.% B_4C + 50 wt.% Ni in the powder blend

Figure 36: Secondary electron image of the abraded coating surfaces fabricated from 50 wt.% TiC + 50 wt.% Ni in the powder blend
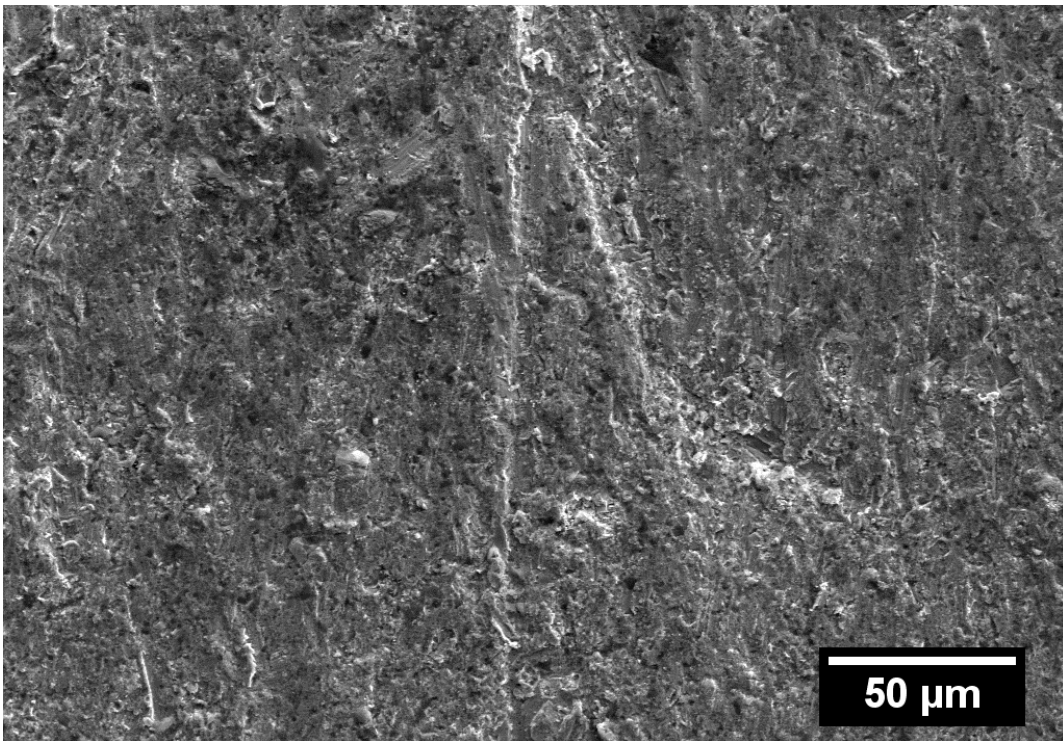
Figure 37: Secondary electron image of the abraded coating surfaces fabricated from 50 wt.% WC + 50 wt.% Ni in the powder blend

There was evidence of microploughing and microcutting in all the worn surfaces shown in Figs. 35 – 37. However, the grooves and scratches are most noticeable in the TiC-based coating (see Fig. 36). This suggests that the abrasive sand penetrated further into the composite coating during wear testing, resulting in a deeper and more pronounced grooves and scratches. Therefore, this TiC-based coating has a higher wear rate, as indicated in Fig. 34. In the case of the worn WC-based MMC coating surface there was one deep scratch in addition to the grooves and scratches indicative of microploughing and microcutting. The deep scratch may be the result of the lower volume loading of reinforcing particles in the WC-based coating, at 3 vol.% versus the 6 vol.% in B_4C- and TiC-based MMC coatings. The lower content of reinforcing particles in a region of the coating will result in higher rates of material removal in that region. However, despite the lower volume loading and the localized areas of higher removal rates, the 3 vol.% WC-based MMC coating still has a lower overall wear rate than that of the 6 vol.% B_4C-based MMC coating, as shown in Fig. 34. The backscattered electron micrographs in Figs. 38 – 40 allow for a possible explanation for the lower wear rates of the 3 vol.% WC + Ni. There are trails of small WC particles that follow the large WC particles (see Fig. 40). These trails are not as prominent in the B_4C- and TiC-based MMC coating Figs. 38 and 39. This suggests that there was dispersal of the WC particles during the abrasive wear. This may result in a decrease in the wear rates of the coating, due to increased volume content of reinforcing particles at the surface of the coating. The higher volume content of reinforcing particles at the surface provides increased load sharing, thereby, decreasing the wear rates.
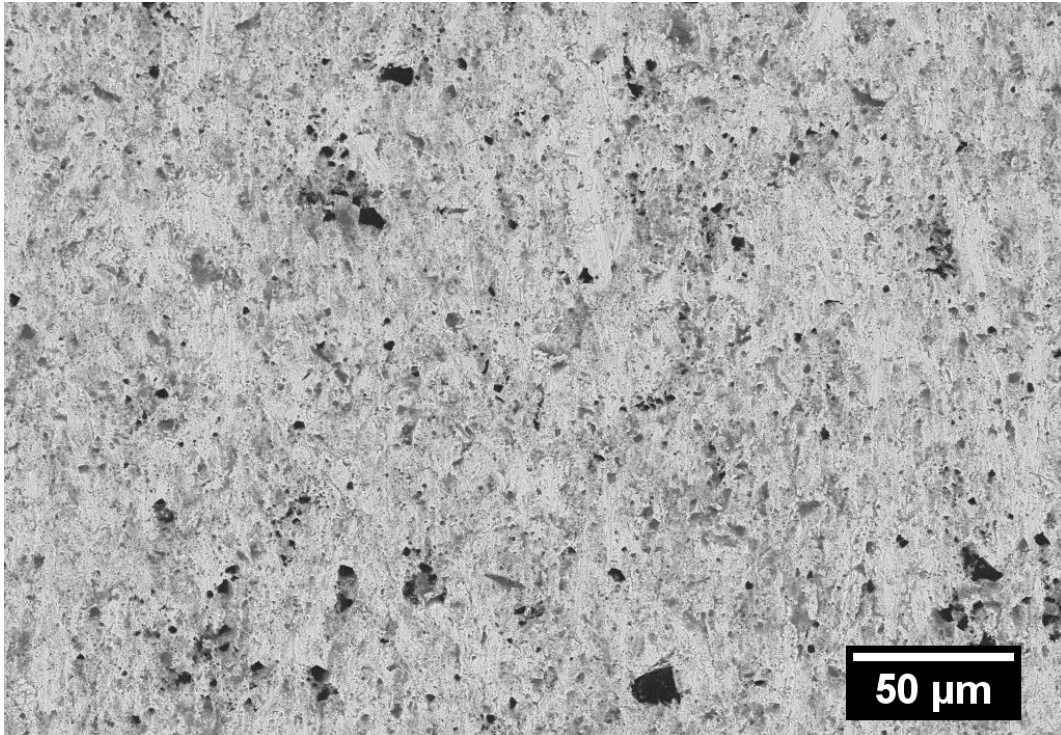
Figure 38: BSE image of the abraded coating surfaces fabricated from
50 wt.% B$_4$C + 50 wt.% Ni in the powder blend
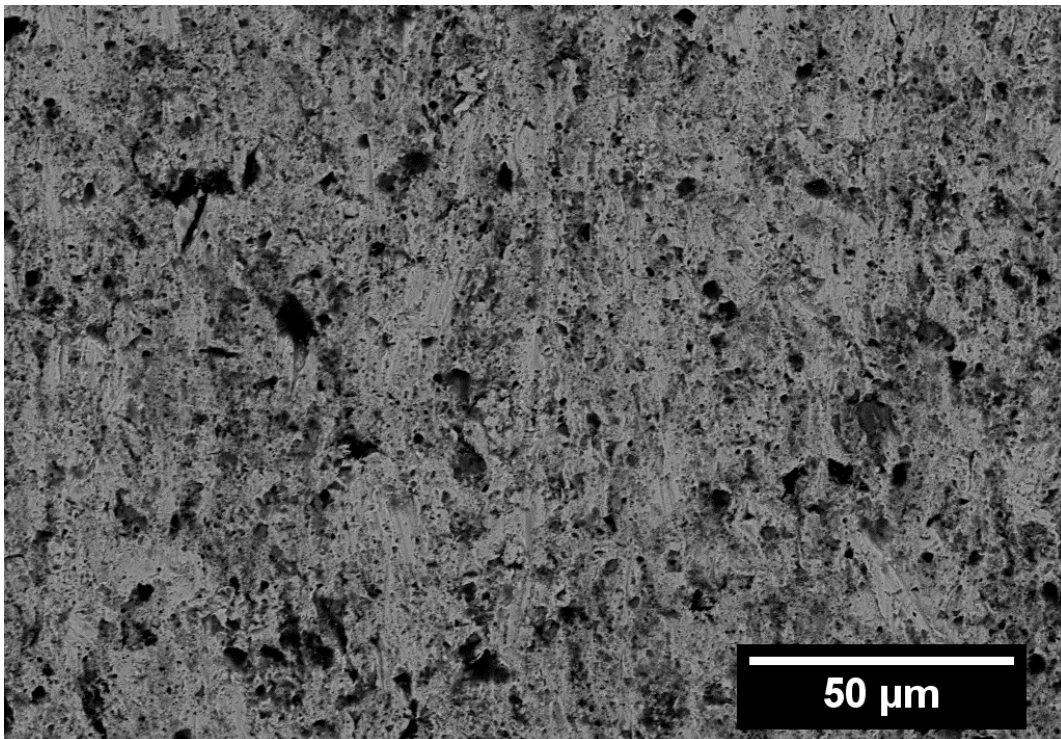
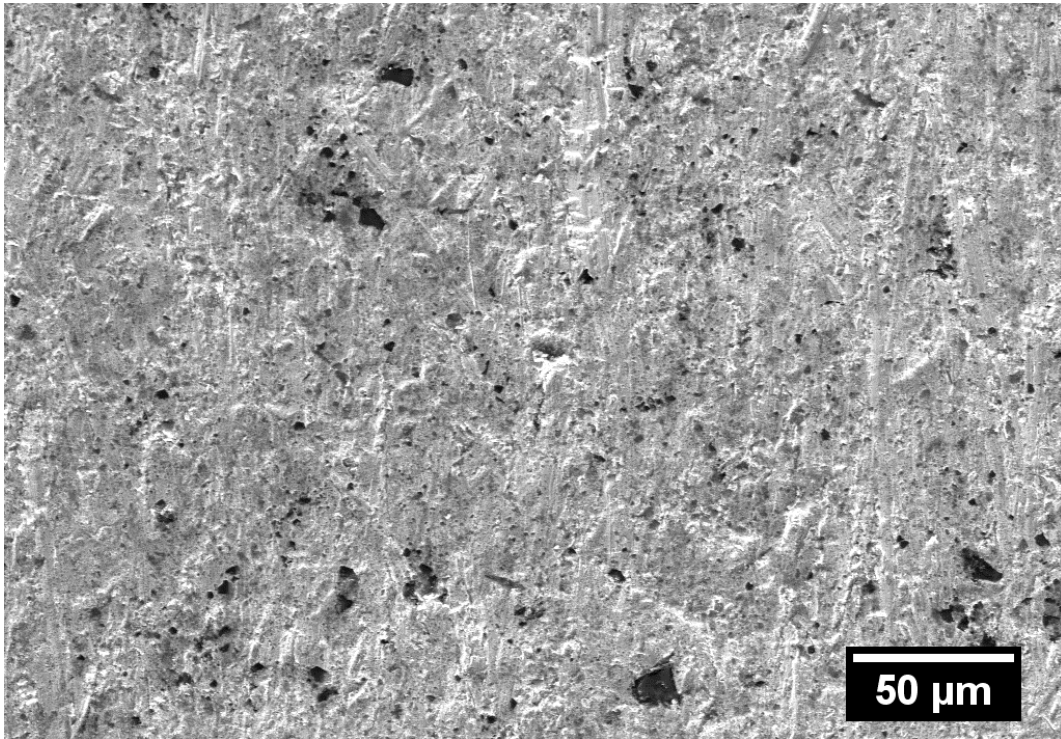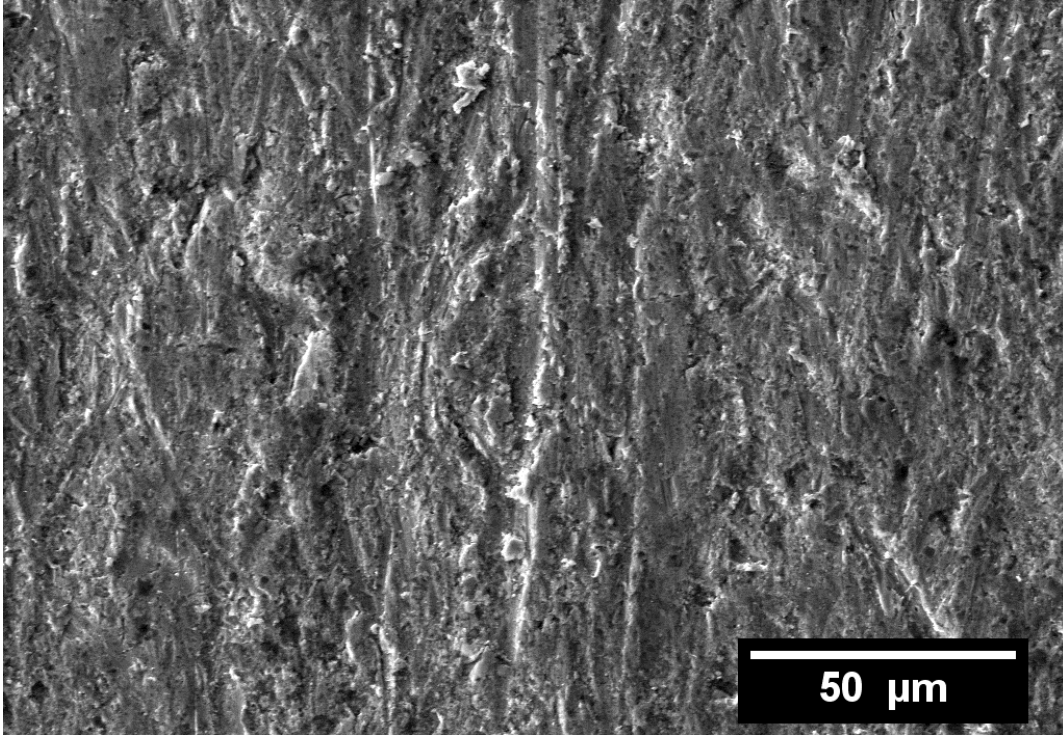**Figure 39**: BSE image of the abraded coating surfaces fabricated from
50 wt.% TiC + 50 wt.% Ni in the powder blend
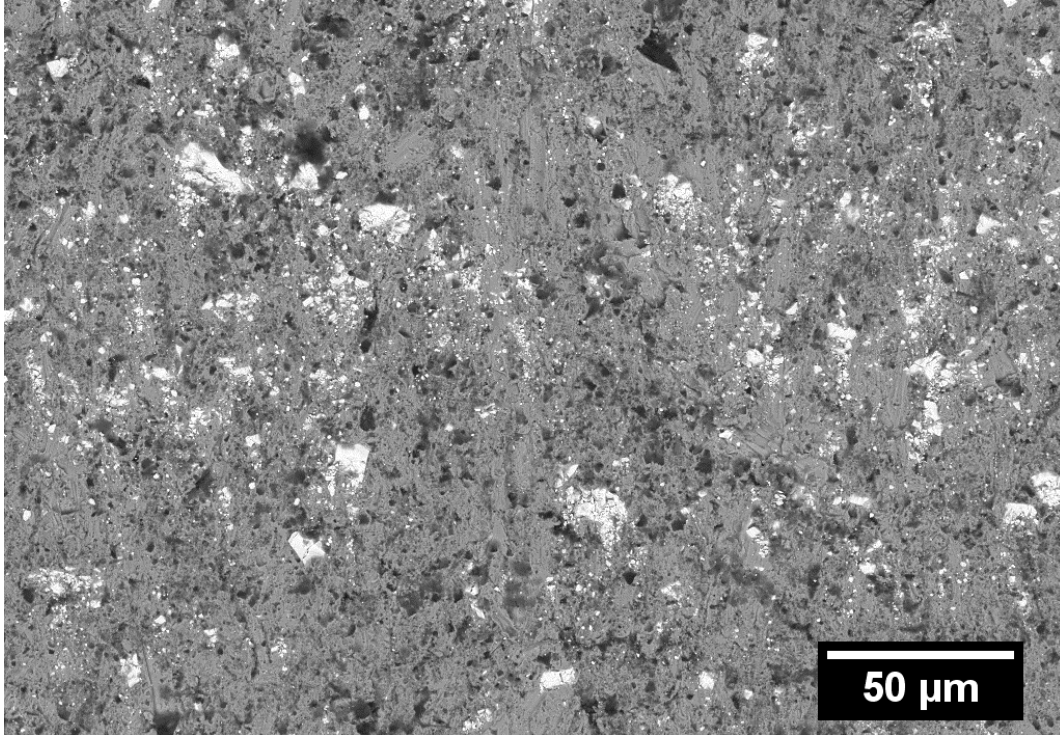
Figure 40: BSE image of the abraded coating surfaces fabricated from
50 wt.% WC + 50 wt.% Ni in the powder blend

Figures 41 – 43 show the worn surfaces of the coatings that were fabricated with 92 wt.%

carbide + 8 wt.% Ni powder blend. That powder blend produced MMC coatings with carbide

content of 23 vol.% B_4C, 29 vol.% TiC, and 22 vol.% WC. Grooves and scratches are also

observed on the worn surfaces (see Figs. 41 – 43) which suggested that microcutting and

microploughing were the major material removal mechanisms for all the MMC coatings.

Comparison of the scratches and grooves shown in the TiC-based MMC coating (see Fig. 42) to

those shown in the WC-based MMC coating (see Fig. 43) indicated deeper and longer wear scars

in the TiC-based MMC coating. This observation can be explained by comparing the momentum

values of the impacting carbides during the fabrication process. Higher momentum of the

particles and the impact force had a work hardening effect, which strengthened the metal matrix.

The momentum of the WC particles was higher than that of the TiC particles, which resulted in a stronger matrix for the WC-based coatings. This allowed for reduced penetration of the abrasive sand particles into the metal matrix of the WC-reinforced coating, reducing the wear rates of the WC-based MMC coatings (see Fig. 34). The compaction effect of the high momentum particles improved the adhesion of the reinforcing particles in the coating, which was shown by the presence of the B_4C and WC particles in the worn surface (see Figs. 41 and 43). For the TiC particles, which possessed lower momentum, they were less discernable in the wear scars (see Fig. 42). It appears that most of the TiC particles were removed from the surface. In fact, with high magnification images discussed during the evaluation of porosity (see Figs. 20 and 21), it was observed that the TiC particles contain voids or particle pull-out (see Fig. 20). This suggests that the TiC particles were highly fractured upon impact with the surface, such that they were even being removed during the polishing process as evidenced by the particle pull-out observed in the SEM image taken at 2000 times magnification (see Fig. 20). This same behavior was not observed for the WC particles of which cracks were visible at 8000 times magnification image (see Fig. 21). The cracked WC particles were not removed from the polished surface, which may be caused by the higher compaction of the coating due to the high momentum of the WC particles, therefore the coatings have higher compressive stresses which retains the WC particles. As a result the TiC particles were easily removed during wear tests resulting in high wear rates and the WC particles were retained in the coating and decreased wear rates.
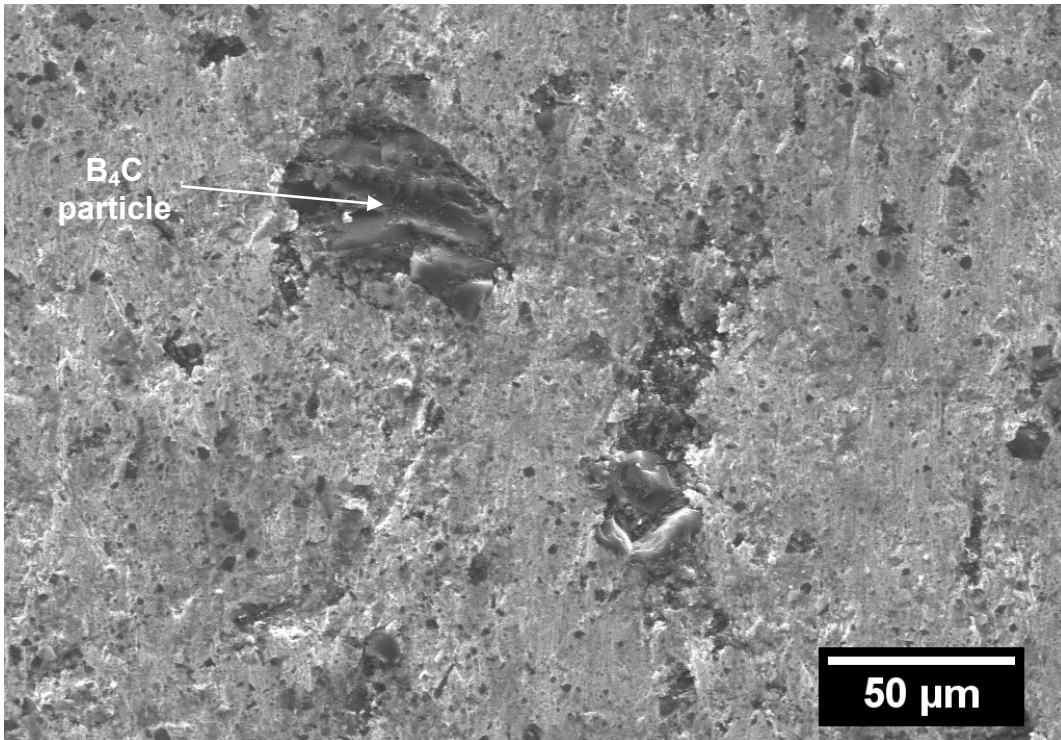
Figure 41: Secondary electron image of the abraded coating surfaces fabricated from 92 wt.% B_4C + 8 wt.% Ni in the powder blend
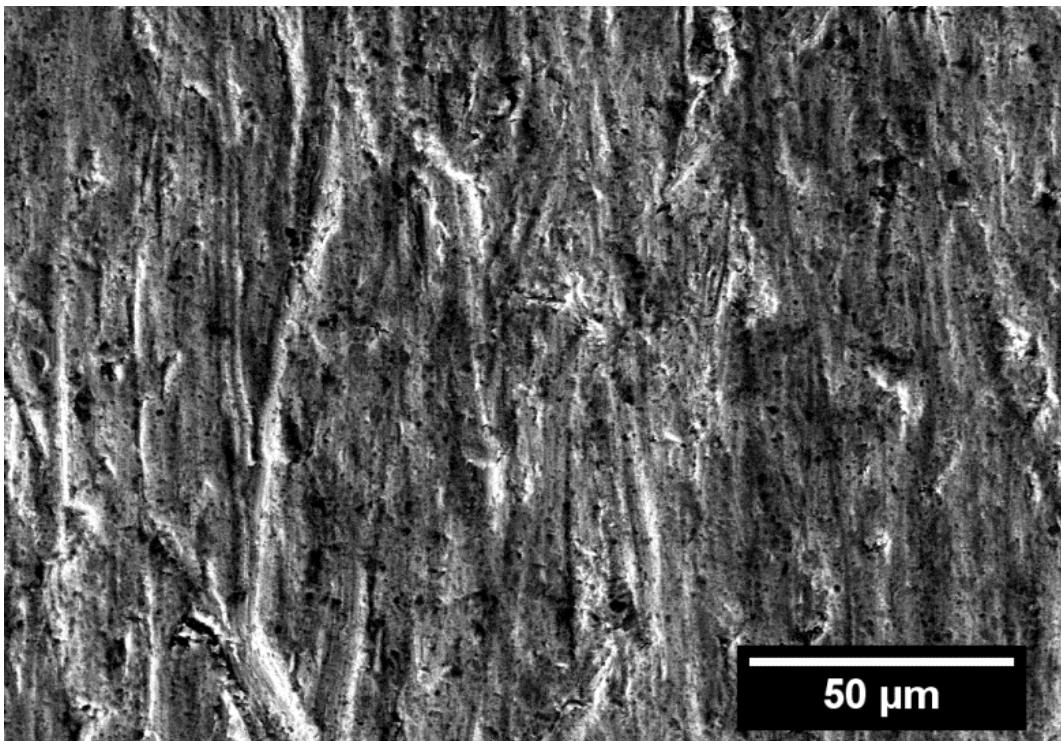
Figure 42: Secondary electron image of the abraded coating surfaces fabricated from 92 wt.% TiC + 8 wt.% Ni in the powder blend
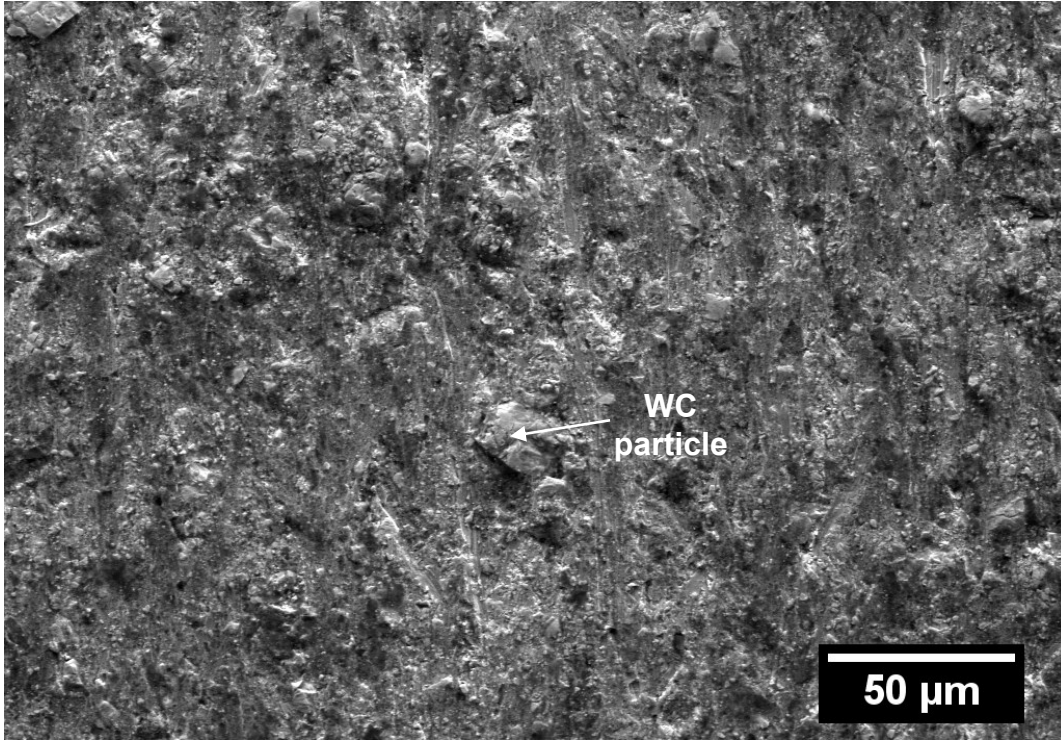
Figure 43: Secondary electron image of the abraded coating surfaces fabricated from 92 wt.% WC + 8 wt.% Ni in the powder blend

The fracture toughness of the carbide particles was identified as another parameter affecting the wear rates of the MMC coatings. The abraded surfaces of the WC-based MMC coating showed that WC particles protruded from the worn surface (see Fig. 43). This behavior was most likely due the high fracture toughness of WC particles (see Table 5). This observation suggested that these particles were not breaking upon collision with the abrasive sand and were diverting the path of the abrasive sand particles, resulting in reduced wear rates of the WC-based MMC coatings. In the case of the MMC coatings with the reinforcing particle that had the lowest fracture toughness, the B_4C-based composites, there was evidence of particle fracture on the abraded surface (see Fig. 41). The fractured reinforcing particles indicated that the carbides

mechanically failed upon collision with the abrasive sand resulting in higher wear rates than that observed for the WC-based composite.

Overall, the wear scars have shown that there are many factors that affect the wear rate of the cold-sprayed MMC materials. It has been shown that the WC particles are leaving trails of small particles on the worn surface (see Fig. 40). The high momentum of the impacting carbide particles had a work hardening effect that was strengthening the matrix and reducing the amount of microcutting and microploughing. However, even with these improvements the wear rates found in this study do not compare to those found by Melendez *et. al* [10] which are an order of magnitude lower (20 x 10^{-6} mm^3/N.m) at similar hardness values. As such, an investigation of the fracture behavior was completed to investigate the difference between the MMC coatings of this study and the WC-Co-Ni coating developed by Melendez *et. al* [10].

4.6 Four Point Bending with Acoustic Emission[8]

Four point bending test were conducted to investigate the fracture behavior of the cold-sprayed MMC coatings. The acoustic emission from the test was collected and an energy value was calculated for each acoustic event. The total energy released was represented by a cumulative absolute energy parameter with units of aJ (10^{-18} J) [54]. Figures 44 – 47 show the cumulative energy measured from the four point bending tests. The maximum energy for all of the B$_4$C-Ni (see Fig. 45) and Ni (see Fig. 46) coatings was on the order of 10^4 aJ, this was in the

---

[8] The results in this section were gathered by Mr. Mohamed Shibly and analyzed by Yik Tung Roy Lee

same order as the uncoated substrate (see Fig. 47). This suggests that the B_4C-Ni MMC coatings have a fracture behavior similar to that of an unreinforced metal. The maximum energy for the WC-Co-Ni coatings was on the order of 10^{10} aJ (see Fig. 45). This was evidence of brittle fracture behavior in the coating. Under tensile loading, brittle MMC coatings (WC-Co-Ni) experience stress accumulation at defects. When a critical stress is obtained, the crack grows and propagates until it reaches a reinforcing particle where the crack tip is blunted. A blunted crack tip reduces stress concentration and limits further failure until more strain is applied to the coating. The sudden release of the accumulated stress in the tip of crack releases energy in the form of sound which is then collected by the acoustic transducers. Therefore, brittle coatings show the high cumulative energy values from the onset of failure and strain to failure can easily be determined as ~0.5 %, as shown in Fig. 45. Conversely, ductile MMC coatings will plastically deform under stress and prevent stress concentration. As a result, ductile MMC coatings (B_4C-Ni) do not experience a sudden release of accumulated stress and high acoustic energy was not measured for these coatings, as shown in Fig. 44. No strain to failure value can be established for the ductile samples (see Figs. 44 and 46) as they do not produce significantly more energy than the substrate (see Fig. 47) under the same loading. Sample BC2 in Fig. 44, shows higher cumulative energies than then other coatings; however, the magnitude of the energy was insufficient to imply a different failure behavior. The cumulative energy from sample BC2 could be the result of some inter-splat failures in the coating or simply residual acoustic emission from the rollers settling on the sample surface.
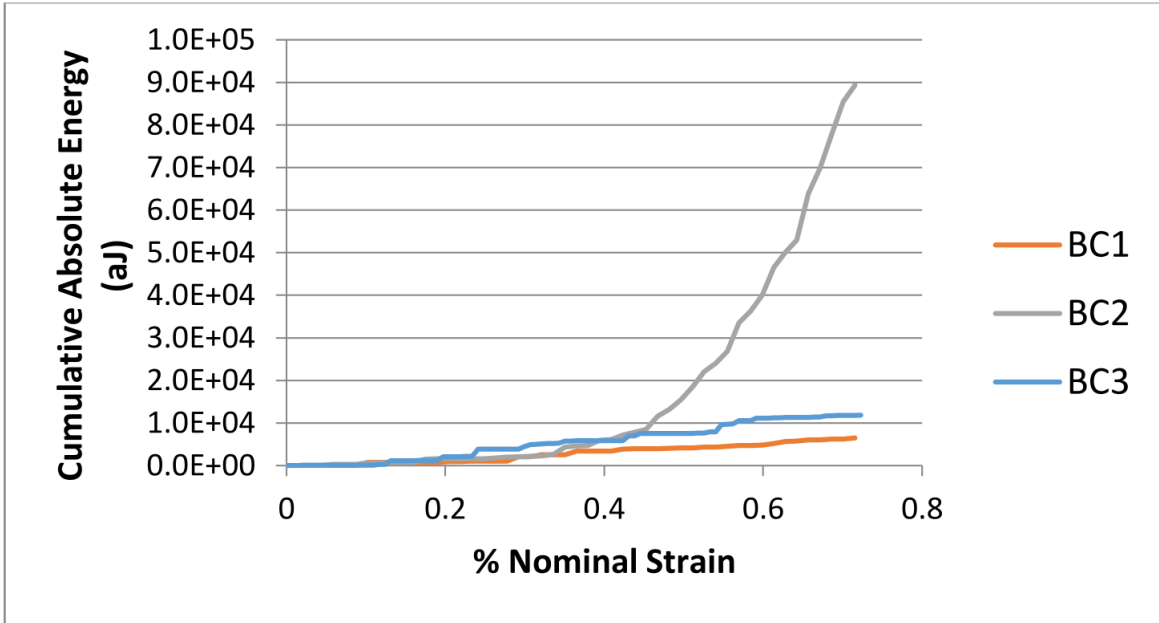
Figure 44: Cumulative energy versus % nominal strain for the coating fabricated from 92 wt.% B$_4$C + 8 wt.% Ni in the powder blend [54]
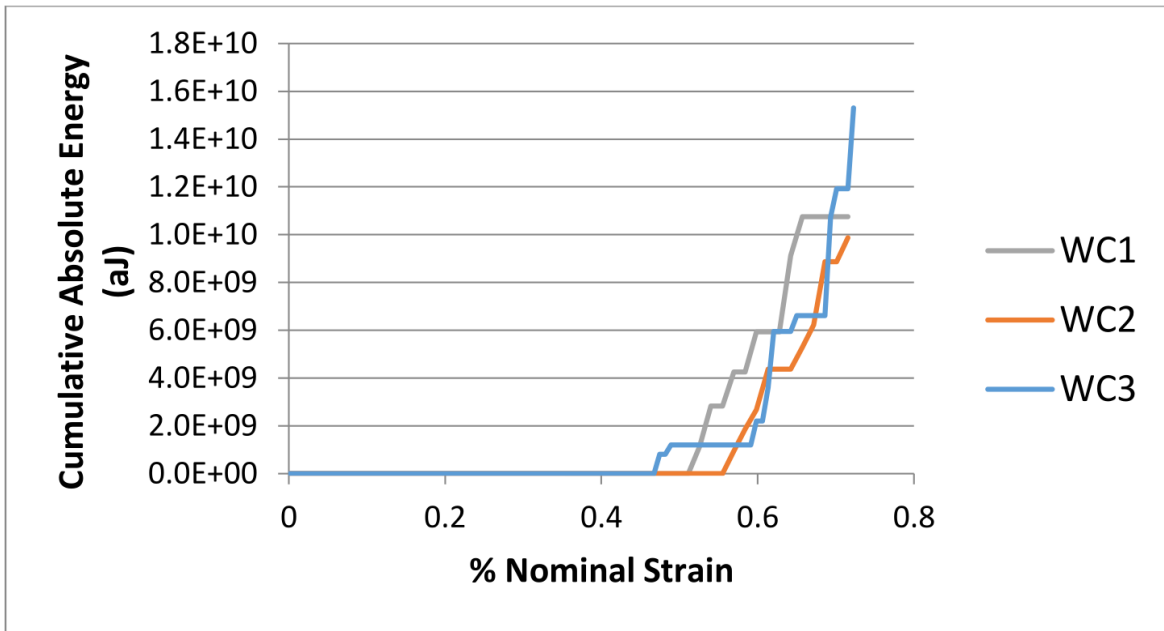
Figure 45: Cumulative energy versus % nominal strain for the coating fabricated from 96 wt.% WC-Co + 4 wt.% Ni in the powder blend [54]
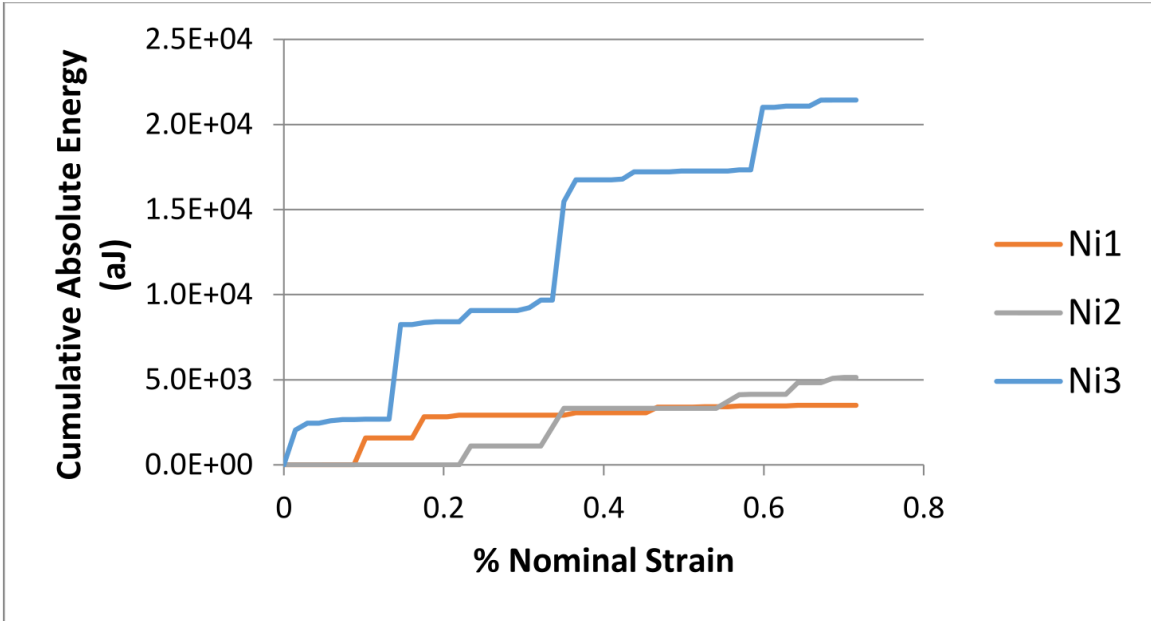
Figure 46: Cumulative energy versus % nominal strain for a cold-sprayed Ni coating [54]
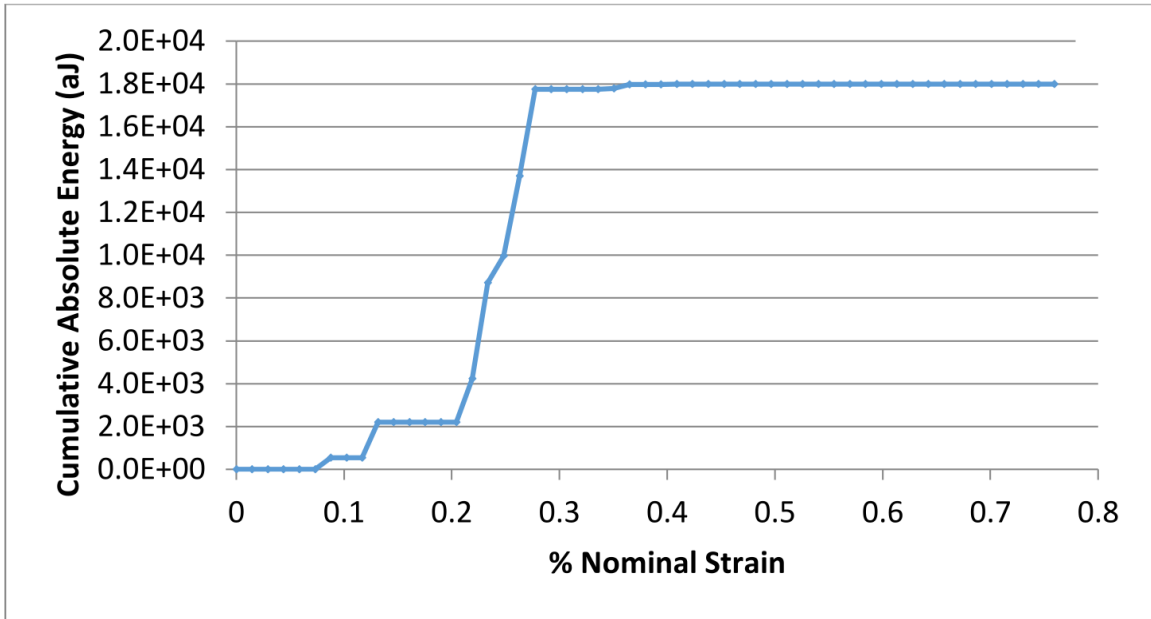
Figure 47: Cumulative energy versus % nominal strain for the titanium alloy substrate [54]

The change in failure behavior during four point bend testing highlights the modifications to material properties that can be obtained by adding reinforcing particles. The change in the

WC-Co-Ni coating into a brittle failure behavior shows that the carbide particles can have a significant impact on coating properties. Brittle fracture in the flexure test indicates that the carbide particles have reached a significant quantity to dominate the failure mechanism of the material. This finding may apply to different performance tests, such as abrasive wear resistance. The WC-Co-Ni coating had low wear rates, 20×10^{-6} mm^3/N.m [10], which suggests that the shift to a brittle fracture-based failure can improve the wear rates of the coatings. Additionally, the B$_4$C-Ni coatings had high wear rates, 435×10^{-6} mm^3/N.m, and they did not have sufficient carbide particles to modify the failure behavior in flexure test. Furthermore, the worn surfaces of the B$_4$C-Ni coatings showed wear modes common to ductile metals such as grooves and scratches on the surface (see Fig. 41). This ductile failure behavior was observed in the B$_4$C-Ni coatings for both the four point bending tests and the abrasive wear tests.

4.7 Adhesion Testing

High wear resistance in desirable; however, if the adhesion strength of a coating is low, the coating will fail at the coating-substrate interface. Therefore, in addition to high wear resistance, high adhesion strength is also desirable. Adhesion strength tests were conducted on the B$_4$C-Ni coatings. Ten tests were conducted, three at each carbide loading and one blank test (epoxy only). The adhesion strength of the blank epoxy samples was 79 MPa. All the coatings were found to fail by cohesion or at the epoxy interface. Cohesive failure occurs when the coating fails by delamination, where a portion of the coating is removed while another portion of the coating remains on the surface. Cohesive failure is preferred as there is still a portion of the

coating on the substrate to protect it from wear. Since, either cohesive failure or failure at the epoxy coating interface was obtained in the adhesion tests, Fig. 48 summarizes the cohesive strength results. An increase in the cohesive strength with increasing carbide content is shown in Fig. 48. This behavior is due to the roughening of the coating surface from impacting carbide particles. Rebounding carbide particles have a grit blasting effect on the surface and create micro-asperities that facilitated mechanical interlocking which improves the adhesion of subsequent particles. This trend has also been found in other studies of cold-sprayed MMC coatings [73–75].
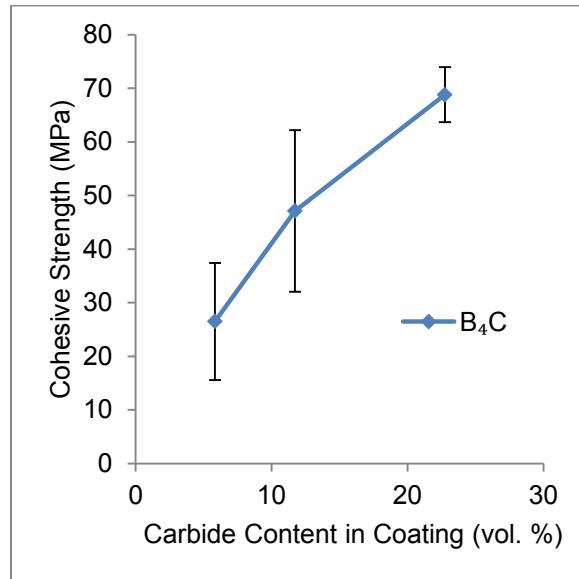
Figure 48: Adhesion strength versus carbide content in B_4C + Ni coatings

The failure of the lowest carbide loading (6 vol.%) coating was found to be cohesive, with the lowest strength at an average of 26.5 MPa. The medium carbide loading coatings (12 vol.%) were found to have both cohesive failure and failure in the epoxy-coating interface, with an average strength of 47.1 MPa. Epoxy-coating interface failure indicates that the coating remains intact. There is no portion of the coating that was removed and only the added epoxy is

removed from the sample surface. Epoxy-coating interface failures suggest that the coating adhesion strength is greater than that of the epoxy adhesion strength. Finally, the coating with the highest loading of reinforcing B_4C particles (23 vol.%) had the highest average strength of 68.8 MPa, with mixed cohesive failure and failure at the epoxy-coating interface. This indicates that there was failure at the epoxy-coating interface and some areas where the coating failed cohesively. The bare substrate was not exposed after these tests, only the coating becoming thinner due to cohesive failure.

Overall, the coatings of all B_4C contents failed either cohesively or at the epoxy-coating interface. None of the failures occurred at the substrate-coating interface. The B_4C + Ni coating with the highest loading of reinforcing particles (23 vol.%) was determined to have an average adhesion strength of 68.8 MPa. This result was consistent with other low-pressure cold-sprayed coatings. Irissou, *et al*. [73] found an adhesion strength above 60 MPa for an Al-Al_2O_3 MMC coating onto a mild steel substrate. Ashrafizadeh and McDonald [76] studied the same low-pressure cold-sprayed TiC-Ni similar to that of this study and found a maximum cohesive strength of 47 MPa. The high cohesive strength of the B_4C-Ni MMC coating can also be attributed to the slower gun transverse speed. As found by Villa, *et al*. [62] the slower transverse speed results in more substrate heating which allows for facilitated substrate-side deformation. The increase in substrate-side deformation is important to the adhesion of impacting ceramic particles as they do not plastically deform; therefore, the facilitated substrate-side deformation results in more mechanical interlocking and a stronger adhesion in between the coating layers and the substrate.

4.8   Preliminary Corrosion Testing

Preliminary corrosion analysis of the cold-sprayed coatings was conducted using laboratory immersion tests. The tests had limited success due to the spallation of the rust resistant paint that was used. Figure 49 shows the mass loss after exposure to corrosion testing. The WC-Ni coatings and the second TiC-Ni coating did not experience any measurable loss in mass. Table 7 shows the qualitative changes on the coating surface. The paint was found to be spallating from all the substrate surfaces. As a consequence, the test results included to significant error; therefore, meaningful conclusions are difficult to draw and further testing, such as cross section analysis or corrosion products analysis in the testing solutions was not pursued. Each of the testing solutions formed an orange residue over the course of the test; this is expected to be the formation of iron oxides due to the corrosion of the exposed substrate. Although no mass loss was observed in the WC-Ni coating (see Fig. 49) there was still evidence of corrosion due to the formation of corrosion products on the surface of the coating (see Table 7). Overall, the results show that the addition of carbide particles improves the corrosion resistance of the cold-sprayed coating. The cold-sprayed Ni coatings were shown to have a porous surface layer [54], and in fact, Melendez, *et al.* [10] measured a porosity of 7 vol.% for a similar cold-sprayed Ni coating, which was higher than the maximum 2 vol.% porosity found in the cold-sprayed MMC coatings explored by the current study. This porosity may contribute to the penetration of the corrosive fluid and the enhanced corrosion of the substrate. The introduction of the carbide particles reduces the porosity of the coatings as shown in section 4.3.2. As a consequence the reduced porosity has decreased the corrosion rate in the samples. However, these results are preliminary and further testing is required to establish accurate

corrosion rates and to investigate the effect of the different carbide particles on the corrosion rate of the MMC coating.
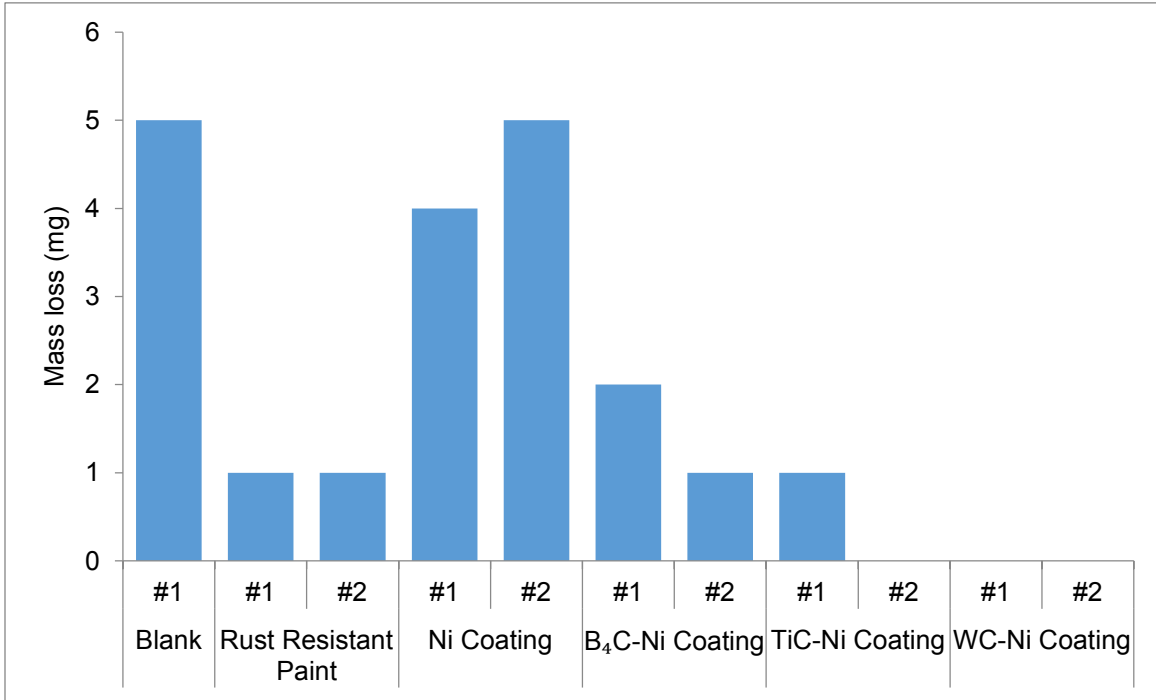
Figure 49: Mass loss from laboratory immersion corrosion tests

Table 7: Observations from the immersion corrosion tests

Sample	Sample #	Mass loss (mg)	Observations on the coating	Observations on the substrate
Blank	#1	5	Not applicable	Dark gray tarnish
Rust Resistant Paint	#1	1	Not applicable	
	#2	1	Not applicable	
Ni Coating	#1	4	Orange and dark gray spots	
	#2	5	Orange and dark gray spots	
B$_4$C-Ni Coating	#1	2	Some orange spots	Paint was spallating from the substrate
	#2	1	No observable change	
TiC-Ni Coating	#1	1	Some dark gray tarnish	
	#2	0	No observable change	
WC-Ni Coating	#1	0	Some orange residue	
	#2	0	Some orange residue	

5 Conclusions[9]

B$_4$C-Ni coatings were successfully fabricated by a low-pressure cold spraying system. Various material properties were measured to evaluate the applicability of the MMC coatings for application in wear environments. The volume fraction of reinforcing carbide particles, mean free path between reinforcing particles, coating hardness, wear rate, adhesion strength, and strain to failure were all evaluated for B$_4$C-Ni coatings. Some of the evaluated parameters were compared against those of TiC- and WC-based MMC coatings to investigate the effects of varying carbide type and thus carbide properties.

The highest reinforcing particle content of 23 vol.% for B$_4$C-Ni, 29 vol.% for TiC-Ni, and 22 vol.% for WC-Ni coatings was achieved by the deposition of 92 wt.% of carbide in the powder blends. In all of the fabricated coatings, the particle size of the carbides was significantly smaller than the powder particles after deposition. This was evidenced by fracturing of the carbide particles upon impact. Based on the effect of fracture of the carbide particles on the deposition efficiency, it was found that the fracture toughness of the selected carbides can be considered as an important parameter for deposition efficiency of reinforcing particles in cold-sprayed MMC coatings. Carbides with higher fracture toughness exhibited higher deposition efficiencies, wherein they increased deposition efficiency by embedding themselves into the coating and roughening the surface to facilitate the adhesion of the impacting powder particles.

---

[9] Portions of this chapter were published in: Y.T.R. Lee, H. Ashrafizadeh, G. Fisher, A. McDonald, Evaluation of the effect of the type of reinforcing particles on the deposition efficiency and wear resistance of low-pressure cold-sprayed MMC coatings, Surf. Coat. Technol., under review, (Manuscript Number: SURFCOAT-D-16-03283).

The velocity and momentum of carbide particles during cold spraying was estimated by using a mathematical model. It was found that the particle momentum can affect the hardness of the MMC coating. The impact of carbides with higher momentum led to a higher degree of work hardening of the matrix which resulted in improvements of the hardness of the MMC coatings. The maximum hardness obtained for all the MMC coatings that were studied was found to be similar at approximately 400 kg/mm^2. The fact that the B$_4$C reinforcing particles are much harder than WC emphasized on the significant effect of particle momentum and possible work hardening of the matrix on the hardness of the cold-sprayed MMC coatings.

Evaluation of the wear rates of the fabricated MMC coatings showed that the WC-Ni MMC coating had the lowest wear rate with similar hardness values to that of TiC and B$_4$C-based MMC coatings. The lower wear resistance of the WC-Ni MMC coatings was due to the high fracture toughness of the WC particles and also the work-hardened Ni matrix in the WC-Ni coating. This emphasized on the importance of the fracture toughness of the carbide particles and the in-flight particle momentum on the wear resistance of cold-sprayed MMC coatings. The worn surfaces showed that the primary material removal mechanism of the MMC coatings are those found in ductile materials, microcutting and microploughing. Additionally, these wear rates found were still not comparable to the wear rates, of 20 x 10^{-6} mm^3/N.m, found by Melendez, *et al.* [10]. The fracture behavior as investigated by four point bend testing with acoustic emission offered an explanation for this difference. The WC-Co-Ni coating was found to experience brittle fracture behavior, while the B$_4$C-Ni coating was found to behave similar to an unreinforced Ni matrix. This provided further evidence that the B$_4$C-Ni coating did not have sufficient reinforcing particles to change the failure behavior of the B$_4$C-Ni coating. Therefore, the wear

rates of the B_4C-Ni coatings were not modified and still dominated by the ductile matrix; thus, the wear rates were higher.

Adhesion testing showed that the cold-sprayed B_4C-Ni coatings experienced cohesive failure and had high cohesive strengths. The high cohesive strength was attributed to the sprayed carbide particles increasing the surface roughness and creating micro-asperities to enhance mechanical interlocking between coating layers. Further increase in the cohesive strength in the coatings fabricated from 92 wt.% B_4C + 8 wt.% Ni, was attributed to the slower transverse speed of the spray nozzle. The slower nozzle speed increased substrate-side plastic deformation with improved mechanical interlocking between coating layers.

The preliminary laboratory immersion corrosion testing showed that the carbide particles within the cold spray feedstock powder can improve the corrosion resistance of the coating. It was found that the impacting carbide particles caused compaction of the deposited coating layers and reduced the porosity of the coating, which led to the reduction of corrosion experienced by the coatings.

This study has shown that low-pressure cold spraying can produce high quality B_4C-Ni coatings. The fracture toughness and carbide particle momentum have been shown to influence the material properties of the MMC coatings. The hardness and adhesion strength of the B_4C-Ni

coatings are comparable to other cold-sprayed MMC coatings. However, more work needs to be conducted to improve the wear rates of the B_4C-Ni coating.

6 Future Work and Recommendations

The primary focus of this study was to fabricate low-pressure cold-sprayed B_4C-Ni coatings for wear application. The performance of the B_4C-Ni coatings was evaluated and compared against low-pressure cold-sprayed TiC- and WC-based coatings. It was found that the fracture toughness and carbide particle momentum can influence the hardness and wear rates of the fabricated coatings. Wear scars were analyzed to determine the material removal mechanisms; however, cross-sectional wear scar analysis should be conducted to investigate further the dispersion of reinforcing particles within the wear scars.

Additional testing could also further understanding of the wear and corrosion resistance of the coatings. Preliminary corrosion tests were conducted in this study; however, the results only showed that the inclusion of carbide particles reduced the corrosion rates due to reduced porosity. Further corrosion tests with a longer duration and improved protection of the substrate is needed to evaluate accurate corrosion rates. Wet abrasion tests, such as ASTM G105 (2016) [77] or ASTM B611 (2013) [78], should also be conducted to investigate the wear behavior in slurries, where both wear and corrosion are a possibility.

Further investigation of the microstructure could also improve the understanding of the effect of impacting carbide particles of different momenta. Grain size measurements within the Ni matrix could identify the grain refinement associated with work hardened materials. Either

etching of the coatings could be explored or the use of electron backscatter diffraction (EBSD) could be used.

Replacing WC-based coatings with B_4C-based coating can also reduce the cost of wear resistant coatings. Currently, commercial B_4C powder costs approximately $121/kg [79]. While a similar commercial WC powder costs approximately $142/kg [80]. There is an advantage when comparing weight of the powders; however, it is the volume fraction of carbide within a coating that influences the MMC coating performance. The cost advantage of B_4C increases significantly when comparing the cost per volume of the carbides due to the higher density of WC. As the development of B_4C-based coatings continues, the cost of B_4C may change and additional economic analysis should be conducted to investigate the feasibility of B_4C-based coatings.

The low-stress abrasion wear rates of the B_4C-Ni coatings were high and would not be able to compete against current HVOF WC-based coatings. However, further work can be done to optimize the powder blend for higher carbide particle deposition efficiency. Feng, *et al.* [41] showed that B_4C reinforcing particle contents up to 44 vol.% could be obtained by using chemical vapor deposition (CVD) to deposit a layer of Ni onto the B_4C particles before high-pressure cold spraying. If a B_4C-Ni sintered and agglomerated powder, similar to the one used by Melendez, *et al.* [10,16] used for the WC-Co-Ni coatings, higher B_4C reinforcing particle content in the fabricated coating could be achieved and lower wear rates are possible.

References

[1] A. Al-Hamed, H.Y. Al-Fadhli, S. Al-Mutairi, B.S. Yilbas, M.S.J. Hashmi, J. Stokes, Investigation of HVOF thermal sprayed nanostructured WC-12Co mixed with Inconel-625 coatings for oil/gas applications, in: Surf. Eff. Contact Mech. XI, WIT Press, Southampton, 2013: pp. 215–225.

[2] P.L. Fauchais, J.V.R. Heberlein, M.I. Boulos, Thermal Spray Fundamentals, Springer US, Boston, MA, 2014.

[3] R.C. Tucker, A.I.H. Committee, A.S. for M.T.S. Division, Thermal Spray Technology, ASM International, 2013.

[4] K.-H. Zum Gahr, Microstructure and wear of materials, Elsevier, Amsterdam ; New York, 1987.

[5] P.L. Menezes, S.P. Ingole, M. Nosonovsky, S.V. Kailas, M.R. Lovell, eds., Tribology for scientists and engineers: from basics to advanced concepts, Springer, New York, 2013.

[6] Sankara Papavinasam, Parviz Rahimi, Sandy Williamson, Corrosion Conditions in the Path of Bitumen from Well to Wheel, in: National Association of Corrosion Engineers, Toronto, Canada, 2012.

[7] B. Bhushan, Modern Tribology Handbook, Two Volume Set, CRC Press, Hoboken, 2000.

[8] M.J. Neale, M.G. Gee, Guide to wear problems and testing for industry, William Andrew Pub, Norwich, N.Y, 2001.

[9] N. Chawla, K.K. Chawla, Metal Matrix Composites, Springer New York, New York, NY, 2013.

[10] N.M. Melendez, V.V. Narulkar, G.A. Fisher, A.G. McDonald, Effect of reinforcing particles on the wear rate of low-pressure cold-sprayed WC-based MMC coatings, Wear 306 (2013) 185–195.

[11] I.A. Ibrahim, F.A. Mohamed, E.J. Lavernia, Particulate reinforced metal matrix composites - A review, J. Mater. Sci. 26 (1991) 1137–1156.

[12] I.M. Hutchings, Tribological properties of metal matrix composites, Mater. Sci. Technol. 10 (1994) 513–517.

[13] G.Y. Lee, C.K. Dharan, R. Ritchie, A physically-based abrasive wear model for composite materials, Wear 252 (2002) 322–331.

[14] ÖN Doğan, JA Hawk, JH Tylczak, RD Wilson, RD Govier, Wear of titanium carbide reinforced metal matrix composites, Wear 225–229 (1999) 758–769.

[15] H.S. Kim, On the rule of mixtures for the hardness of particle reinforced composites, Mater. Sci. Eng. A. 289 (2000) 30–33.

[16] N.M. Melendez, A.G. McDonald, Development of WC-based metal matrix composite coatings using low-pressure cold gas dynamic spraying, Surf. Coat. Technol. 214 (2013) 101–109.

[17] N. Axén, S. Jacobson, A model for the abrasive wear resistance of multiphase materials, Wear 174 (1994) 187–199.

[18] H. Ashrafizadeh, A. Lopera-Valle, A. Gerlich, A. McDonald, Effect of Friction-Stir Processing on the Wear Rate of WC-Based MMC Coatings Deposited by Low-Pressure Cold Gas Dynamic Spraying, in: ASM International, Long Beach, California, USA, 2015: pp. 41–47.

[19] K.J. Hodder, H. Izadi, A.G. McDonald, A.P. Gerlich, Fabrication of aluminum–alumina metal matrix composites via cold gas dynamic spraying at low pressure followed by friction stir processing, Mater. Sci. Eng. A. 556 (2012) 114–121.

[20] R. Gonzalez, H. Ashrafizadeh, A. Lopera, P. Mertiny, A. McDonald, A Review of Thermal Spray Metallization of Polymer-Based Structures, J. Therm. Spray Technol. 25 (2016) 897–919.

[21] H. Ashrafizadeh, P. Mertiny, A. McDonald, Determination of temperature distribution within polyurethane substrates during deposition of flame-sprayed aluminum–12silicon coatings using Green's function modeling and experiments, Surf. Coat. Technol. 259 (2014) 625–636.

[22] D.A. Stewart, P.H. Shipway, D.G. McCartney, Abrasive wear behaviour of conventional and nanocomposite HVOF-sprayed WC–Co coatings, Wear 225–229 (1999) 789–798.

[23] H. Chen, I. Hutchings, Abrasive wear resistance of plasma-sprayed tungsten carbide–cobalt coatings, Surf. Coat. Technol. 107 (1998) 106–114.

[24] Y. Zhang, J. Huang, C. Ding, Mechanical and Tribological Properties of Plasma-Sprayed Cr_3C_2-NiCr, WC-Co, and Cr_2O_3 Coatings, J. Therm. Spray Technol. 7 (1998) 242–246.

[25] M.A. Zavareh, A.A.D.M. Sarhan, P.A. Zavareh, B.B.A. Razak, W.J. Basirun, M.B.C. Ismail, Development and protection evaluation of two new, advanced ceramic composite thermal spray coatings, Al_2O_3–40TiO_2 and Cr_3C_2–20NiCr on carbon steel petroleum oil piping, Ceram. Int. 42 (2016) 5203–5210.

[26] S. Al-Mutairi, M.S.J. Hashmi, B.S. Yilbas, J. Stokes, Microstructural characterization of HVOF/plasma thermal spray of micro/nano WC–12%Co powders, Surf. Coat. Technol. 264 (2015) 175–186.

[27] J.M. Guilemany, J.M. de Paco, J.R. Miguel, J. Nutting, Characterization of the W_2C phase formed during the high velocity oxygen fuel spraying of a WC + 12 pct Co powder, Metall. Mater. Trans. A. 30 (1999) 1913–1921.

[28] H. Wang, X. Song, X. Liu, C. Wei, Y. Gao, J. Fu, Effect of heat-treatment of spray-dried powder on properties of ultrafine-structured WC–Co coating, Surf. Coat. Technol. 207 (2012) 117–122.

[29] X. Qi, N. Eigen, E. Aust, F. Gärtner, T. Klassen, R. Bormann, Two-body abrasive wear of nano- and microcrystalline TiC–Ni-based thermal spray coatings, Surf. Coat. Technol. 200 (2006) 5037–5047.

[30] G.C. Saha, T.I. Khan, Comparative Abrasive Wear Study of HVOF Coatings Obtained by Spraying WC-17Co Microcrystalline and Duplex Near-Nanocrystalline Cermet Powders, J. Eng. Mater. Technol. 133 (2011) 41002.

[31] J.M. Guilemany, S. Dosta, J.R. Miguel, The enhancement of the properties of WC-Co HVOF coatings through the use of nanostructured and microstructured feedstock powders, Surf. Coat. Technol. 201 (2006) 1180–1190.

[32] A. Papyrin, Cold spray technology, Elsevier, Amsterdam; London, 2007.

[33] T. Schmidt, F. Gärtner, H. Assadi, H. Kreye, Development of a generalized parameter window for cold spray deposition, Acta Mater. 54 (2006) 729–742.

[34] H. Ashrafizadeh, A. McDonald, P. Mertiny, Deposition of Electrically Conductive Coatings on Castable Polyurethane Elastomers by the Flame Spraying Process, J. Therm. Spray Technol. 25 (2016) 419–430.

[35] A. Moridi, S.M. Hassani-Gangaraj, M. Guagliano, M. Dao, Cold spray coating: review of material systems and future perspectives, Surf. Eng. 30 (2014) 369–395.

[36] R.G. Maev, V. Leshchynsky, eds., Cold gas dynamic spray, CRC Press, Taylor & Francis Group, Boca Raton, 2016.

[37] A. Sova, A. Papyrin, I. Smurov, Influence of Ceramic Powder Size on Process of Cermet Coating Formation by Cold Spray, J. Therm. Spray Technol. 18 (2009) 633–641.

[38] A. Sova, V.F. Kosarev, A. Papyrin, I. Smurov, Effect of Ceramic Particle Velocity on Cold Spray Deposition of Metal-Ceramic Coatings, J. Therm. Spray Technol. 20 (2011) 285–291.

[39] H.-J. Kim, C.-H. Lee, S.-Y. Hwang, Fabrication of WC–Co coatings by cold spray deposition, Surf. Coat. Technol. 191 (2005) 335–340.

[40] S. Dosta, M. Couto, J.M. Guilemany, Cold spray deposition of a WC-25Co cermet onto Al7075-T6 and carbon steel substrates, Acta Mater. 61 (2013) 643–652.

[41] C. Feng, V. Guipont, M. Jeandin, O. Amsellem, F. Pauchet, R. Saenger, S. Bucher, C. Iacob, B_4C/Ni Composite Coatings Prepared by Cold Spray of Blended or CVD-Coated Powders, J. Therm. Spray Technol. 21 (2012) 561–570.

[42] A. Nino, A. Tanaka, S. Sugiyama, H. Taimatsu, Indentation Size Effect for the Hardness of Refractory Carbides, Mater. Trans. 51 (2010) 1621–1626.

[43] H. Engqvist, S. Ederyd, N. Axén, S. Hogmark, Grooving wear of single-crystal tungsten carbide, Wear 230 (1999) 165–174.

[44] J.F. Shackelford, Y.-H. Han, S. Kim, S.-H. Kwon, CRC materials science and engineering handbook, Fourth edition, CRC Press, Boca Raton; London; New York, 2015.

[45] M.W. Barsoum, Fundamentals of ceramics, Second edition, CRC Press, Bristol, 2003.

[46] Technical Data Sheet SST-N5001, (2015). http://supersonicspray.com/knowledge-docs/en/SST-TDS-N5001-PR-1_1-0415.pdf.

[47] H. Ashrafizadeh, P. Mertiny, A. McDonald, Evaluation of the effect of temperature on mechanical properties and wear resistance of polyurethane elastomers, Wear 368–369 (2016) 26–38.

[48] M. Kouzeli, A. Mortensen, Size dependent strengthening in particle reinforced aluminium, Acta Mater. 50 (2002) 39–51.

[49] D.L. Bish, S.A. Howard, Quantitative phase analysis using the Rietveld method, J. Appl. Crystallogr. 21 (1988) 86–91.

[50] ASTM E384-11e1, Standard Test Method for Knoop and Vickers Hardness of Materials, ASTM International, West Conshohocken, PA, 2015. www.astm.org.

[51] ASTM C1327-15, Standard Test Method for Vickers Indentation Hardness of Advanced Ceramics, ASTM International, West Conshohocken, PA, 2015. www.astm.org.

[52] ASTM G65-04(2010), Standard Test Method for Measuring Abrasion Using the Dry Sand/Rubber Wheel Apparatus, ASTM International, West Conshohocken, PA, 2015. www.astm.org.

[53] G.W. Stachowiak, A.W. Batchelor, Engineering tribology, 3rd ed, Elsevier Butterworth-Heinemann, Amsterdam; Boston, 2005.

[54] M. Shibly, Fracture behaviour of cold sprayed cermet coatings, University of Nottingham, 2016.

[55] ASTM C633-13, Standard Test Method for Adhesion or Cohesion Strength of Thermal Spray Coatings, ASTM International, West Conshohocken, PA, 2013. www.astm.org.

[56] NACE/ASTM G31-12a, Standard Guide for Laboratory Immersion Corrosion Testing of Metals, ASTM International, West Conshohocken, PA, 2012. www.astm.org.

[57] R.C. Dykhuizen, M.F. Smith, Gas Dynamic Principles of Cold Spray, J. Therm. Spray Technol. 7 (1998) 205–212.

[58] M. Grujicic, C.. Zhao, C. Tong, W.. DeRosset, D. Helfritch, Analysis of the impact velocity of powder particles in the cold-gas dynamic-spray process, Mater. Sci. Eng. A. 368 (2004) 222–230.

[59] Y.T.R. Lee, H. Ashrafizadeh, G. Fisher, A. McDonald, Effect of content and type of reinforcing particles on the hardness and wear rate of low-pressure cold-sprayed TiC and B4C-based metal matrix composite coatings, in: ASM International, Shanghai, China, 2016: pp. 310–315.

[60] U. Prisco, Size-dependent distributions of particle velocity and temperature at impact in the cold-gas dynamic-spray process, J. Mater. Process. Technol. 216 (2015) 302–314.

[61] H.Z. Li, J. Wang, J.M. Fan, Analysis and modelling of particle velocities in micro-abrasive air jet, Int. J. Mach. Tools Manuf. 49 (2009) 850–858.

[62] M. Villa Vidaller, F. Haußler, H. Assadi, F. Gärtner, T. Klassen, Influence of Substrate on Cold Sprayed Titanium Coatings, in: ASM International, Long Beach, California, USA, 2015: pp. 1047–1054.

[63] H. Assadi, F. Gärtner, T. Stoltenhoff, H. Kreye, Bonding mechanism in cold gas spraying, Acta Mater. 51 (2003) 4379–4394.

[64] T. Schmidt, H. Assadi, F. Gärtner, H. Richter, T. Stoltenhoff, H. Kreye, T. Klassen, From Particle Acceleration to Impact and Bonding in Cold Spraying, J. Therm. Spray Technol. 18 (2009) 794–808.

[65] I. Miller, J.E. Freund, Probability and statistics for engineers, 3rd ed, Prentice-Hall, Englewood Cliffs, NJ, 1985.

[66] H.K. Tonshoff, I. Inaski, I.D. Marinescu, Handbook of Ceramics Grinding & Polishing, Elsevier Science, Park Ridge, NJ, 2000.

[67] K. Neishi, Z. Horita, T.G. Langdon, Grain refinement of pure nickel using equal-channel angular pressing, Mater. Sci. Eng. A. 325 (2002) 54–58.

[68] M.P. Dewar, A.G. McDonald, A.P. Gerlich, Interfacial heating during low-pressure cold-gas dynamic spraying of aluminum coatings, J. Mater. Sci. 47 (2012) 184–198.

[69] R.C. Dykhuizen, M.F. Smith, D.L. Gilmore, R.A. Neiser, X. Jiang, S. Sampath, Impact of High Velocity Cold Spray Particles, J. Therm. Spray Technol. 8 (1999) 559–564.

[70] K. Kim, M. Watanabe, J. Kawakita, S. Kuroda, Grain refinement in a single titanium powder particle impacted at high velocity, Scr. Mater. 59 (2008) 768–771.

[71] W.-Y. Li, C. Zhang, H. Liao, J. Li, C. Coddet, Characterizations of cold-sprayed Nickel–Alumina composite coating with relatively large Nickel-coated Alumina powder, Surf. Coat. Technol. 202 (2008) 4855–4860.

[72] H. Saito, A. Iwabuchi, T. Shimizu, Effects of Co content and WC grain size on wear of WC cemented carbide, Wear 261 (2006) 126–132.

[73] E. Irissou, J.-G. Legoux, B. Arsenault, C. Moreau, Investigation of Al-Al$_2$O$_3$ Cold Spray Coating Formation and Properties, J. Therm. Spray Technol. 16 (2007) 661–668.

[74] H.Y. Lee, S.H. Jung, S.Y. Lee, Y.H. You, K.H. Ko, Correlation between Al$_2$O$_3$ particles and interface of Al–Al$_2$O$_3$ coatings by cold spray, Appl. Surf. Sci. 252 (2005) 1891–1898.

[75] K. Spencer, D.M. Fabijanic, M.-X. Zhang, The use of Al–Al$_2$O$_3$ cold spray coatings to improve the surface properties of magnesium alloys, Surf. Coat. Technol. 204 (2009) 336–344.

[76] H. Ashrafizadeh, A. McDonald, Final Report – "Evaluation of Abrasion and Corrosion Resistance of Low-Pressure Cold-sprayed TiC-Ni-Based MMC Coatings", submitted to Pacific Particulate Materials (PPM) Ltd., November 6, 2015.

[77] ASTM G105-16, Standard Test Method for Conducting Wet Sand/Rubber Wheel Abrasion Tests, ASTM International, West Conshohocken, PA, 2016. www.astm.org.

[78] ASTM B611-13, Standard Test Method for Determining the High Stress Abrasion Resistance of Hard Materials, ASTM International, West Conshohocken, PA, 2013. www.astm.org.

[79] Boron Carbide Powder 500 Grit - 25 Lbs in a Box, Boron Carbide Powder 500 Grit - 25 Lbs Box. (n.d.). https://www.amazon.com/Boron-Carbide-Powder-500-Grit/dp/B00BMAU6PQ (accessed December 14, 2016).

[80] WP-305, TUNGSTEN CARBIDE POWDER - Micron Metals, WP-305 TUNGSTEN CARBIDE POWDER. (n.d.). http://micronmetals.com/products/wp-305-tungsten-carbide-powder/ (accessed December 14, 2016).

Appendix A – MATLAB Code

```matlab
clear;clc;
%The velocity of the expanding gas prior to the introduction of the ceramic
particles is calculated in the section A.

%The velocity of the expanding gas after the introduction of the ceramic
particles is calculated in the section B.

%Section C verifies that the shock pressure is above ambient pressure.

%Sections D-F contain the calculations for each carbide particle.


%% SECTION A
%The velocity of the expanding gas prior to the introduction of the ceramic
%particles is calculated in the section A.

g=1.4; %Ratio of specific heats for air, gamma
%R=8.3144598; %Gas Constant, J/mol/K
R=287; %Specific Gas Constant for Air, J/K/kg
r_throat=1.25E-3; %Throat Radius, m
r_1=2.3E-3; %Radius where ceramics are introduced, m
x=[0:0.1:5]; %x direction along the expansion, mm
r=r_throat+(r_1-r_throat)*x/5; %radius along the expansion, m
A=r.^2*pi; %cross sectional area along the expansion, m^2
T_o=550+273.15; %Temperature of the gas entering the expansion, K
P_o=634000+101325; %Pressure of gas entering the expansion, Pa
rho_o=P_o/(R*T_o); % Density of air entering the expansion, kg/m^3

k1=218.0629-243.5764*g+71.7925*g^2; %Eq. 5b
k2=-0.12245+0.28130*g; %Eq. 5c
M=(k1.*A./A(1)+(1-k1)).^k2; %Mach number along the expansion, Eq. 5a

P_throat=P_o/(1+(g-1)/2)^(g/(g-1)); %Throat pressure, Pa, Eq. 6b
P=P_throat.*((g+1)./(2+(g-1).*M.^2)).^(g/(g-1)); %Pressure of air along the
expansion, Pa, Eq. 6a
T=T_o./(1+((g-1)/2).*M.^2); %Temperature of air along the expansion, K, Eq. 7
V=M.*sqrt(g.*R.*T); %Velocity of air along the expansion, m/s, Eq. 8
rho=rho_o./((1+(g-1)./2).*M.^2).^(1/(g-1)); %Density of air along the
expansion, kg/m^3, Eq. 9

V_1=V(end); %Define air velocity where the ceramic particles are introduced


%% SECTION B
%The velocity of the expanding gas after the introduction of the ceramic
%particles is calculated in the following section B.

g=1.4; %Ratio of specific heats for air, gamma
%R=8.3144598; %Gas Constant, J/mol/K
R=287; %Specific Gas Constant for Air, J/K/kg
r_1=2.3E-3; %Radius where ceramics are introduced, m
r_2=3.2E-3; %Radius of the nozzle outlet, m
x_b=[0.1:0.1:120]; %x direction, along the length of the nozzle, mm
```

```matlab
r_b=r_1+(r_2-r_1)*x_b/120; %Radius along nozzle, m
A_b=r_b.^2*pi; %Cross sectional area along the nozzle, m^2
P_atm=101325; %Ambient pressure, Pa


k1=218.0629-243.5764*g+71.7925*g^2; %Eq. 5b
k2=-0.12245+0.28130*g; %Eq. 5c
M_b=(k1.*A_b./A(1)+(1-k1)).^k2; %Mach number along the nozzle, Eq. 5a


P_b=P_throat.*((g+1)./(2+(g-1).*M_b.^2)).^(g/(g-1)); %Pressure of air along
the nozzle, Pa, Eq. 6a
T_b=T_o./(1+((g-1)/2).*M_b.^2); %Temperature of air along the nozzle, K, Eq.
7
V_b=M_b.*sqrt(g.*R.*T_b); %Velocity of the air along the nozzle, Eq. 8
rho_b=rho_o./(1+((g-1)./2).*M_b.^2).^(1/(g-1)); %Density of air along the
nozzle, Eq. 9
hold on
% Plotting to check velocity
x_tot=[x,5+x_b]; %Total x direction, from the throat to the nozzle exit, mm
V_tot=[V,V_b]; %Total air velocity, from the throat to the nozzle exit, m/s
% plot(x_tot,V_tot)


V_g=V_b; %Gas velocity, m/s
% plot(x_b,V_g)



%% Section C - Shock Pressure
P_s=P_b(end)*(2*g/(g+1)*M_b(end)^2-(g-1)/(g+1));%Eq. 10
Shock=P_atm>=P_s



%% Section D - B4C
d_p=3.9E-5; % Particle diameter, m
rho_p=2.52; % Particle density, g/cm^3
rho_p=rho_p/1000*100^3; % Particle density, kg/m^3

% Viscosity Equation, Eq 13b
nu_ref=18.27E-6; % Reference Viscosity, Pa/s
Tref=291.15; % Reference Temperature, K
C=120; % Sutherland Temp, K

%Initialize
V_p=zeros(1,length(x_b));
n=1;
for n = 2:(length(x_b))
    nu=nu_ref*(Tref+C)/(T_b(n)+C)*(T_b(n)/Tref)^(3/2); % Viscosity, Pa/s, Eq.
13b
    Re_p=abs(V_g(n)-V_p(n-1))*rho_b(n)*d_p/nu; %Particle Reynolds number, Eq.
13a
    M_p=abs(V_g(n)-V_p(n-1))/sqrt(g*R*T_b(n)); %Particle Mach number, Eq. 14
    %Calculate drag coefficient, Eq. 12
    C_D=24/Re_p*((1+0.15*Re_p^0.687)*(1+exp(-(0.427/M_p^4.63)-
(3/Re_p^0.88)))/(1+(M_p/Re_p)*(3.82+1.28*exp(-1.25*M_p/Re_p))));
    %Calculate Velocity, Eq. 15
    V_p(n)=(V_p(n-1)^2+1.5*(x_b(n)-x_b(n-1))*(10^-
3)*C_D*rho_b(n)/d_p/rho_p*(V_g(n)-V_p(n-1))^2)^0.5;
```

A-2

```matlab
end
B4C=V_p;
Ek_B4C=0.5.*B4C.^2.*(rho_p*4/3*pi*(d_p/2)^3); %Particle Energy, J
Momentum_B4C=(rho_p*4/3*pi*(d_p/2)^3)*B4C; %Particle Momentum, Nm, Eq. 16
plot(x_b,B4C)


%% Section E - TiC
d_p=2.3E-5; % Particle diameter, m
rho_p=4.93; % Particle density, g/cm^3
rho_p=rho_p/1000*100^3; % Particle density, kg/m^3

% Viscosity Equation, Eq 13b
nu_ref=18.27E-6; % Reference Viscosity, Pa/s
Tref=291.15; % Reference Temperature, K
C=120; % Sutherland Temp, K

%Initialize
V_p=zeros(1,length(x_b));
n=1;
for n = 2:(length(x_b))
    nu=nu_ref*(Tref+C)/(T_b(n)+C)*(T_b(n)/Tref)^(3/2); % Viscosity, Pa/s, Eq
13b
    Re_p=abs(V_g(n)-V_p(n-1))*rho_b(n)*d_p/nu; %Particle Reynolds number, Eq.
13a
    M_p=abs(V_g(n)-V_p(n-1))/sqrt(g*R*T_b(n)); %Particle Mach number, Eq. 14
    %Calculate drag coefficient, Eq. 12
    C_D=24/Re_p*((1+0.15*Re_p^0.687)*(1+exp(-(0.427/M_p^4.63)-
(3/Re_p^0.88)))/(1+(M_p/Re_p)*(3.82+1.28*exp(-1.25*M_p/Re_p))));
    %Calculate Velocity, Eq. 15
    V_p(n)=(V_p(n-1)^2+1.5*(x_b(n)-x_b(n-1))*(10^-
3)*C_D*rho_b(n)/d_p/rho_p*(V_g(n)-V_p(n-1))^2)^0.5;
end
TiC=V_p;
Ek_TiC=0.5.*TiC.^2.*(rho_p*4/3*pi*(d_p/2)^3); %Particle Energy, J
Momentum_TiC=(rho_p*4/3*pi*(d_p/2)^3)*TiC; %Particle Momentum, Nm, Eq. 16
plot(x_b,TiC)


%% Section F - WC
d_p=3.6E-5; % Particle diameter, m
rho_p=15.8; % Particle density, g/cm^3
rho_p=rho_p/1000*100^3; % Particle density, kg/m^3

% Viscosity Equation, Eq 13b
nu_ref=18.27E-6; % Reference Viscosity, Pa/s
Tref=291.15; % Reference Temperature, K
C=120; % Sutherland Temp, K

%Initialize
V_p=zeros(1,length(x_b));
n=1;
for n = 2:(length(x_b))
    nu=nu_ref*(Tref+C)/(T_b(n)+C)*(T_b(n)/Tref)^(3/2); % Viscosity, Pa/s, Eq
13b
```

```
    Re_p=abs(V_g(n)-V_p(n-1))*rho_b(n)*d_p/nu; %Particle Reynolds number, Eq.
13a
    M_p=abs(V_g(n)-V_p(n-1))/sqrt(g*R*T_b(n)); %Particle Mach number, Eq. 14
    %Calculate drag coefficient, Eq. 12
    C_D=24/Re_p*((1+0.15*Re_p^0.687)*(1+exp(-(0.427/M_p^4.63)-
(3/Re_p^0.88)))/(1+(M_p/Re_p)*(3.82+1.28*exp(-1.25*M_p/Re_p))));
    %Calculate Velocity, Eq. 15
    V_p(n)=(V_p(n-1)^2+1.5*(x_b(n)-x_b(n-1))*(10^-
3)*C_D*rho_b(n)/d_p/rho_p*(V_g(n)-V_p(n-1))^2)^0.5;
end
WC=V_p;
Ek_WC=0.5.*WC.^2.*(rho_p*4/3*pi*(d_p/2)^3); %Particle Energy, J
Momentum_WC=(rho_p*4/3*pi*(d_p/2)^3)*WC; %Particle Momentum, Nm, Eq. 16
plot(x_b,WC)


%%
legend('B_4C','TiC','WC')
hold off
Solution={'','Velocity(m/s)','Energy(J)','Momentum(Nm)';'B4C',B4C(end),Ek_B4C
(end),Momentum_B4C(end);'TiC',TiC(end),Ek_TiC(end),Momentum_TiC(end);'WC',WC(
end),Ek_WC(end),Momentum_WC(end)}
```

Appendix B – SEM Images of Coating Microstructure
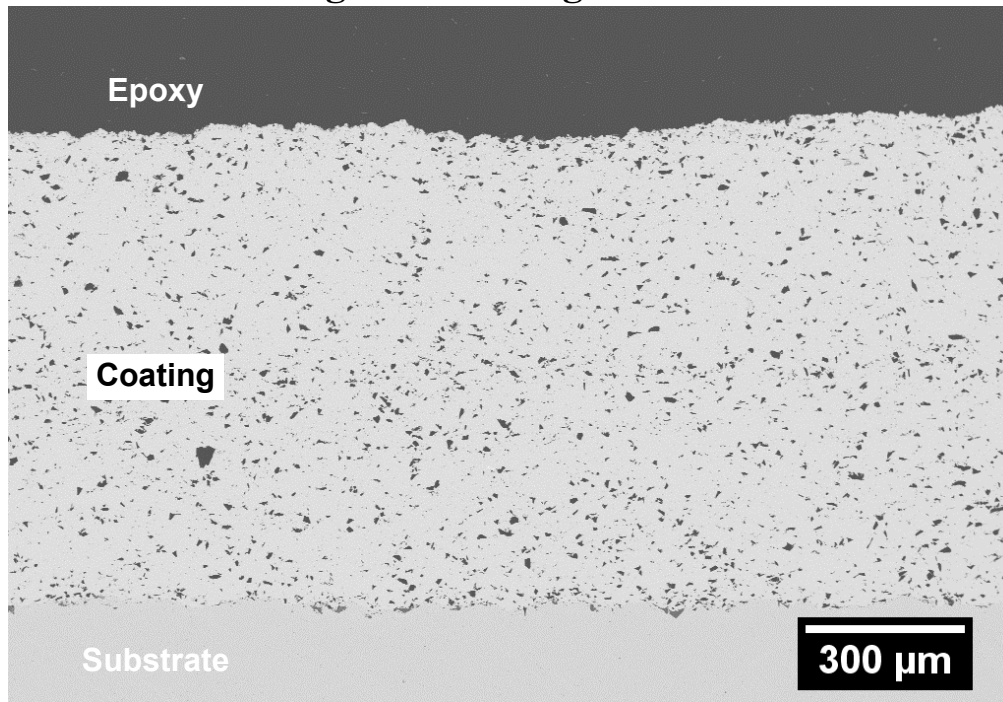
Figure B 1: BSE image of the MMC coatings fabricated from
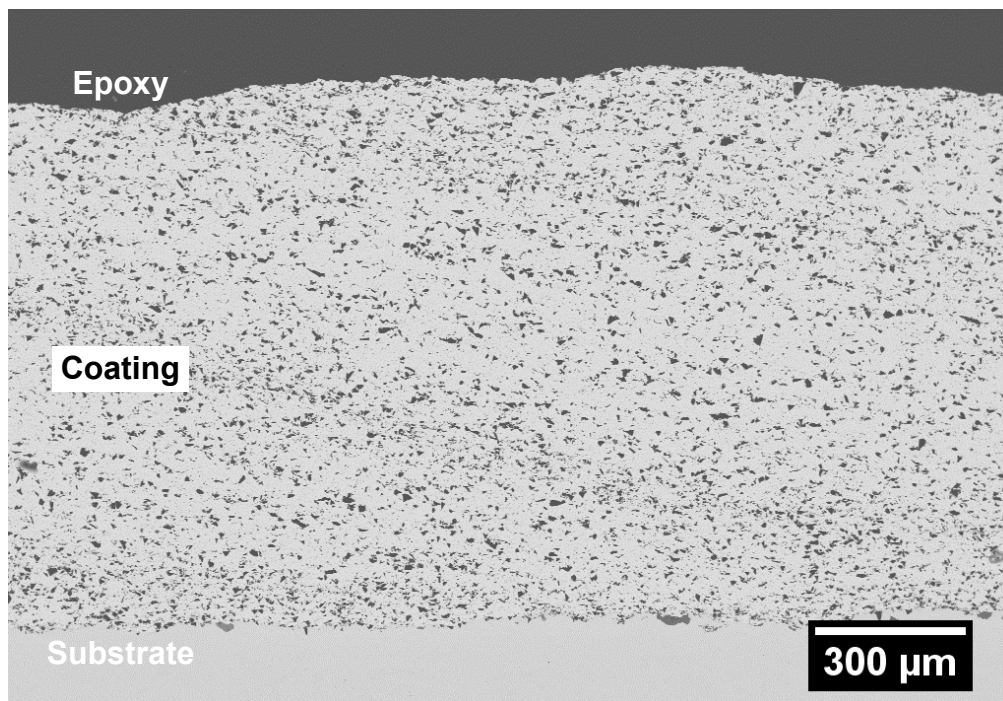50 wt.% B_4C + 50 wt.% Ni in the powder blend

Figure B 2: BSE image of the MMC coatings fabricated from
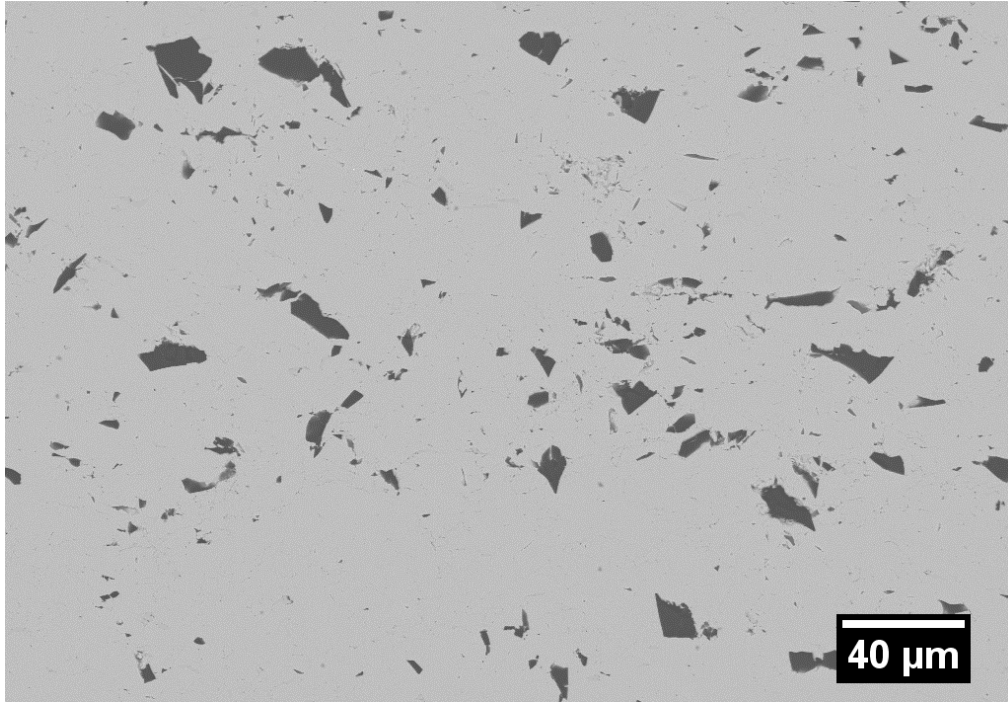75 wt.% B_4C + 25 wt.% Ni in the powder blend

Figure B 3: BSE image of the MMC coatings microstructure fabricated from
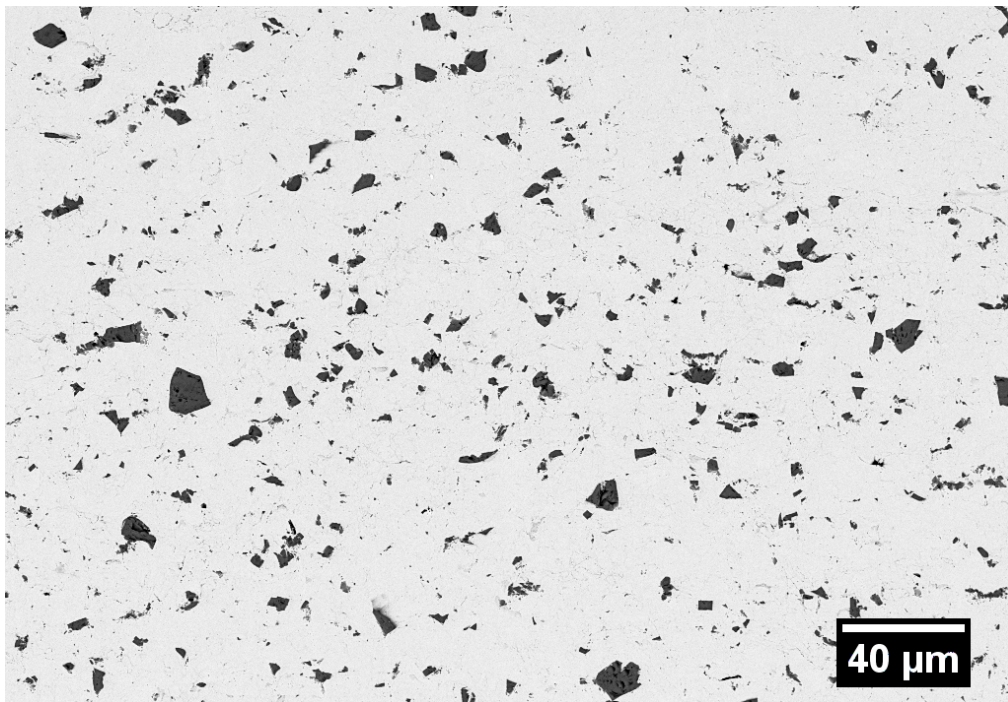50 wt.% B$_4$C + 50 wt.% Ni in the powder blend

Figure B 4: BSE image of the MMC coatings microstructure fabricated from
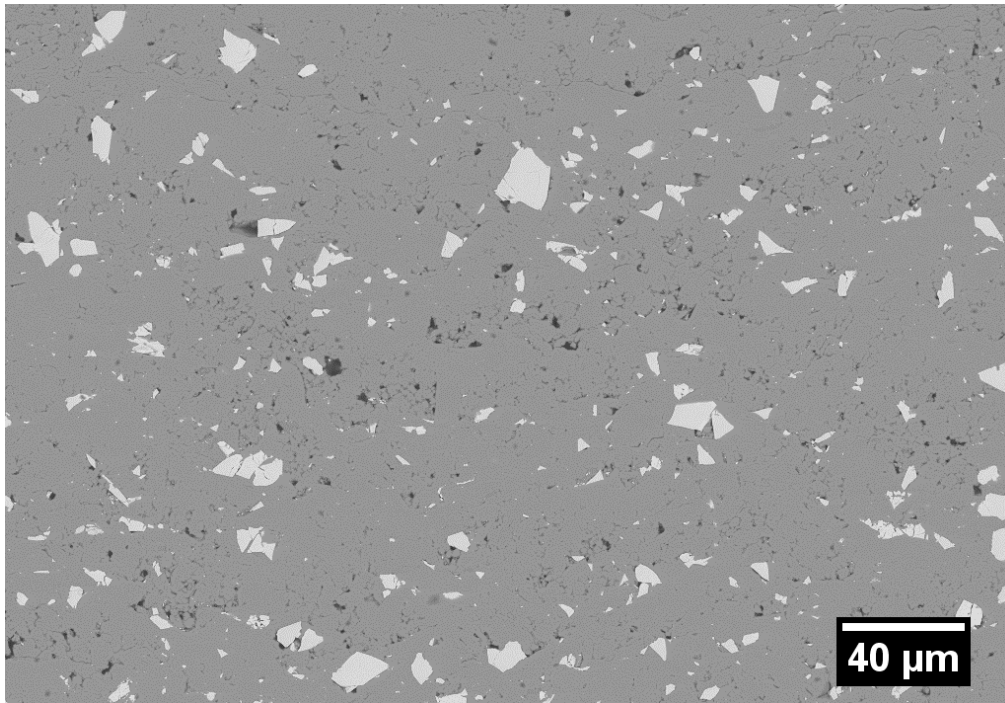50 wt.% TiC + 50 wt.% Ni in the powder blend

Figure B 5: BSE image of the MMC coatings microstructure fabricated from 50 wt.% WC + 50 wt.% Ni in the powder blend
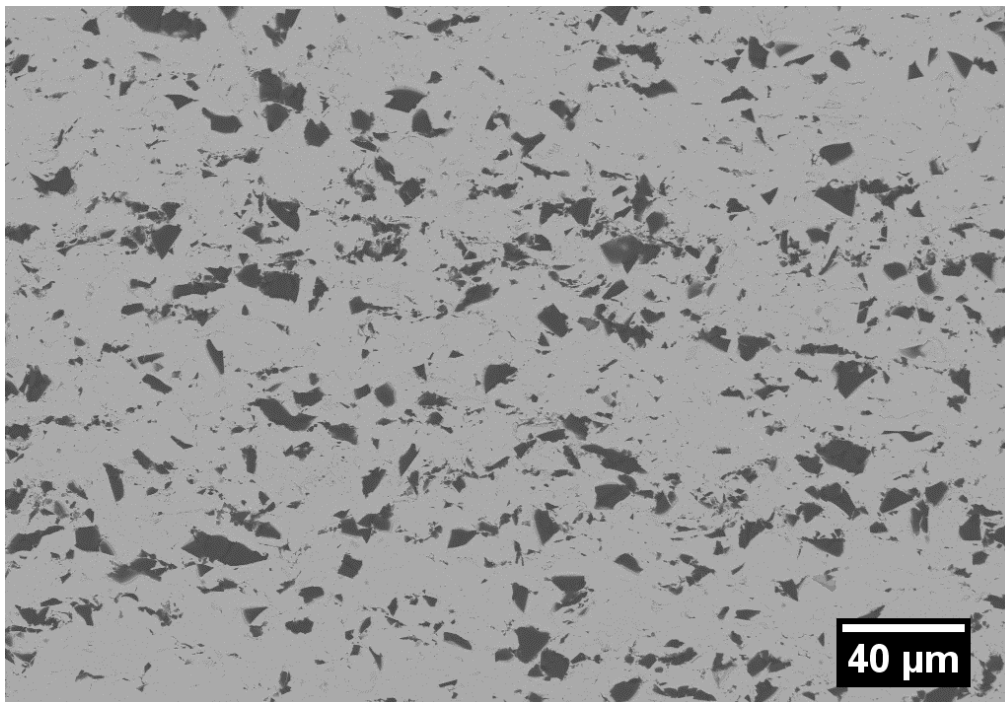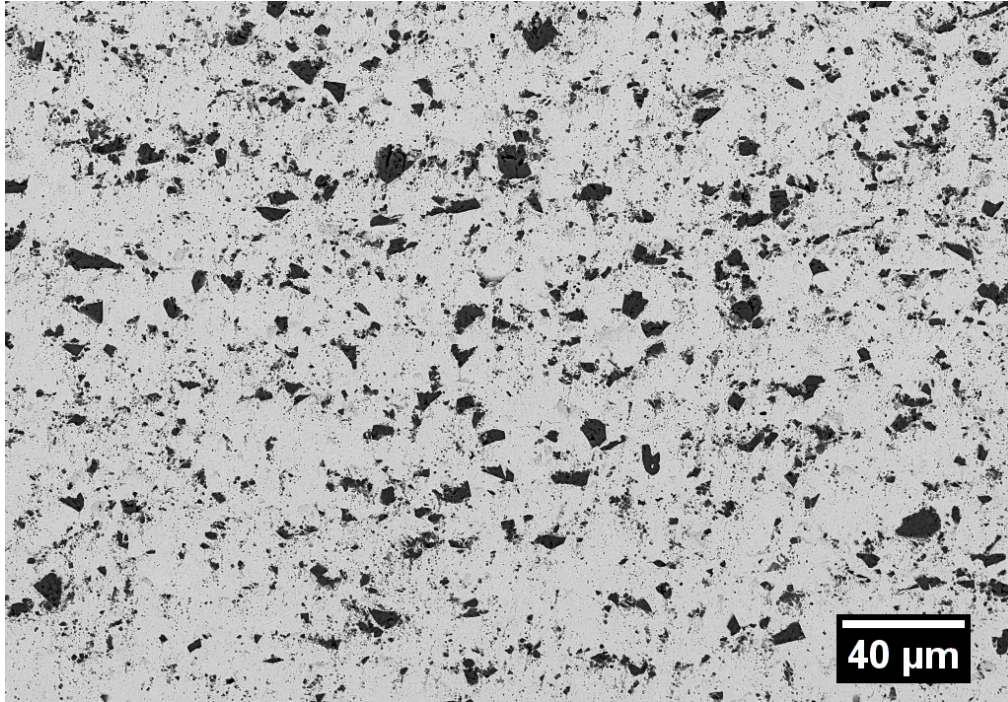

Figure B 6: BSE image of the MMC coatings microstructure fabricated from 75 wt.% B_4C + 25 wt.% Ni in the powder blend

Figure B 7: BSE image of the MMC coatings microstructure fabricated from
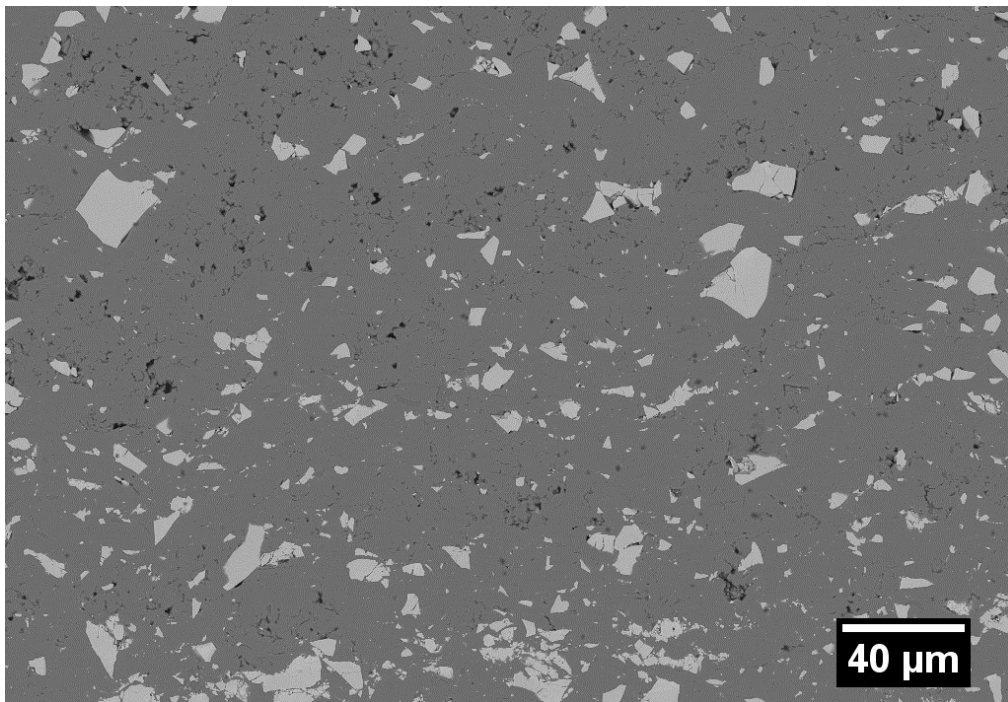75 wt.% TiC + 25 wt.% Ni in the powder blend

Figure B 8: BSE image of the MMC coatings microstructure fabricated from
75 wt.% WC + 25 wt.% Ni in the powder blend